

# How About Vanadium-Based Compounds as Cathode Materials for Aqueous Zinc Ion Batteries?

Tingting Lv,\* Yi Peng, Guangxun Zhang, Shu Jiang, Zilin Yang, Shengyang Yang, and Huan Pang\*

Aqueous zinc-ion batteries (AZIBs) stand out among many monovalent/multivalent metal-ion batteries as promising new energy storage devices because of their good safety, low cost, and environmental friendliness. Nevertheless, there are still many great challenges to exploring new-type cathode materials that are suitable for  $\text{Zn}^{2+}$  intercalation. Vanadium-based compounds with various structures, large layer spacing, and different oxidation states are considered suitable cathode candidates for AZIBs. Herein, the research advances in vanadium-based compounds in recent years are systematically reviewed. The preparation methods, crystal structures, electrochemical performances, and energy storage mechanisms of vanadium-based compounds (e.g., vanadium phosphates, vanadium oxides, vanadates, vanadium sulfides, and vanadium nitrides) are mainly introduced. Finally, the limitations and development prospects of vanadium-based compounds are pointed out. Vanadium-based compounds as cathode materials for AZIBs are hoped to flourish in the coming years and attract more and more researchers' attention.

## 1. Introduction

With the continuous consumption of fossil fuels and the gradual intensification of the greenhouse effect, energy shortages and environmental pollution have become two major problems facing the sustainable development of human society.<sup>[1–7]</sup> The development of clean and green energy resources, such as wind, solar, and tidal power, has received widespread attention.<sup>[8–12]</sup> Therefore, it's essential for efficient energy storage and conversion


devices.<sup>[13–16]</sup> In recent years, lithium-ion batteries (LIBs) have gradually occupied the market for commercial rechargeable batteries due to their high energy density, long service life, and mature preparation technology.<sup>[17–19]</sup> However, despite the commercial success, the limited lithium resources, high cost, unsafety, and environmental pollution problems caused by the flammable and toxic organic electrolyte have seriously hindered the further development and large-scale applications of LIBs.<sup>[20–22]</sup> Compared with organic electrolytes, which have a large number of safety risks, aqueous electrolytes (AEs) have many technical advantages, such as higher safety, low price, and facile manufacturing, and are expected to be employed to develop the next generation of green rechargeable batteries.<sup>[23–26]</sup> More importantly, the ionic conductivity of AEs is two orders of magnitude higher than that of organic electrolytes,

which can promote power densities and fast charging capability.<sup>[27–31]</sup> Since 1994, Li et al.<sup>[32]</sup> introduced aqueous solution as an electrolyte for LIBs. Nowadays, different kinds of aqueous rechargeable batteries on the basis of charge carriers with various valence states (e.g.,  $\text{Li}^+$ ,  $\text{Na}^+$ ,  $\text{K}^+$ ,  $\text{Mg}^{2+}$ ,  $\text{Zn}^{2+}$ ,  $\text{Ca}^{2+}$ , and  $\text{Al}^{3+}$ ) have been developed.<sup>[33–36]</sup> Among these aqueous rechargeable monovalent/multivalent metal-ion batteries, aqueous zinc-ion batteries (AZIBs) are one of the most concerned devices due to their high capacity of  $820 \text{ mAh g}^{-1}$ , excellent volumetric capacity of  $5855 \text{ mAh cm}^{-3}$ , low redox potential of  $-0.763 \text{ V}$  (vs standard hydrogen electrode, SHE), large hydrogen evolution overpotential in AE, repeatable stripping/plating, as well as abundant and cheap (Scheme 1).<sup>[37–41]</sup>

Before AZIBs flourished as they do today, zinc-based batteries had a long history of development (Scheme 2). Zinc-manganese batteries have dominated the primary battery market since their invention by French engineer Georges Le Klain in 1868.<sup>[42]</sup> Alkaline  $\text{Zn/MnO}_2$  batteries were successfully developed on the basis of zinc-manganese batteries in 1986.<sup>[43]</sup> However, the early  $\text{Zn/MnO}_2$  batteries were relatively backward in technology, costly, and wasteful of resources. To save resources and enhance efficiency, rechargeable alkaline  $\text{Zn/MnO}_2$  batteries were developed. However, rechargeable alkaline  $\text{Zn/MnO}_2$  batteries still have some disadvantages, such as low CE and fast capacity decay due to the irreversible reactions on  $\text{Zn/MnO}_2$  batteries' electrodes.<sup>[44]</sup> Until 2012, Xu and co-workers<sup>[45]</sup> successfully

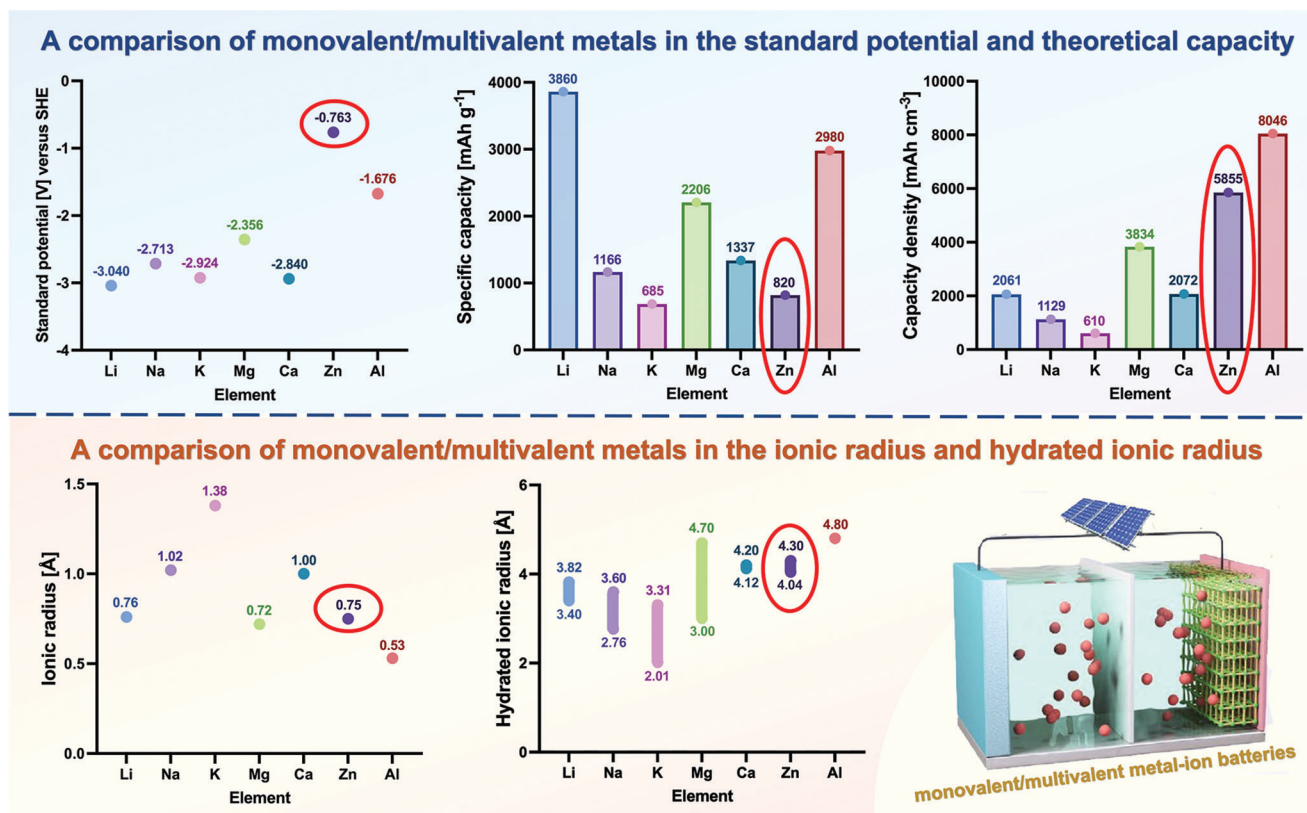
T. Lv  
Interdisciplinary Materials Research Center, Institute for Advanced Study  
Chengdu University  
Chengdu, Sichuan 610106, P. R. China  
E-mail: tingtinglv0311@163.com

T. Lv, Y. Peng, G. Zhang, S. Jiang, Z. Yang, S. Yang, H. Pang  
School of Chemistry and Chemical Engineering  
Yangzhou University  
Yangzhou, Jiangsu 225009, P. R. China  
E-mail: panghuan@yzu.edu.cn

 The ORCID identification number(s) for the author(s) of this article can be found under <https://doi.org/10.1002/adv.202206907>

© 2023 The Authors. Advanced Science published by Wiley-VCH GmbH. This is an open access article under the terms of the Creative Commons Attribution License, which permits use, distribution and reproduction in any medium, provided the original work is properly cited.

DOI: 10.1002/adv.202206907



**Scheme 1.** The comparisons of monovalent/multivalent metals in the standard potential and theoretical capacity (Top), ionic radius, and hydrated ionic radius (Bottom).

developed rechargeable AZIBs using mild zinc sulfate as the electrolyte,  $\alpha$ - $\text{MnO}_2$  as the positive material, and Zn as the negative material. Polycrystalline  $\text{MnO}_2$  (mainly including  $\alpha$ ,  $\beta$ , R,  $\delta$ , T,  $\lambda$ ,  $\epsilon$ , and  $\gamma$ ), Prussian blue, and its analogs (e.g., copper hexacyanoferrate and zinc hexacyanoferrate) have attracted much attention as cathode materials.<sup>[46–51]</sup> However, the crystal structure of  $\text{MnO}_2$  is unstable, and it shows poor cycling performance in the (dis)charging process.<sup>[52,53]</sup> In addition, Prussian blue and its analogs have a stable crystal structure, but poor Zn storage capacity (less than 100  $\text{mAh g}^{-1}$ ).<sup>[54,55]</sup> Therefore, the development of structurally stable and high-capacity cathode materials has become one of the keys for the research of AZIBs.<sup>[56–58]</sup>

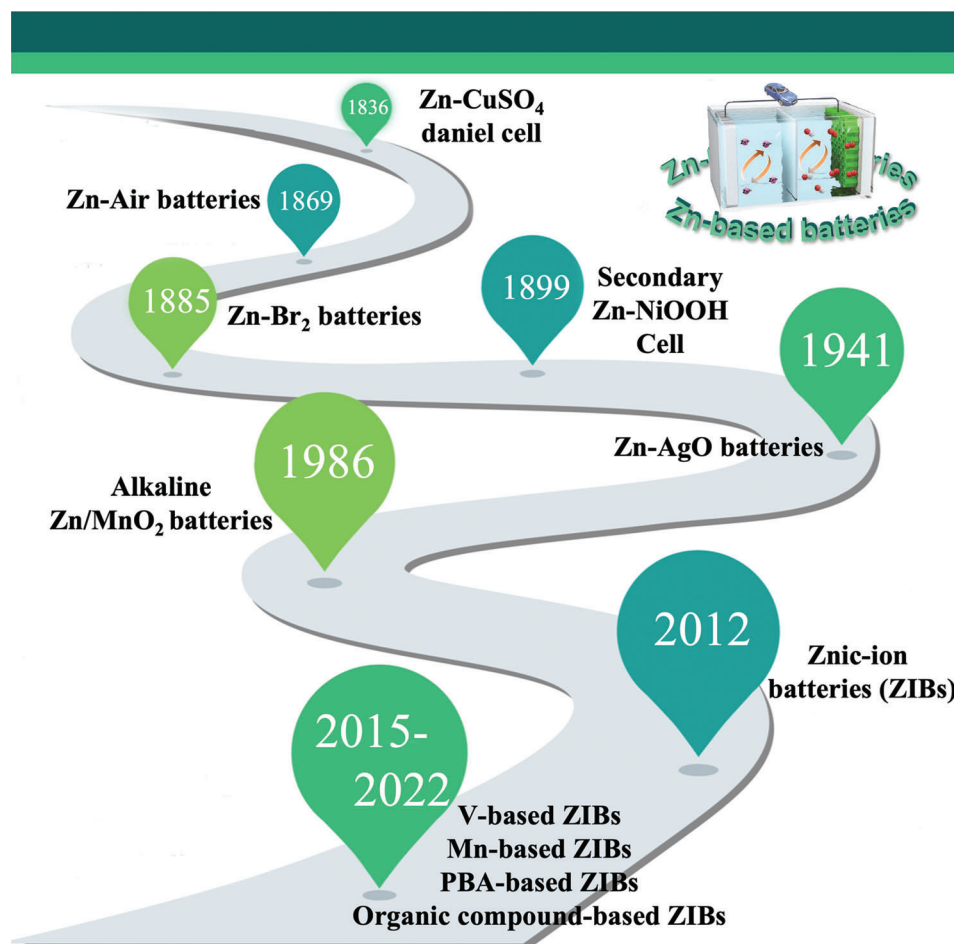
In 2016, Dipan Kundu and co-workers<sup>[59]</sup> used layered  $\text{Zn}_{0.25}\text{V}_2\text{O}_5 \cdot n\text{H}_2\text{O}$  as a cathode material to store  $\text{Zn}^{2+}$ . The specific capacity can reach 300  $\text{mAh g}^{-1}$  and the capacity retention rate was still more than 80% after the cycle life exceeded 1000 times. After that, due to the low cost and multiple oxidation states of vanadium, different kinds of vanadium-based compounds (e.g., vanadium phosphates, vanadium oxides, vanadates, vanadium sulfides, and vanadium nitrides (VNs), etc.) were constructed to store  $\text{Zn}^{2+}$ .<sup>[60–65]</sup> Vanadium-based compounds have higher reversible capacities, better reactivity, and longer cycle lives than  $\text{MnO}_2$  and Prussian blue and its analogs.<sup>[66–69]</sup> In addition, they also have diverse crystal structures, including layered, tunnel, NASICON structure, and so on, which can not only achieve multi-electron transfer, but also help to achieve local electric neutrality and alleviate the polarization problem caused by

$\text{Zn}^{2+}$  intercalation.<sup>[70]</sup> The multiple oxidation states of vanadium (ranging from +2 to +5) and the deformation of V–O polyhedral lead to a variety of different compositions and structural frameworks of vanadium-based compounds constructed by various coordination polyhedral, for instance,  $\text{VO}_4$  tetrahedron,  $\text{VO}_5$  trigonal bipyramid/square pyramid and  $\text{VO}_6$  distorted/regular octahedron (Scheme 3).<sup>[71]</sup> Until now, several types of vanadium-based compounds have been studied as AZIBs cathodes and have shown superior  $\text{Zn}^{2+}$  storage capacity.<sup>[72–75]</sup> However, there are still some key issues for vanadium-based compounds such as complex energy storage mechanisms, low average operating voltage, and unsatisfactory performance. Furthermore, the open framework of vanadium-based compounds is prone to collapse, resulting in the dissolution of vanadium after long cycles.<sup>[76,77]</sup>

In this review, we will introduce different vanadium-based compounds and their applications in AZIBs, such as the preparation methods, crystal structures, electrochemical performances, and energy storage mechanisms (Scheme 4). In the end, further development and prospects of vanadium-based AZIBs cathodes are introduced.

## 2. Vanadium Phosphates

As a special vanadium-based compound, vanadium phosphate can enhance the redox potential of vanadium-based compounds through the induction of polyanion  $\text{PO}_4^{3-}$ .<sup>[78]</sup> In addition, the



**Scheme 2.** Brief history of Zn-based batteries.

strong polarization of  $O^{2-}$  will reduce the M–O covalent bonds and further enhance the transition metal redox potential.<sup>[79]</sup> There are two types of vanadium-based compounds: 1) The layered vanadyl phosphates with large open 2D channel, which provide a wide channel for  $Zn^{2+}$  (de)intercalation processes (e.g., layered  $VOPO_4$ ,  $VO(OH)_2PO_4$ ).<sup>[80]</sup> 2) Vanadium phosphates with high structural stability, interconnected 3D channels, and flexible active sites that can be constructed internally, which are conducive to the transport of  $Zn^{2+}$  (e.g., polyanionic-type and NASICON-type vanadium phosphates).<sup>[81]</sup> The electrochemical properties of some common vanadium phosphates as cathode materials are shown in Table 1.

## 2.1. Vanadyl Phosphates

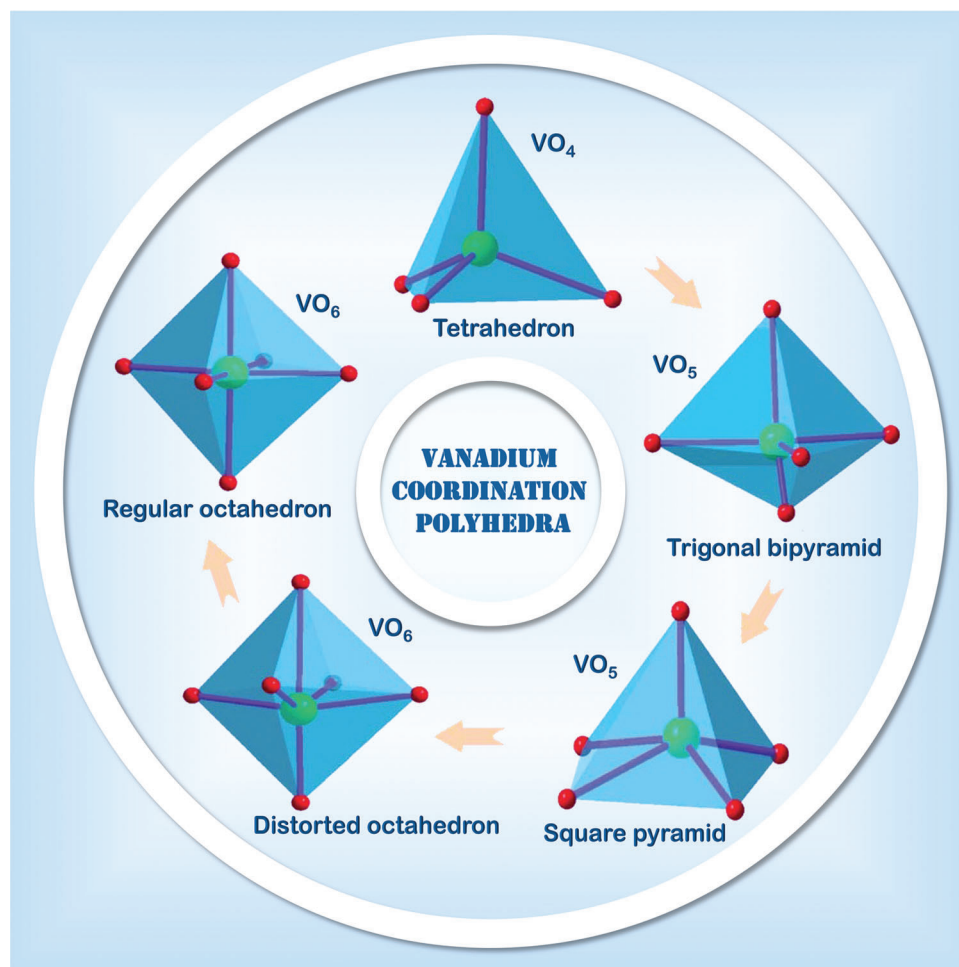
### 2.1.1. $VOPO_4$

Layered  $VOPO_4$ , with typical polyanionic cathodes, has corresponding 2D diffusion channels. Wan et al.<sup>[82]</sup> have developed a highly reversible AZIBs based on layered  $VOPO_4$  cathode and water-electrolyte in salt. The  $VOPO_4$  consists of corner-sharing  $VO_6$  octahedron connected to the  $PO_4$  tetrahedron (Figure 1a).<sup>[83]</sup> Different from  $VOPO_4 \cdot 2H_2O$ , the X-ray diffraction (XRD) pattern

of  $VOPO_4$  showed only (00l) base plane lines and no other (h0l) lines (Figure 1b).  $Zn/VOPO_4$  batteries can be charged directly from the open circuit voltage (point a) to 2.1 V (point b), from which an obvious platform was observed (Figure 1c).

### 2.1.2. The Intercalation of $H_2O$

$VOPO_4 \cdot 2H_2O$ : In addition to  $VOPO_4$ , the most recent progress reveals layered  $VOPO_4 \cdot 2H_2O$  can also be considered as a promising cathode candidate for AZIBs owing to its higher discharge platform from the induction effect.<sup>[38]</sup> The crystal structure of  $VOPO_4 \cdot 2H_2O$  was revealed by Tietze in 1981.<sup>[84]</sup> The structure is described as a superposition of  $VO(OH)_2PO_4$  layers along the c-axis, with water molecules occupying a large layer spacing. In 2018, Wang et al.<sup>[85]</sup> revealed the storage mechanism of layered  $VOPO_4 \cdot 2H_2O$  framework for zinc ions and studied the influence of moisture content on the diffusion ability of  $Zn^{2+}$  in AZIBs system, as well as developing the application of layered  $VOPO_4 \cdot 2H_2O$  in ZIBs cathode for the first time. As shown in Figure 1d,  $H_2O$  migrates from AE into the  $VOPO_4$  lattice, and simultaneously creates a “wet interface” that assists the  $Zn^{2+}$  intercalation, while the dry interface accepts the  $Zn^{2+}$  with significant resistance (see the dotted box). Wu and colleagues<sup>[86]</sup>



**Scheme 3.** Various vanadium coordination polyhedrons (Red O atoms, green V atoms, and pink V–O bonds).

developed a liquid stripping strategy in isopropanol that can introduce a mass of oxygen permeates with high concentration to produce oxygen-rich vacancy bilayer nanosheets with high yield (Figure 1e). The specific capacity of the bilayer-structured  $\text{VOPO}_4 \cdot 2\text{H}_2\text{O}$  cathode is  $313.6 \text{ mAh g}^{-1}$  at  $0.1 \text{ A g}^{-1}$ .

**$\text{VOPO}_4 \cdot x\text{H}_2\text{O}$ :** Layered  $\text{VOPO}_4 \cdot x\text{H}_2\text{O}$ , which can be obtained by cryogenic synthesis procedures, provides adjustable interlaminar spacing to accommodate inserted cations. Shi et al.<sup>[87]</sup> prevented the decomposition and dissolution of  $\text{VOPO}_4 \cdot x\text{H}_2\text{O}$  by the electrolyte containing a high concentration of inexpensive and highly soluble  $\text{ZnCl}_2$  salt. This  $\text{H}^+$  and  $\text{Zn}^{2+}$  sequential intercalation structure provides AZIBs with a high capacity of  $170 \text{ mAh g}^{-1}$ .

Recent studies have shown that the capacity and cycling performance of the cathode can be significantly enhanced by cationic intercalation and organic molecule intercalation to adjust the interlayer structure.<sup>[88,89]</sup>

#### 2.1.3. The Intercalation of $\text{K}^+$

**$\text{KVOPO}_4 \cdot 2\text{H}_2\text{O}$ :** Zhu et al.<sup>[90]</sup> used  $\text{VOPO}_4 \cdot 2\text{H}_2\text{O}$  as a precursor to intercalate  $\text{K}^+$  into the  $\text{VOPO}_4$  layers through ion ex-

change (Figure 1f). At a current density of  $500 \text{ mA g}^{-1}$ ,  $\text{KVOPO}_4$  electrode of AZIBs can achieve over 400 cycles, which shows a superb cycling stability.

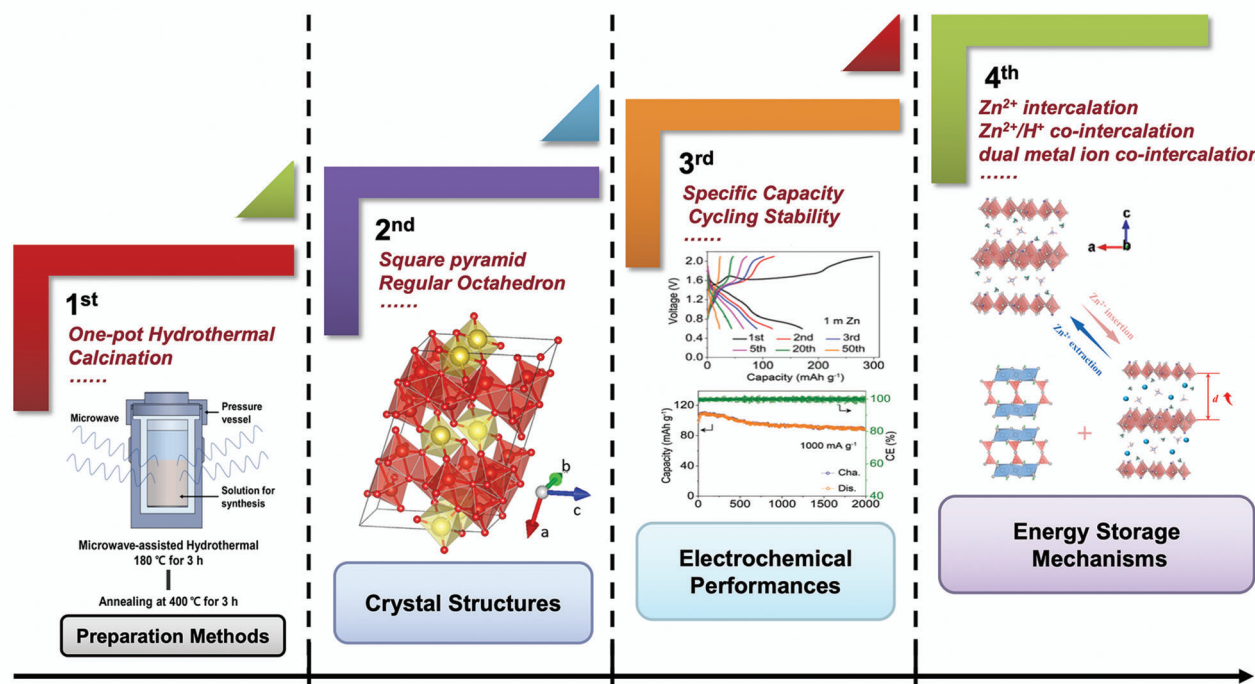
#### 2.1.4. The Intercalation of $\text{Zn}^{2+}$ and $\text{H}_2\text{O}$

**$\text{Zn}_{0.4}\text{VOPO}_4 \cdot 0.8\text{H}_2\text{O}$ :** Cations can partially replace the structural water in  $\text{VOPO}_4 \cdot 2\text{H}_2\text{O}$  or can be inserted directly into  $\text{VOPO}_4$ . Wu and colleagues<sup>[87]</sup> developed a layered phosphate,  $\text{Zn}_{0.4}\text{VOPO}_4 \cdot 0.8\text{H}_2\text{O}$ , by introducing  $\text{Zn}^{2+}$  into the  $\text{VOPO}_4 \cdot 2\text{H}_2\text{O}$  framework (Figure 1g). There is no change in the interlayer  $\text{VOPO}_4$  framework compared to  $\text{VOPO}_4 \cdot 2\text{H}_2\text{O}$  (Figure 1h). At the power density of  $136.2 \text{ W kg}^{-1}$ , the energy density of  $\text{Zn} // \text{Zn}_{0.4}\text{VOPO}_4 \cdot 0.8\text{H}_2\text{O}$  battery reaches up to  $219.8 \text{ Wh kg}^{-1}$ .

#### 2.1.5. The Intercalation of Polypyridine in $\text{VOPO}_4$

Highly conductive organic polymers show the potential for further extending the layer spacing due to the dense charge distribution of intercalated metal ions.<sup>[92]</sup> Vivek Verma and colleagues<sup>[93]</sup> greatly improved the output and long-term capacity retention





**Scheme 4.** Graphical abstract of the introduction of vanadium-based compounds in this review.

**Table 1.** Electrochemical performance of vanadium phosphates as cathodes materials in AZIBs.

Materials	Electrolyte	Specific capacity [mAh g <sup>-1</sup> ] (current density [A g <sup>-1</sup> ])	Capacity retention (cycles numbers)	Voltage range [V]	Ref.
VOPO <sub>4</sub>	21 m LiTFSI + 1 m Zn(Tr) <sub>2</sub>	139 (0.05)	93% (1000)	0.8–2.1	[82]
VOPO <sub>4</sub> ·xH <sub>2</sub> O	13 m ZnCl <sub>2</sub> + 0.8 m H <sub>3</sub> PO <sub>4</sub>	170 (0.1)	≈96% (500)	0.7–1.9	[87]
bilayer-VOP	2 m ZnSO <sub>4</sub>	313.6 (0.1)	76.8% (2000)	0.2–1.9	[86]
KVOPO <sub>4</sub>	4 m Zn(CF <sub>3</sub> SO <sub>3</sub> ) <sub>2</sub>	68 (0.5)	≈100% (400)	0.8–2.0	[90]
Zn <sub>0.4</sub> VOPO <sub>4</sub>	2 m Zn(CF <sub>3</sub> SO <sub>3</sub> ) <sub>2</sub>	161.4 (0.1)	71.4% (1000)	0.2–1.9	[91]
PPy-VOPO <sub>4</sub>	1 m Zn(CF <sub>3</sub> SO <sub>3</sub> ) <sub>2</sub> + Acetonitrile electrolyte with 10 vol% water	86 (0.025)	90.6% (350)	0.5–2.0	[93]
PA-VOP	2 m Zn(CF <sub>3</sub> SO <sub>3</sub> ) <sub>2</sub>	268.2 (0.1)	92.3% (2000)	0.2–1.9	[92]
Li <sub>3</sub> V <sub>2</sub> (PO <sub>4</sub> ) <sub>3</sub>	1 m Zn(ClO <sub>4</sub> ) <sub>2</sub> + Acetonitrile electrolyte with 10.85 vol% water	128 (1 C)	88.7% (1000)	0.7–2.2	[78]
Li <sub>3</sub> V <sub>2</sub> (PO <sub>4</sub> ) <sub>3</sub>	1 m Zn(OTf) <sub>2</sub> + 15 m LiTFSI	126.7 (0.2)	82.3% (2000)	0.6–2.1	[108]
Li <sub>3</sub> V <sub>2</sub> (PO <sub>4</sub> ) <sub>3</sub>	1 m Li <sub>2</sub> SO <sub>4</sub> + 2 m ZnSO <sub>4</sub>	128 (0.2 C)	85.4% (200)	0.7–2.1	[107]
Li <sub>3</sub> V <sub>2</sub> (PO <sub>4</sub> ) <sub>3</sub>	2 m Zn(OTf) <sub>2</sub> with 70 wt.% Polyethylene glycol 400	≈80 (0.5 C)	83.5% (100)	0.2–1.9	[109]
Li <sub>3</sub> V <sub>2</sub> (PO <sub>4</sub> ) <sub>3</sub>	1 m Zn(CF <sub>3</sub> SO <sub>3</sub> ) <sub>2</sub> + 20 m LiTFSI	111 (0.2)	93.6% (100)	0.7–1.7	[134]
Li <sub>3</sub> V <sub>2</sub> (PO <sub>4</sub> ) <sub>3</sub> @C	2 m ZnSO <sub>4</sub> + 1 m Li <sub>2</sub> SO <sub>4</sub>	95 (2 C)	91% (50)	0.7–1.7	[81]
Na <sub>3</sub> V <sub>2</sub> (PO <sub>4</sub> ) <sub>3</sub>	2 m ZnSO <sub>4</sub> + 1 m Li <sub>2</sub> SO <sub>4</sub>	96 (0.2 C)	84.1% (200)	0.7–2.1	[107]
Na <sub>3</sub> V <sub>2</sub> (PO <sub>4</sub> ) <sub>3</sub>	Zn(CF <sub>3</sub> SO <sub>3</sub> ) <sub>2</sub> in triethyl phosphate	74 (0.5)	≈100% (600)	0.6–1.8	[113]
Na <sub>3</sub> V <sub>2</sub> (PO <sub>4</sub> ) <sub>3</sub>	0.5 m Zn(CH <sub>3</sub> CO <sub>2</sub> ) <sub>2</sub>	90 (0.1)	80% (100)	0.6–1.8	[135]
Na <sub>3</sub> V <sub>2</sub> (PO <sub>4</sub> ) <sub>3</sub>	2 m ZnOTf <sub>2</sub> + 1 m NaOTf with polyethylene glycol	90 (0.05)	66.7% (300)	0.6–1.8	[136]
Na <sub>3</sub> V <sub>2</sub> (PO <sub>4</sub> ) <sub>3</sub> /C	0.5 m Zn(CH <sub>3</sub> OO) <sub>2</sub>	97 (0.5 C)	74% (100)	0.8–1.7	[102]
Na <sub>3</sub> V <sub>2</sub> (PO <sub>4</sub> ) <sub>3</sub> /C	0.5 MCH <sub>3</sub> OONa + Zn(CH <sub>3</sub> OO) <sub>2</sub> solution	92 (0.05)	77% (200)	0.5–1.7	[112]
Na <sub>3</sub> V <sub>2</sub> (PO <sub>4</sub> ) <sub>3</sub> /rGO	2 m Zn(CF <sub>3</sub> SO <sub>3</sub> ) <sub>2</sub>	114 (0.05)	75% (200)	0.6–1.8	[114]
Sr-doped Na <sub>3</sub> V <sub>2</sub> (PO <sub>4</sub> ) <sub>3</sub>	Hydrated gel electrolyte	108 (0.5 C)	96.2% (400)	(–0.13)–2.6	[115]
Na <sub>3</sub> V <sub>2</sub> (PO <sub>4</sub> ) <sub>3</sub> O <sub>1.6</sub> F <sub>1.4</sub>	25 m ZnCl <sub>2</sub> + 5 m NH <sub>4</sub> Cl	155 (0.05)	73.5% (7000)	0.2–1.4	[128]

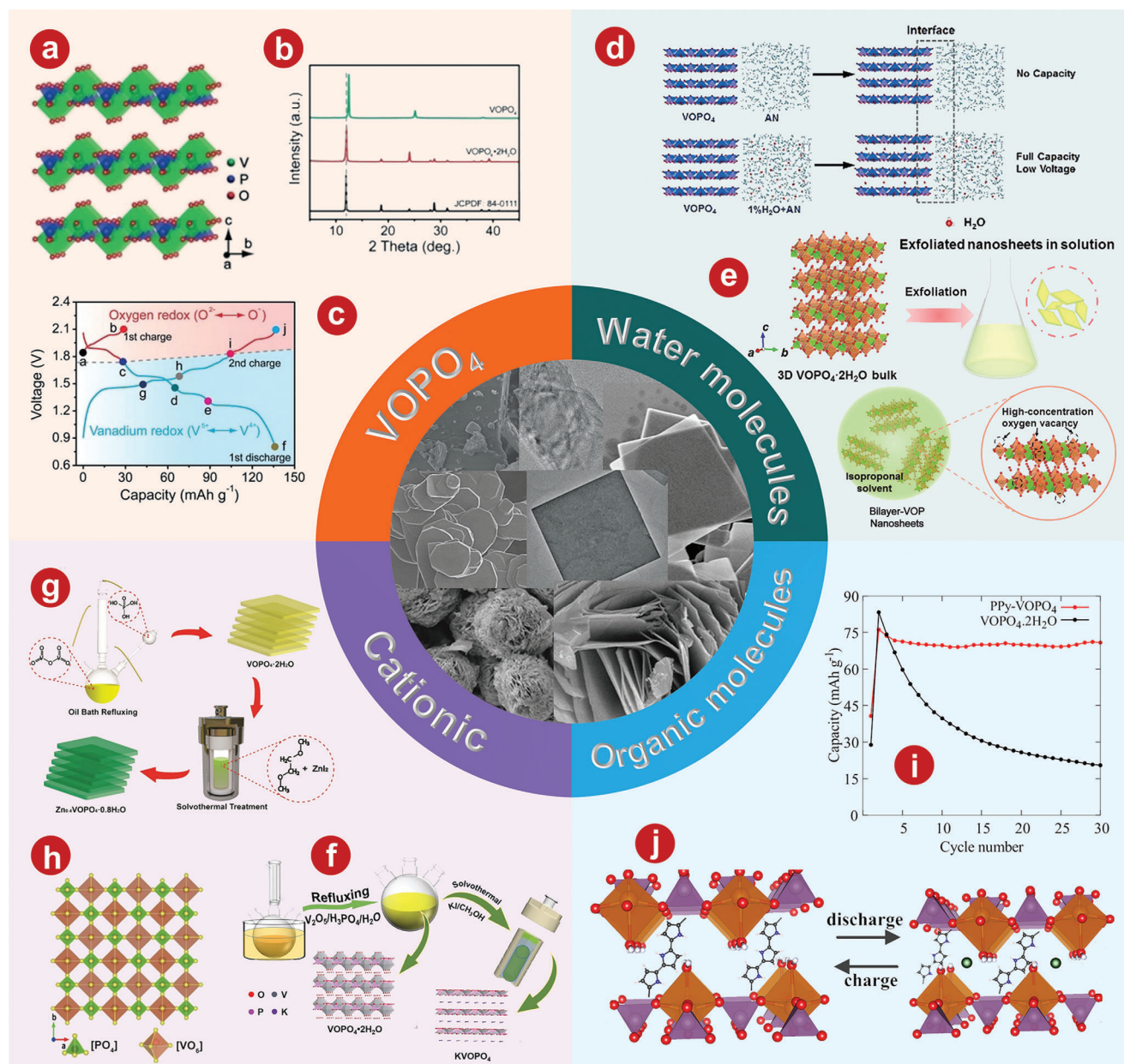


**Figure 1.** a) Crystal structure of  $\text{VOPO}_4$ . b) XRD patterns of  $\text{VOPO}_4 \cdot 2\text{H}_2\text{O}$  and  $\text{VOPO}_4$ . c) Charge/discharge curves of  $\text{Zn}/\text{VOPO}_4$  batteries at  $0.05 \text{ A g}^{-1}$ . d) Schematic illustrations of  $\text{VOPO}_4$  in  $0.1 \text{ M Zn}(\text{OTf})_2\text{-AN}$  without water (top) and with  $1\% \text{ H}_2\text{O}$  (bottom). e) Schematic of liquid-phase exfoliation and predictable oxygen vacancy formation in bilayer-structured  $\text{VOPO}_4 \cdot 2\text{H}_2\text{O}$  nanosheets. f) Schematic illustration for the preparation process of  $\text{KVOPO}_4$ . g) Schematic illustration of the  $\text{Zn}^{2+}$  incorporation in layered  $\text{VOPO}_4 \cdot 2\text{H}_2\text{O}$  by an appropriate solvothermal process. h) SXRD pattern of the  $\text{Zn}_{0.4}\text{VOPO}_4 \cdot 0.8\text{H}_2\text{O}$  single crystal along the  $b$ -axis. i) Comparison of the cycling stabilities for  $\text{VOPO}_4 \cdot 2\text{H}_2\text{O}$  and  $\text{PPy-VOPO}_4$  at a current rate of  $30 \text{ mA g}^{-1}$  in  $1 \text{ M Zn}(\text{CF}_3\text{SO}_3)_2/\text{acetonitrile}$  electrolyte with  $10 \text{ vol } \%$  water. j) Schematic depicting overall mechanism of zinc intercalation or deintercalation processes into the  $\text{PPy-VOPO}_4$  host structure. Green spheres indicate  $\text{Zn}^{2+}$  ions. a–c) Reproduced with permission.<sup>[82]</sup> Copyright 2019, Wiley-VCH. d) Reproduced with permission.<sup>[85]</sup> Copyright 2018, Wiley-VCH. e) Reproduced with permission.<sup>[86]</sup> Copyright 2021, Wiley-VCH. f) Reproduced with permission.<sup>[86]</sup> Copyright 2021, Elsevier. g, h) Reproduced with permission.<sup>[87]</sup> Copyright 2020, American Chemical Society. i, j) Reproduced with permission.<sup>[93]</sup> Copyright 2019, American Chemical Society.

of AZIBs by the pre-intercalation of polypyridine between crystalline layers and using water-controlled electrolytes. Comparison of cyclic stability between  $\text{VOPO}_4 \cdot 2\text{H}_2\text{O}$  and  $\text{PPy-VOPO}_4$  was shown in Figure 1i. Obviously,  $\text{PPy-VOPO}_4$  had better capacity retention. As shown in Figure 1j, the mechanisms can be inferred through the study of structural characterization.

## 2.2. NASICON-Type Phosphates

NASICON-type phosphates ( $\text{M}_3\text{V}_2(\text{PO}_4)_3$  ( $\text{M} = \text{Li}, \text{Na}, \text{K}$ )) with sodium superionic conductor structure have a highly covalent 3D host framework with rich clearance space, allowing efficient diffusion of ions.<sup>[94–98]</sup> In recent years, the NASICON-type

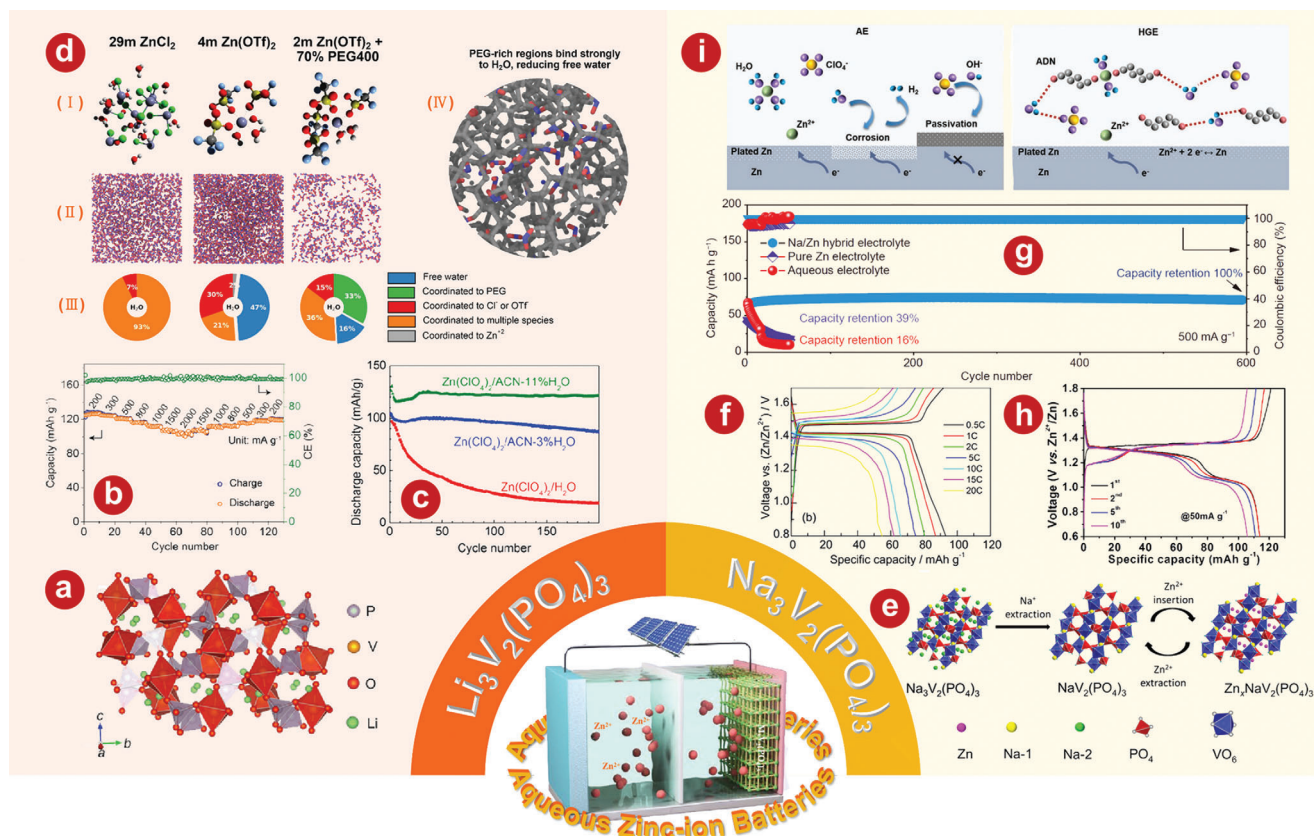


**Figure 2.** a) Schematic illustration of the  $\text{Li}_3\text{V}_2(\text{PO}_4)_3$  crystal structure. b) Rate performance of the  $\text{Li}_3\text{V}_2(\text{PO}_4)_3$  cathode in 1 mol  $\text{kg}^{-1}$  Zn + 15 mol  $\text{kg}^{-1}$  Li electrolyte. c) Cycling stability of the  $\text{Li}_3\text{V}_2(\text{PO}_4)_3$  electrode at the 200th cycle in Zn cells with different electrolytes at 2C. d) Electrolyte structure in 29 mol  $\text{kg}^{-1}$   $\text{ZnCl}_2$ , 4 mol  $\text{kg}^{-1}$   $\text{Zn}(\text{OTf})_2$ , and 70PEG electrolytes. (I) Typical  $\text{Zn}^{2+}$  solvation structures. (II) Simulation snapshots showing only the water molecules. (III) Distribution of water populations. (IV) Water molecules absorbed into the PEG-rich region of the 70PEG electrolyte. e) Schematic representation for phase transition of  $\text{Na}_3\text{V}_2(\text{PO}_4)_3$  cathode during cycling. f) Charge-discharge curves of the system at different C rates of the Zn/ $\text{Na}_3\text{V}_2(\text{PO}_4)_3$  battery. g) The comparison of long-term cycle performance at a current of 500  $\text{mA g}^{-1}$  in different electrolytes. h) Charge/discharge curves of  $\text{Na}_3\text{V}_2(\text{PO}_4)_3$ @reduced graphene oxide composites at 50  $\text{mA g}^{-1}$ . i) Schematic illustration of  $\text{Zn}^{2+}$  solvation structure and corresponding interfacial reactions in AE and HGE. a, b) Reproduced with permission.<sup>[108]</sup> Copyright 2021, The Royal Society of Chemistry. c) Reproduced with permission.<sup>[78]</sup> Copyright 2021, The Royal Society of Chemistry. d) Reproduced with permission.<sup>[109]</sup> Copyright 2022, American Chemical Society. e) Reproduced with permission.<sup>[102]</sup> Copyright 2016, Elsevier. f) Reproduced with permission.<sup>[112]</sup> Copyright 2016, Elsevier. g) Reproduced with permission.<sup>[113]</sup> Copyright 2021, Springer. h) Reproduced with permission.<sup>[114]</sup> Copyright 2019, Wiley-VCH. i) Reproduced with permission.<sup>[115]</sup> Copyright 2021, Wiley-VCH.

phosphate structure has been used as cathode materials to store monovalent metal ions, such as  $\text{Li}^+$ ,  $\text{Na}^+$ , and  $\text{K}^+$ .<sup>[99–101]</sup> Relevant studies show that the radius of  $\text{Na}^+$  (0.98 Å) is larger than that of  $\text{Zn}^{2+}$  (0.74 Å), indicating that  $\text{Zn}^{2+}$  has great potential in the framework of NASICON-type phosphates.<sup>[102]</sup> In addition, the NASICON-type phosphate structure has a higher energy density and redox potential than the homologous vanadium oxides because of the strong indelible effect of  $\text{PO}_4^{3-}$  polyanion and the strong P–O bond.<sup>[87]</sup>

### 2.2.1. $\text{Li}_3\text{V}_2(\text{PO}_4)_3$

$\text{Li}_3\text{V}_2(\text{PO}_4)_3$  has two kinds of framework structure distinguished by the connection of “lantern” element  $[\text{V}_2(\text{PO}_4)_3]$ , namely rhomboid phase and monoclinic phase.<sup>[103–105]</sup> Structural differences result in their various electrochemical performances. However, the three mobile  $\text{Li}^+$  in the monoclinic phase make electrochemical performance of monoclinic phase better than that of the

rhomboid phase, which leads to greater research value.<sup>[106]</sup> In 2016, Zhao et al.<sup>[107]</sup> demonstrated the feasibility of  $\text{Li}_3\text{V}_2(\text{PO}_4)_3$  for AZIBs, which aroused great interest among researchers. Li and colleagues<sup>[108]</sup> demonstrated that the capacity decay and voltage drop problems of the  $\text{Li}_3\text{V}_2(\text{PO}_4)_3$  cathode were significantly solved when using a concentrated AE based on zinc and lithium salts. **Figure 2a** illustrates the crystal structure of  $\text{Li}_3\text{V}_2(\text{PO}_4)_3$ . The rate performance of  $\text{Li}_3\text{V}_2(\text{PO}_4)_3$  indicates that a high capacity of 100.5  $\text{mA h g}^{-1}$  is achieved at 2000  $\text{mA g}^{-1}$  (Figure 2b). Li et al.<sup>[78]</sup> took advantage of the optimal solvent combination of water and acetonitrile in the electrolyte, which can effectively prevent the dissolution or decomposition of  $\text{Li}_3\text{V}_2(\text{PO}_4)_3$  into vanadium oxide without sacrificing the disinsertion and insertion kinetics of  $\text{Zn}^{2+}$ . To enhance the conductivity, rGO was added to  $\text{Li}_3\text{V}_2(\text{PO}_4)_3$ . In  $\text{Zn}(\text{ClO}_4)_2/\text{acetonitrile} \approx 11\% \text{ H}_2\text{O}$  electrolytes, its performance is further improved. The initial capacity of the electrode reaches 125  $\text{mA h g}^{-1}$  and remains at 121  $\text{mA h g}^{-1}$  after 200 cycles. In addition, Li and coworkers<sup>[109]</sup> focused on the inhibition of harmful  $\text{H}^+$  intercalation by adjusting the



solvation structure with  $\text{Li}_3\text{V}_2(\text{PO}_4)_3$  as the model cathode. Electrolyte structure in 29 mol  $\text{kg}^{-1}$   $\text{ZnCl}_2$ , 4 mol  $\text{kg}^{-1}$   $\text{Zn}(\text{OTf})_2$ , and 70 PEG electrolytes is shown in Figure 2d. The novel PEG hybrid electrolyte not only has a good inhibition of  $\text{H}^+$  intercalation, but also has high reversible plating/stripping performance, with a CE value of 99.7% after 150 cycles.

### 2.2.2. $\text{Na}_3\text{V}_2(\text{PO}_4)_3$

Different from  $\text{Li}_3\text{V}_2(\text{PO}_4)_3$ , the basic frame structure of  $\text{Na}_3\text{V}_2(\text{PO}_4)_3$  with rhomboid phase is  $\text{VO}_6$  octahedron and  $\text{PO}_4$  tetrahedron, which share angular connection. There are two kinds of sodium ions in the crystal structure, in which each  $\text{PO}_4$  tetrahedron is connected by two  $\text{VO}_6$  octahedrons and sodium 1, while sodium 2 is located only between the two  $\text{VO}_6$  octahedrons.<sup>[110]</sup> By comparing the length of the sodium-oxygen bond, it was found that the occupancy rate of sodium 2 was smaller than that of sodium 1, which made the corresponding sodium ion easier to be extracted in the electrochemical process.<sup>[111]</sup> Huang's group<sup>[102]</sup> first developed  $\text{Na}_3\text{V}_2(\text{PO}_4)_3$  with NASICON structure as the cathode material of AZIBs. Phase transition diagram of  $\text{Na}_3\text{V}_2(\text{PO}_4)_3$  cathode cycle is shown in Figure 2e.  $\text{Na}_3\text{V}_2(\text{PO}_4)_3$  has great potential as cathode materials of AZIBs, which show excellent rates and cyclic performances. In addition, Huang's group<sup>[112]</sup> enhanced the electrochemical properties of  $\text{Na}_3\text{V}_2(\text{PO}_4)_3$  by co-incorporating carbon and reduced graphene oxide (rGO). This aqueous hybrid battery, which uses carbon-rGO- $\text{Na}_3\text{V}_2(\text{PO}_4)_3$  composite as cathode, has a capacity of 92 mAh  $\text{g}^{-1}$  and a high and flat operating voltage of 1.42 V at a current density of 50 mA  $\text{g}^{-1}$  (Figure 2f). Li et al.<sup>[113]</sup> systematically studied the capacity degradation mechanism of  $\text{Na}_3\text{V}_2(\text{PO}_4)_3$  and proposed a new organic double salt electrolyte that achieved good cyclic stability of 600 cycles at 500 mA  $\text{g}^{-1}$  without a capacity loss (Figure 2g). Hu and his colleagues<sup>[114]</sup> demonstrated that  $\text{Na}_3\text{V}_2(\text{PO}_4)_3$ @rGO microspheres have a simultaneous  $\text{Zn}^{2+}/\text{Na}^+$  (de)intercalation behavior in a single-component 2.0 M  $\text{Zn}(\text{CF}_3\text{SO}_3)_2$  electrolyte. As shown in Figure 2h, the average discharge platform of  $\text{Na}_3\text{V}_2(\text{PO}_4)_3$ @rGO microspheres at 50 mA  $\text{g}^{-1}$  is 1.23 V. Lin et al.<sup>[115]</sup> developed a dual-function AZIB hydration gel electrolyte with NASICON-type strontium-doped  $\text{Na}_3\text{V}_2(\text{PO}_4)_3$  as the cathode, which can effectively reduce the para-reaction of water at the cathode. Solvation structure and interfacial reaction diagram of  $\text{Zn}^{2+}$  in AE and hydrated gel electrolyte (HGE) is shown in Figure 2i. Using the NASICON-type strontium-doped  $\text{Na}_3\text{V}_2(\text{PO}_4)_3$  as the cathode, the AZIBs can achieve more than 8000 cycles at 10 C, and still maintain the high capacity of 90 mAh  $\text{g}^{-1}$ .

### 2.2.3. $\text{K}_3\text{V}_2(\text{PO}_4)_3$

With the successful application of homologous  $\text{Li}_3\text{V}_2(\text{PO}_4)_3$  and  $\text{Na}_3\text{V}_2(\text{PO}_4)_3$  cathodes,  $\text{K}_3\text{V}_2(\text{PO}_4)_3$  has attracted extensive attention.<sup>[116,117]</sup> However, at present, relevant applications are concentrated in LIBs and sodium-ion batteries, and there is no application in AZIBs with excellent electrochemical performance.  $\text{K}_3\text{V}_2(\text{PO}_4)_3$  is expected to be widely used in AZIBs in the future.

## 2.3. NASICON-Type Phosphate Analogs

Basic studies on  $\text{Li}_3\text{V}_2(\text{PO}_4)_3$  and  $\text{Na}_3\text{V}_2(\text{PO}_4)_3$  have shown that NASICON-type materials have suitable diffusion channels and guest ion attachment sites and have the storage capacity of  $\text{Zn}^{2+}$ .  $\text{Na}_3\text{V}_2(\text{PO}_4)_2\text{F}_3$ , as an outstanding representative of NASICON-type phosphate analogs, has the advantages of high energy density, interstitial spaces, and good structural stability.<sup>[118,119]</sup> As the F–V bond is more ionic than the O–V bond, the working potential of  $\text{Na}_3\text{V}_2(\text{PO}_4)_2\text{F}_3$  is reported to be as high as  $\approx 3.9$  V and the energy density as high as  $\approx 500$  Wh  $\text{kg}^{-1}$ .<sup>[120]</sup>  $\text{Na}_3\text{V}_2(\text{PO}_4)_2\text{F}_3$  with *Amam* space group belongs to orthorhombic crystal system, which is composed of  $[\text{V}_2\text{O}_8\text{F}_3]$  bi-octahedron and  $[\text{PO}_4]$  tetrahedron units. The bi-octahedron units are connected by F atoms, while the  $[\text{PO}_4]$  units are connected by oxygen atoms.<sup>[121,122]</sup> The charge and discharge process is usually accompanied by the redox of transition metal ions in the crystal structure, so the diffusion path of electrons in  $\text{Na}_3\text{V}_2(\text{PO}_4)_2\text{F}_3$  depends on the interconnection between the  $[\text{V}_2\text{O}_8\text{F}_3]$  bi-octahedron.<sup>[123]</sup> Li et al.<sup>[124]</sup> developed an AZIB based on a novel intercalated  $\text{Na}_3\text{V}_2(\text{PO}_4)_2\text{F}_3$  cathode, a carbon film functionalized Zn anode, as well as a 2 M  $\text{Zn}(\text{CF}_3\text{SO}_3)_2$  electrolyte. The zinc storage mechanism is illustrated in Figure 3a. When the discharge rate increases sharply from 0.2 to 3 A  $\text{g}^{-1}$ , the AZIB shows a good discharge platform and a small voltage drop (Figure 3b). Min Je Pai and coworkers<sup>[125]</sup> focused on charge storage mechanisms of Non-AZIBs and AZIBs with  $\text{Na}_3\text{V}_2(\text{PO}_4)_2\text{F}_3$  as cathode material. The electrochemical cycling and ex situ analyses of the  $\text{Na}_3\text{V}_2(\text{PO}_4)_2\text{F}_3/\text{C}$  cathode reveal a completely contrasting electrochemical behavior between Non-AZIBs and AZIBs due to the difference in the guest ion for the faradaic reactions during the cycle.

$\text{Na}_3\text{V}_2(\text{PO}_4)_2\text{F}_3$  has been widely studied in materials with the molecular formula  $\text{Na}_3\text{V}_2(\text{PO}_4)_2\text{F}_{3-2y}\text{O}_{2y}$  ( $0 \leq y \leq 1$ ). However, replacing part of  $\text{F}^-$  with  $\text{O}^{2-}$  reduces the induction effect caused by  $\text{F}^-$ , resulting in higher ionic conductivity and lower polarization of  $\text{Na}_3\text{V}_2(\text{PO}_4)_2\text{O}_2\text{F}$  composed of  $\text{V}^{4+}$ . Wang and colleagues<sup>[126]</sup> developed an AZIBs consisting of a novel nitrogen-doped carbon inserted layered  $\text{MoO}_2$  material ( $\text{MoO}_2@\text{NC}$ ) as the intercalated anode and  $\text{Na}_3\text{V}_2(\text{PO}_4)_2\text{O}_2\text{F}$  as the cathode. The preparation of  $\text{MoO}_2@\text{NC}$  is shown in Figure 3c. The capacity of  $\text{MoO}_2@\text{NC}||\text{Zn}-\text{Na}_3\text{V}_2(\text{PO}_4)_2\text{O}_2\text{F}$  full cell remained at 78 mAh  $\text{g}^{-1}$  with a high-capacity retention of 93% even after 200 cycles.

In addition,  $\text{Na}_3\text{V}_2(\text{PO}_4)_2\text{O}_{1.6}\text{F}_{1.4}$  ( $\text{V}^{3.8+}$ ) provides an additional 0.4 electrons per formula unit compared to  $\text{V}^{4+}/\text{V}^{5+}$  single-electron transfer in  $\text{Na}_3\text{V}_2(\text{PO}_4)_2\text{O}_2\text{F}$ .<sup>[127]</sup> Therefore, this hybrid valency vanadium compound may exhibit a higher reversible capacity as cathode material of AZIBs. Ni et al.<sup>[128]</sup> developed a neutral water-in-bisalts electrolyte of 25 mol  $\text{kg}^{-1}$   $\text{ZnCl}_2$  + 5 mol  $\text{kg}^{-1}$   $\text{NH}_4\text{Cl}$  to enhance the electrochemical performance of  $\text{Na}_3\text{V}_2(\text{PO}_4)_2\text{O}_{1.6}\text{F}_{1.4}$  coated with rGO (5 wt.%) as a novel AZIBs cathode. The crystal structure of  $\text{Na}_3\text{V}_2(\text{PO}_4)_2\text{O}_{1.6}\text{F}_{1.4}$  is shown in Figure 3e. The  $\text{PO}_4$  tetrahedron and the  $\text{VO}_5\text{F}/\text{VO}_4\text{F}_2$  octahedron (including  $\text{V}^{4+}$  and  $\text{V}^{3+}$ ) share oxygen atoms to form an open framework. In addition,  $\text{VO}_5\text{F}$  and  $\text{VO}_4\text{F}_2$  octahedrons are bridged by F atoms. At 50 mA  $\text{g}^{-1}$ , the reversible capacity is 155 mAh  $\text{g}^{-1}$  (Figure 3f), the average operating potential is 1.46 V, as well as the stable circulation can achieve 7000 cycles at 2 A  $\text{g}^{-1}$  (Figure 3g).



NASICON-type phosphate analogues

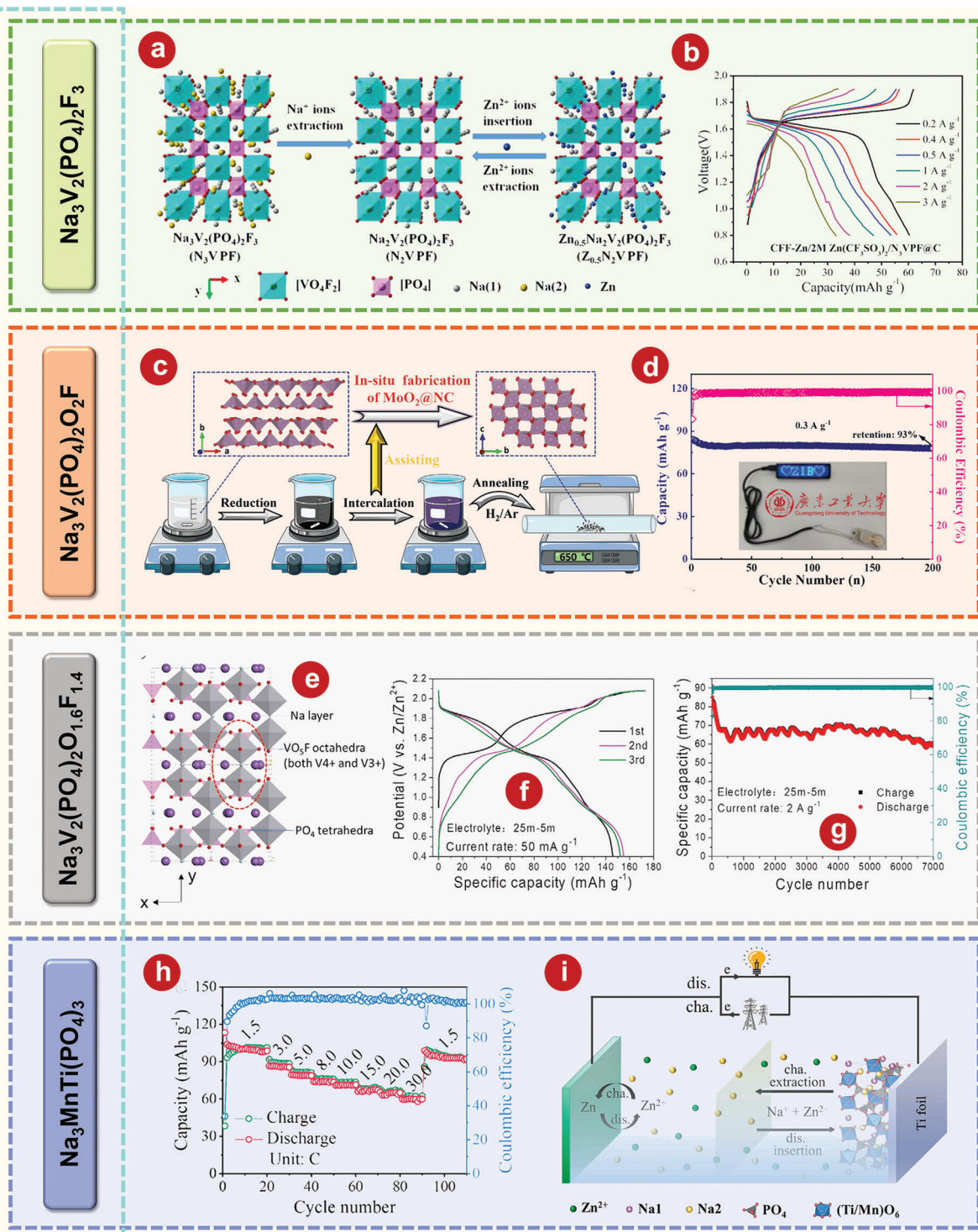
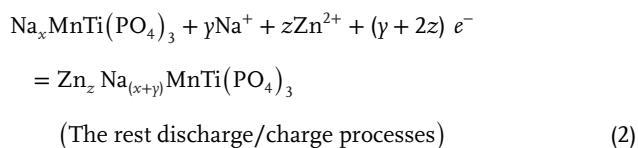
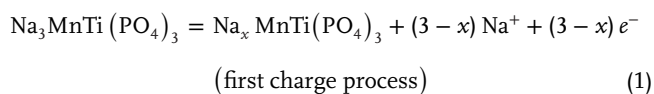


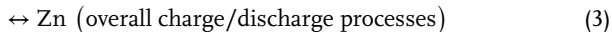
**Figure 3.** a) Schematic illustration of Zinc storage mechanism. b) Charge/discharge profiles of carbon film functionalizing-Zn// $\text{Na}_3\text{V}_2(\text{PO}_4)_2\text{F}_3$ @C battery at various current densities from 0.2 to 3  $\text{A g}^{-1}$ . c) Illustration of synthesis process of  $\text{MoO}_2$ @NC. d) Cycling performance of  $\text{MoO}_2$ @NC||Zn- $\text{Na}_3\text{V}_2(\text{PO}_4)_2\text{O}_2\text{F}$  full cell at 0.3  $\text{A g}^{-1}$ . e) Schematic of the crystal structure of  $\text{Na}_3\text{V}_2(\text{PO}_4)_2\text{F}_{1.4}$ . f) The initial galvanostatic charge/discharge profiles of the  $\text{Na}_3\text{V}_2(\text{PO}_4)_2\text{O}_{1.6}\text{F}_{1.4}$  electrode in the 25 mol  $\text{kg}^{-1}$  + 5 mol  $\text{kg}^{-1}$  electrolyte at a current rate of 50  $\text{mA g}^{-1}$ . g) The cycling performance of  $\text{Na}_3\text{V}_2(\text{PO}_4)_2\text{O}_{1.6}\text{F}_{1.4}$  electrode in the 25 mol  $\text{kg}^{-1}$  + 5 mol  $\text{kg}^{-1}$  electrolyte at a current rate of 2  $\text{A g}^{-1}$ . h) Rate capability of the Zn// $\text{Na}_3\text{MnTi}(\text{PO}_4)_3$  battery from 1.5 to 30.0 C. i) Schematic illustration of aqueous rechargeable hybrid Zn// $\text{Na}_3\text{MnTi}(\text{PO}_4)_3$  battery during charge and discharge processes. a, b) Reproduced with permission.<sup>[124]</sup> Copyright 2018, Elsevier. c, d) Reproduced with permission.<sup>[126]</sup> Copyright 2021, Wiley-VCH. e-g) Reproduced with permission.<sup>[128]</sup> Copyright 2020, Wiley-VCH. h, i) Reproduced with permission.<sup>[133]</sup> Copyright 2021, Elsevier.

$\text{Na}_3\text{MnTi}(\text{PO}_4)_3$ , as a typical analog of sodium superconductor NASICON-typed  $\text{Na}_3\text{V}_2(\text{PO}_4)_3$ , has been regarded as a promising cathode material. Although  $\text{Na}_3\text{MnTi}(\text{PO}_4)_3$  doesn't belong to vanadium-based compounds, compared with vanadium, transition metals manganese and titanium have the advantages of low price, low toxicity, and rich resources.<sup>[129–132]</sup> The new environmentally friendly water-based rechargeable hybrid sodium/zinc battery developed by Zhou et al.<sup>[133]</sup> uses zinc as anode,  $\text{Na}_3\text{MnTi}(\text{PO}_4)_3$  as cathode, as well as 0.5 M  $\text{CH}_3\text{COONa}$  and  $\text{Zn}(\text{CH}_3\text{COO})_2$  as mixed electrolytes. After 50 cycles at 1.5 C, the discharge capacity remains at 95.0 mAh g<sup>-1</sup>, the capacity retention rate is 84.6%, and the CE is 103.5% (Figure 3h). The schematic diagram (Figure 3i) of the electrochemical reaction between  $\text{Zn}/\text{Na}_3\text{MnTi}(\text{PO}_4)_3$  and every single electrode is shown below:

Cathode reaction:



Anodic reaction:  $\text{Zn}^{2+} + 2e^-$



### 3. Vanadium Oxides

Vanadium oxides have been widely used due to their various oxidation states and large open crystal structure, which is favorable for metal ion (de)intercalation.<sup>[137–139]</sup> Vanadium oxides have various oxidation states, different composition forms, and diverse coordination polyhedron, which provide many paths for  $\text{Zn}^{2+}$  (de)intercalation.<sup>[140]</sup> In recent years, vanadium oxides have attracted much attention in AZIBs due to their high specific capacity, wide availability, and low cost.<sup>[141]</sup> In addition, some electrochemical performance of vanadium oxides as cathode materials are shown in Table 2.

#### 3.1. $\text{VO}_2$

$\text{VO}_2$  is a kind of metal oxide with phase transformation. The structure changes before and after phase transformation lead to the reversible transformation of infrared light from transmission to reflection.<sup>[142]</sup> In addition,  $\text{VO}_2$  has d<sup>1</sup> electronic system, and there are many different crystal types, including thermodynamically stable rutile  $\text{VO}_2(\text{R})$ , monoclinic  $\text{VO}_2(\text{M})$  and metastable tetragonal  $\text{VO}_2(\text{A})$ , monoclinic  $\text{VO}_2(\text{B})$ ,  $\text{VO}_2(\text{C})$ , and  $\text{VO}_2(\text{D})$ .<sup>[143]</sup> Although the chemical formula is the same, their crystal structure and electronic structure are completely different and complicated, and the application scenarios are different. Metastable monoclinic  $\text{VO}_2(\text{B})$  has been widely used as a cathode material for AZIBs due to its open framework.<sup>[144–146]</sup> In 2018, Park

et al.<sup>[144]</sup> first proposed using  $\text{VO}_2(\text{B})$  as a cathode material of AZIBs and verified its feasibility through first-principles calculation. The crystal structure of  $\text{VO}_2(\text{B})$  is shown in Figure 4a. The team successfully synthesized  $\text{VO}_2(\text{B})$  by low-temperature solvothermal method, which was then combined with rGO to form  $\text{VO}_2(\text{B})/\text{rGO}$ .<sup>[144]</sup> Electrochemical tests were carried out on the  $\text{VO}_2(\text{B})$  and  $\text{VO}_2(\text{B})/\text{rGO}$  composite materials, and it was obvious that the electrochemical performance of the composite materials was significantly improved by rGO (Figure 4b). By in situ XRD and various electrochemical measurements, Ding and colleagues<sup>[60]</sup> demonstrated the pseudo-capacitance behavior and ultra-fast kinetics of a unique tunnel of zinc ions embedded  $\text{VO}_2(\text{B})$  nanofibers in an aqueous  $\text{Zn}(\text{CF}_3\text{SO}_3)_2$  electrolyte. The as-prepared  $\text{VO}_2(\text{B})$  nanofiber cathode has a highly stable reversible capacity of 357 mAh g<sup>-1</sup> at 0.25 C (Figure 4c).

Metastable  $\text{VO}_2(\text{D})$  has also been synthesized as a cathode material for AZIBs. Wei et al.<sup>[147]</sup> first studied the zinc storage performance of metastable  $\text{VO}_2(\text{D})$  as a cathode material of ZIBs. Their team demonstrated an interesting electrochemically induced phase transition from monoclinic  $\text{VO}_2$  to bilayer  $\text{V}_2\text{O}_5 \cdot n\text{H}_2\text{O}$ , with significantly increased interlayer spacing and reduced structural order during the initial (de)intercalation of  $\text{Zn}^{2+}$ , with good structural stability in subsequent cycles. The corresponding discharge/charge profiles show the  $\text{VO}_2(\text{D})$  cathode has superior rate performance, among which the best capacity is 274 mAh g<sup>-1</sup> at 0.1 A g<sup>-1</sup> (Figure 4d). Furthermore, by measuring and comparing the power and energy density of state-of-the-art power supplies (Figure 4e), it can be seen that the  $\text{VO}_2$ -based AZIBs system provides excellent electrochemical performance.<sup>[46,59,148,149]</sup> Chen and colleagues<sup>[150]</sup> developed  $\text{VO}_2(\text{D})$  hollow nanospheres as ZIBs cathode materials, which have a high reversible discharge capacity of 408 mAh g<sup>-1</sup> at 0.1 A g<sup>-1</sup> in 3 M  $\text{ZnSO}_4$  electrolyte (Figure 4f), and long cyclic endurance stability stable can reach up to 30 000 cycles with the capacity attenuation rate of 0.0023% each cycle.

$\text{VO}_2(\text{M})$  is composed of twisted  $[\text{VO}_6]$  octahedrons, in which  $[\text{VO}_6]$  octahedrons are staggered and connected into a network by sharing O atoms, forming a tunnel about 0.318 nm long.<sup>[151]</sup> Importantly,  $\text{VO}_2(\text{M})$  phase can be obtained by a simple heat treatment of  $\text{VO}_2(\text{B})$ .<sup>[152]</sup> Compared with  $\text{VO}_2(\text{B})$  and  $\text{VO}_2(\text{D})$ ,  $\text{VO}_2(\text{M})$  has a denser tunnel and higher space utilization, which facilitates ion migration. In addition, it is found that  $\text{VO}_2(\text{M})$  has better thermal stability. Zhang et al.<sup>[153]</sup> first prepared  $\text{VO}_2(\text{M})$  integrated with carbon nanotubes (CNTs) as AZIBs cathode. As shown in Figure 4g, the as-prepared binder-free cathode delivers excellent stability with 84.5% retention after 5000 cycles at 20 A g<sup>-1</sup>. The electrochemical reaction of the  $\text{Zn}/\text{VO}_2(\text{M})$  battery (Figure 4h) in the aqueous  $\text{ZnSO}_4$  electrolyte solution is as follows:



#### 3.2. $\text{V}_2\text{O}_3$

$\text{V}_2\text{O}_3$  is considered as a high-capacity electrochemical energy storage material because it shares an edge with the adjacent octahedron through two common  $\text{VO}_6$  octahedra to form a 3D

**Table 2.** Electrochemical performance of vanadium oxides as cathodes in AZIBs.

Materials	Electrolyte	Specific capacity [mAh g <sup>-1</sup> ] (current density [A g <sup>-1</sup> ])	Capacity retention (cycles numbers)	Voltage range [V]	Ref.
VO <sub>2</sub>	1 m ZnSO <sub>4</sub>	325.6 (0.05)	86% (5000)	0.2–1.2	[145]
VO <sub>2</sub>	1 m ZnSO <sub>4</sub>	353 (1)	75.5% (945)	0.2–1.3	[216]
Nsutite-type VO <sub>2</sub>	3 m Zn(CF <sub>3</sub> SO <sub>3</sub> ) <sub>2</sub>	314.4 (1)	84% (5000)	0.2–1.4	[217]
VO <sub>2</sub> (A)	3 m Zn(CF <sub>3</sub> SO <sub>3</sub> ) <sub>2</sub>	400 (0.1)	29.3% (600)	0.2–1.4	[218]
VO <sub>2</sub> (A)@PPy	3 m Zn(CF <sub>3</sub> SO <sub>3</sub> ) <sub>2</sub>	440 (0.1)	47.7% (860)	0.2–1.4	[218]
VO <sub>2</sub> (B)	3 m Zn(CF <sub>3</sub> SO <sub>3</sub> ) <sub>2</sub>	357 (0.25 C)	91.2% (300)	0.3–1.5	[60]
VO <sub>2</sub> (B)/rGO	3 m Zn(CF <sub>3</sub> SO <sub>3</sub> ) <sub>2</sub>	456 (0.1)	90% (1000)	0.2–1.4	[219]
VO <sub>2</sub> (D)	3 m ZnSO <sub>4</sub>	442 (0.1)	30.5% (30 000)	0.2–1.5	[150]
O <sub>d</sub> -HVO@PPy	2 m ZnSO <sub>4</sub>	337 (0.2)	77.2% (1000)	0.2–1.6	[220]
p-V <sub>2</sub> O <sub>3</sub> @C	3 m Zn(CF <sub>3</sub> SO <sub>3</sub> ) <sub>2</sub>	350 (0.1)	90% (4000)	0.3–1.5	[156]
V <sub>2</sub> O <sub>3</sub>	2 m Zn(CF <sub>3</sub> SO <sub>3</sub> ) <sub>2</sub>	625 (0.1)	100% (10 000)	0.2–1.6	[157]
N@C/V <sub>2</sub> O <sub>3</sub>	3 m ZnSO <sub>4</sub>	451 (0.1)	92.95% (152)	0.3–1.6	[221]
V <sub>2</sub> O <sub>5</sub>	1 m Zn(ClO <sub>4</sub> ) <sub>2</sub>	335 (0.05)	85% (5000)	0.4–1.6	[164]
V <sub>2</sub> O <sub>5</sub>	3 m Zn(CF <sub>3</sub> SO <sub>3</sub> ) <sub>2</sub>	460 (0.5)	91.1% (4000)	0.2–1.6	[165]
V <sub>2</sub> O <sub>5</sub>	3 m ZnSO <sub>4</sub>	224 (0.1)	100% (400)	0.4–1.4	[166]
V <sub>2</sub> O <sub>5</sub>	2 m ZnSO <sub>4</sub>	341 (1)	84.3% (500)	0.2–1.6	[167]
V <sub>2</sub> O <sub>5</sub>	3 m Zn(CF <sub>3</sub> SO <sub>3</sub> ) <sub>2</sub>	319 (0.02)	81% (500)	0.5–1.5	[168]
V <sub>2</sub> O <sub>5</sub>	21 m LiTFSI + 1 m Zn(CF <sub>3</sub> SO <sub>3</sub> ) <sub>2</sub>	238 (0.05)	80% (2000)	0.2–1.6	[222]
O <sub>d</sub> -V <sub>2</sub> O <sub>5</sub>	3 m Zn(CF <sub>3</sub> SO <sub>3</sub> ) <sub>2</sub>	406 (0.1)	90% (1000)	0.1–1.6	[223]
O <sub>d</sub> -V <sub>2</sub> O <sub>5</sub>	2 m Zn(CF <sub>3</sub> SO <sub>3</sub> ) <sub>2</sub>	397.5 (0.2)	94.7% (5000)	0.4–1.5	[224]
V <sub>2</sub> O <sub>5</sub> @C	2.5 m Zn(CF <sub>3</sub> SO <sub>3</sub> ) <sub>2</sub>	361.9 (0.5)	71% (2000)	0.2–1.5	[225]
V <sub>2</sub> O <sub>5</sub> /GO	3 m Zn(CF <sub>3</sub> SO <sub>3</sub> ) <sub>2</sub>	525 (0.1)	90.8% (10 000)	0.3–1.6	[226]
PC/V <sub>2</sub> O <sub>5</sub> nH <sub>2</sub> O	3 m Zn(CF <sub>3</sub> SO <sub>3</sub> ) <sub>2</sub>	409.5 (0.5)	97.1% (1000)	0.3–1.6	[227]
V <sub>3</sub> O <sub>7</sub> H <sub>2</sub> O	1 m ZnSO <sub>4</sub>	375 (1 C)	80% (200)	0.4–1.1	[201]
nanogrid- V <sub>3</sub> O <sub>7</sub> H <sub>2</sub> O	3 m Zn(CF <sub>3</sub> SO <sub>3</sub> ) <sub>2</sub>	481.3 (0.1)	85.4% (1000)	0.05–1.7	[228]
h-VOW	2 m ZnSO <sub>4</sub>	455 (0.1)	85% (1200)	0.4–1.6	[229]
V <sub>3</sub> O <sub>7</sub> H <sub>2</sub> O/Mxene	3 m Zn(CF <sub>3</sub> SO <sub>3</sub> ) <sub>2</sub>	365.3 (0.2)	84% (5600)	0.2–1.6	[230]
V <sub>5</sub> O <sub>12</sub> 6H <sub>2</sub> O	3 m Zn(CF <sub>3</sub> SO <sub>3</sub> ) <sub>2</sub>	388 (0.2)	94% (1000)	0.2–1.6	[203]
V <sub>5</sub> O <sub>12</sub> 6H <sub>2</sub> O-LGO	3 m Zn(ClO <sub>4</sub> ) <sub>2</sub>	467 (0.1)	96.6% (3500)	0.2–1.6	[231]
Z-V <sub>5</sub> O <sub>12</sub> 6H <sub>2</sub> O	2 m ZnSO <sub>4</sub>	328 (0.05)	80.4% (1500)	0.2–1.6	[232]
V <sub>6</sub> O <sub>13</sub>	1 m Zn(CF <sub>3</sub> SO <sub>3</sub> ) <sub>2</sub>	≈360 (0.2)	92% (2000)	0.2–1.5	[179]
V <sub>6</sub> O <sub>13</sub>	3 m Zn(CF <sub>3</sub> SO <sub>3</sub> ) <sub>2</sub>	450 (0.1)	80% (3000)	0.3–1.4	[180]
V <sub>6</sub> O <sub>13</sub> /CC	3 m ZnSO <sub>4</sub>	520 (0.5)	85.3% (1000)	0.2–1.4	[233]
V <sub>6</sub> O <sub>13</sub> @GCC	3 m ZnSO <sub>4</sub>	290 (0.375)	99% (1000)	0.2–1.4	[70]
O <sub>d</sub> -V <sub>6</sub> O <sub>13</sub> @C	3 m Zn(TFSI) <sub>2</sub>	401 (0.2)	86% (2000)	0.2–1.5	[234]
DNGS	ZnSO <sub>4</sub> + Na <sub>2</sub> SO <sub>4</sub> + H <sub>3</sub> BO <sub>3</sub> mixed solution	403.5 (0.2)	94% (2000)	0.2–1.5	[235]
VCF	3 m Zn(CF <sub>3</sub> SO <sub>3</sub> ) <sub>2</sub>	371 (0.2)	91% (5000)	0.3–1.5	[236]
CO <sub>2</sub> -V <sub>6</sub> O <sub>13</sub>	3 m Zn(CF <sub>3</sub> SO <sub>3</sub> ) <sub>2</sub>	471 (0.1)	80% (4000)	0.3–1.5	[237]
V <sub>6</sub> O <sub>13</sub> nH <sub>2</sub> O	3 m Zn(CF <sub>3</sub> SO <sub>3</sub> ) <sub>2</sub>	386 (0.3)	87% (1000)	0.2–1.4	[205]
V <sub>10</sub> O <sub>24</sub> 12H <sub>2</sub> O	2 m ZnSO <sub>4</sub>	327 (0.1)	57.5% (3000)	0.5–1.5	[238]
dendritic V <sub>10</sub> O <sub>24</sub> 12H <sub>2</sub> O	3 m Zn(CF <sub>3</sub> SO <sub>3</sub> ) <sub>2</sub>	164.5 (0.2)	80.1% (3000)	0.7–1.7	[206]
Al-doped V <sub>10</sub> O <sub>24</sub> 12H <sub>2</sub> O	3 m Zn(CF <sub>3</sub> SO <sub>3</sub> ) <sub>2</sub>	415 (0.2)	98% (3000)	0.3–1.6	[208]
V <sub>10</sub> O <sub>24</sub> 12H <sub>2</sub> O@C	3 m Zn(CF <sub>3</sub> SO <sub>3</sub> ) <sub>2</sub>	290.5 (0.5)	94.1% (10 000)	0.3–1.5	[209]

structure-like tunnel, which is conducive to the intercalation of cation.<sup>[154,155]</sup> Vanadium 3d electrons can transfer along the V-V chain and generally exhibit higher electronic conductivity than most transition metal oxides, which is conducive to the development of V<sub>2</sub>O<sub>3</sub> as AZIBs cathode with excellent electrochemical performance.<sup>[64]</sup> Ding et al.<sup>[156]</sup> prepared a porous V<sub>2</sub>O<sub>3</sub>@C

hybrid nanostructure (P-V<sub>2</sub>O<sub>3</sub>@C) with high conductivity by pyrolyzing V-MOF precursor and further illustrated its application as a intercalated cathode for AZIBs. The corresponding peak potential separation ( $\Delta V$ ) to P-V<sub>2</sub>O<sub>3</sub>@C at 0.2 mV s<sup>-1</sup> is significantly smaller than V<sub>2</sub>O<sub>3</sub>@C, indicating that the P-V<sub>2</sub>O<sub>3</sub>@C cathode is more stable than V<sub>2</sub>O<sub>3</sub>@C cathode (**Figure 5a**). The



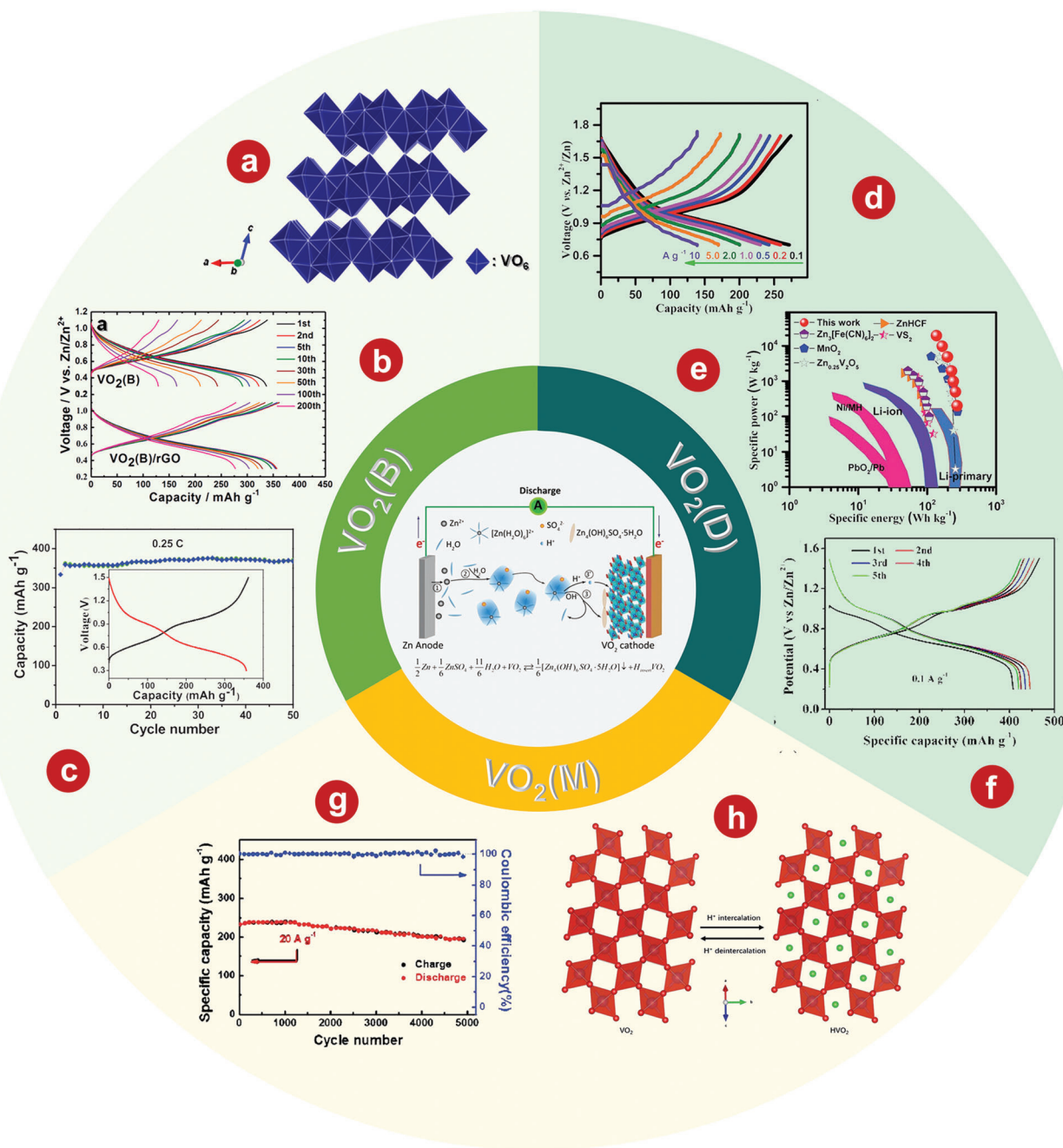
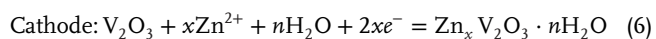


**Figure 4.** a) The crystal structure of VO<sub>2</sub>(B). b) Continuous cycles of bare VO<sub>2</sub> and the VO<sub>2</sub>/rGO composite. c) Discharge–charge profiles obtained at different current densities from 0.1 to 10 A g<sup>-1</sup>. e) Comparison of the Ragone plots of the VO<sub>2</sub>-based ZIB and reported energy storage systems. f) The first five galvanostatic charging/discharging curves at 0.1 A g<sup>-1</sup>. g) Corresponding discharge/charge profiles at various current densities. h) Schematic illustration of the proton insertion and deinsertion into VO<sub>2</sub>(M). a, b) Reproduced with permission.<sup>[144]</sup> Copyright 2018, American Chemical Society. c) Reproduced with permission.<sup>[60]</sup> Copyright 2018, WILEY-VCH. d, e) Reproduced with permission.<sup>[147]</sup> Copyright 2018, The Royal Society of Chemistry. f) Reproduced with permission.<sup>[150]</sup> Copyright 2019, The Royal Society of Chemistry. g, h) Reproduced with permission.<sup>[153]</sup> Copyright 2020, The Royal Society of Chemistry.

electrochemical reactions in new Zn// V<sub>2</sub>O<sub>3</sub> battery system are shown in Figure 5b and described by the following equation:



The intercalation behavior of Zn<sup>2+</sup> in V<sub>2</sub>O<sub>3</sub> is verified by first-principles calculations (Figure 5c). As the charge around the zinc ion increases, so does the number of electrons between the zinc atom and the oxygen atom.

The storage of Zn ions by V<sub>2</sub>O<sub>3</sub> is achieved through the complete phase transformation with the product of V<sub>2</sub>O<sub>5</sub>.<sup>[157,158]</sup>



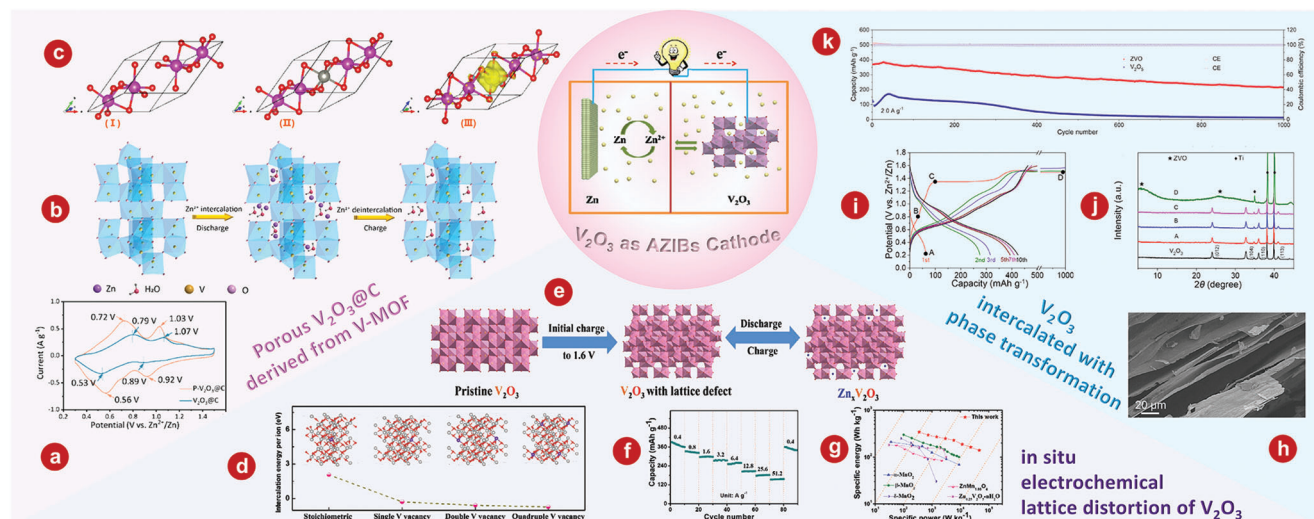


**Figure 5.** a) Peak potential separations in the CV curves of P- $V_2O_5$ @C and  $V_2O_5$ @C. b) Schematic illustrations of  $Zn^{2+}$  storage mechanism of  $V_2O_5$  cathode during the processes of discharge and charge. c) Structure of  $V_2O_5$  without (I) and with (II) Zn ions being inserted. (III) Differential charge state density between  $V_2O_5$  with and without Zn ions being inserted. Red balls denote O atoms, purple balls denote V atoms, and gray balls denote Zn ions. d) DFT calculated intercalation energies for zinc ions in stoichiometric  $V_2O_5$  and  $V_2O_5$  with different vacancies. The inset images show the corresponding models of  $V_{48}O_{72}$  (defect-free),  $V_{47}\square O_{72}$  (one-vacancy),  $V_{46}\square_2 O_{72}$  (two-vacancy), and  $V_{44}\square_4 O_{72}$  (quadruple-vacancy). e) Schematic illustration of the initial charging process for  $V_2O_5$  and the subsequent  $Zn^{2+}$  storage in  $V_2O_5$  with lattice defects. f) Rate performance of  $V_2O_5$  at various rates from 0.4 to 51.2  $A\ g^{-1}$ . g) Ragone plots of  $V_2O_5$  compared with reported cathodes. h) The scanning electron microscopy (SEM) image of  $V_2O_5$  nanosheets. i) The typical charge/discharge profiles of  $V_2O_5$ . j) The XRD patterns of  $V_2O_5$  electrode during the initial cycle. k) The cyclability performance of  $Zn_xV_2O_5 \cdot nH_2O$  electrode at 2.0  $A\ g^{-1}$ . a–c) Reproduced with permission.<sup>[156]</sup> Copyright 2019, American Chemical Society. e–g) Reproduced with permission.<sup>[159]</sup> Copyright 2021, Wiley-VCH. h–k) Reproduced with permission.<sup>[161]</sup> Copyright 2021, Elsevier.

However, the exact electrochemical behavior of  $V_2O_5$  in a weak acid solution containing  $Zn^{2+}$  is not clear. Ding and colleagues<sup>[159]</sup> studied a novel in situ electrochemical conversion reaction of  $V_2O_5$ , and the resulting product can be used as a cathode for ultra-fast  $Zn^{2+}$  (de)intercalation. Operando XRD and Operando Raman spectroscopy confirmed the unique lattice conversion reaction of  $V_2O_5$  during initial charging. As shown in Figure 5d, the corresponding single-vacancy, double-vacancy, and four-vacancy systems consist of  $V_{47}\square O_{72}$ ,  $V_{46}\square_2 O_{72}$ , and  $V_{44}\square_4 O_{72}$ , where  $\square$  represents cationic vacancies. The density functional theory (DFT) calculations show that the intercalation energy of  $Zn^{2+}$  decreases from  $-0.28$  to  $-0.72$  eV when the number of empty spaces increases from 1 to 4, which is lower than stoichiometry  $V_2O_5$  (2.06 eV). This indicates that vanadium vacancies in  $V_2O_5$  facilitate the intercalation of multivalent  $Zn^{2+}$ . As shown in Figure 5e, the reversible process directly indicates that  $V_2O_5$  has superior ability of (de)insertion. The unique in situ electrochemical lattice conversion reaction allows the  $V_2O_5$  cathode to achieve a high reversible capacity of 328  $mAh\ g^{-1}$  at 0.8  $A\ g^{-1}$  (Figure 5f), which is higher than some reported cathodes (Figure 5g).<sup>[146,159,160]</sup> In addition, Hu et al.<sup>[161]</sup> prepared a metallic  $V_2O_5$  material with intercalated phase transition as cathode for application in AZIBs. The prepared  $V_2O_5$  is composed of 2D nanosheets with large sizes (Figure 5h). The significant change in the cyclic voltammetry (CV) curve during the cycle indicates the phase transition during the cycle (Figure 5i). In order to explore the phase evolution mechanism of  $V_2O_5$ , ex situ XRD tests are performed at selected states and different cycling stages (Figure 5j). After 1000 cycles, the  $Zn_xV_2O_5 \cdot nH_2O$  electrode still has a high reversible

specific capacity of 218  $mAh\ g^{-1}$  and the coulombic efficiency (CE) is close to 100% (Figure 5k).

### 3.3. $V_2O_5$

$V_2O_5$  is a typical layered vanadium compound, in which V and O atoms form  $[VO_5]$  square pyramid, and then through co-edges or co-corners form a layered structure.<sup>[162]</sup> The adjacent layers are also connected by van der Waals force and H bonds between the layers.<sup>[163]</sup> In addition, the layer spacing is about 0.58 nm, much larger than the radius of  $Zn^{2+}$  (0.76 Å), which is conducive to the diffusion of  $Zn^{2+}$  between  $V_2O_5$  layers.<sup>[164]</sup>  $V_2O_5$  occurs two-electron redox reaction and can provide a high theoretical zinc storage capacity of 589  $mAh\ g^{-1}$  in the process of (dis)charge.<sup>[165]</sup> However, the large polarization and volume variation caused by the insertion of  $Zn^{2+}$  as a multivalent carrier into the cathode host remains a major obstacle to the development of AZIBs with high performance.<sup>[148]</sup> In addition,  $V_2O_5$  has the disadvantage of low electrical conductivity, which hinders its large-scale development.<sup>[166]</sup> Therefore, it is necessary to find ways to enhance electronic conductivity. So far, researchers have reported a variety of  $V_2O_5$  materials.<sup>[167–170]</sup> Recently, many researchers have enhanced the electronic conductivity of  $V_2O_5$  by combining it with carbonaceous functional materials (e.g., carbon nanotubes, carbon nanofibers, and carbon quantum dots (CQDs)).<sup>[171,172]</sup> Zhang et al.<sup>[173]</sup> synthesized  $V_2O_5$  nanobelts induced by CQDs by a simple one-step hydrothermal method.  $V_2O_5$ /CQDs composite as the cathode of ZIBs shows good stable cycle performance

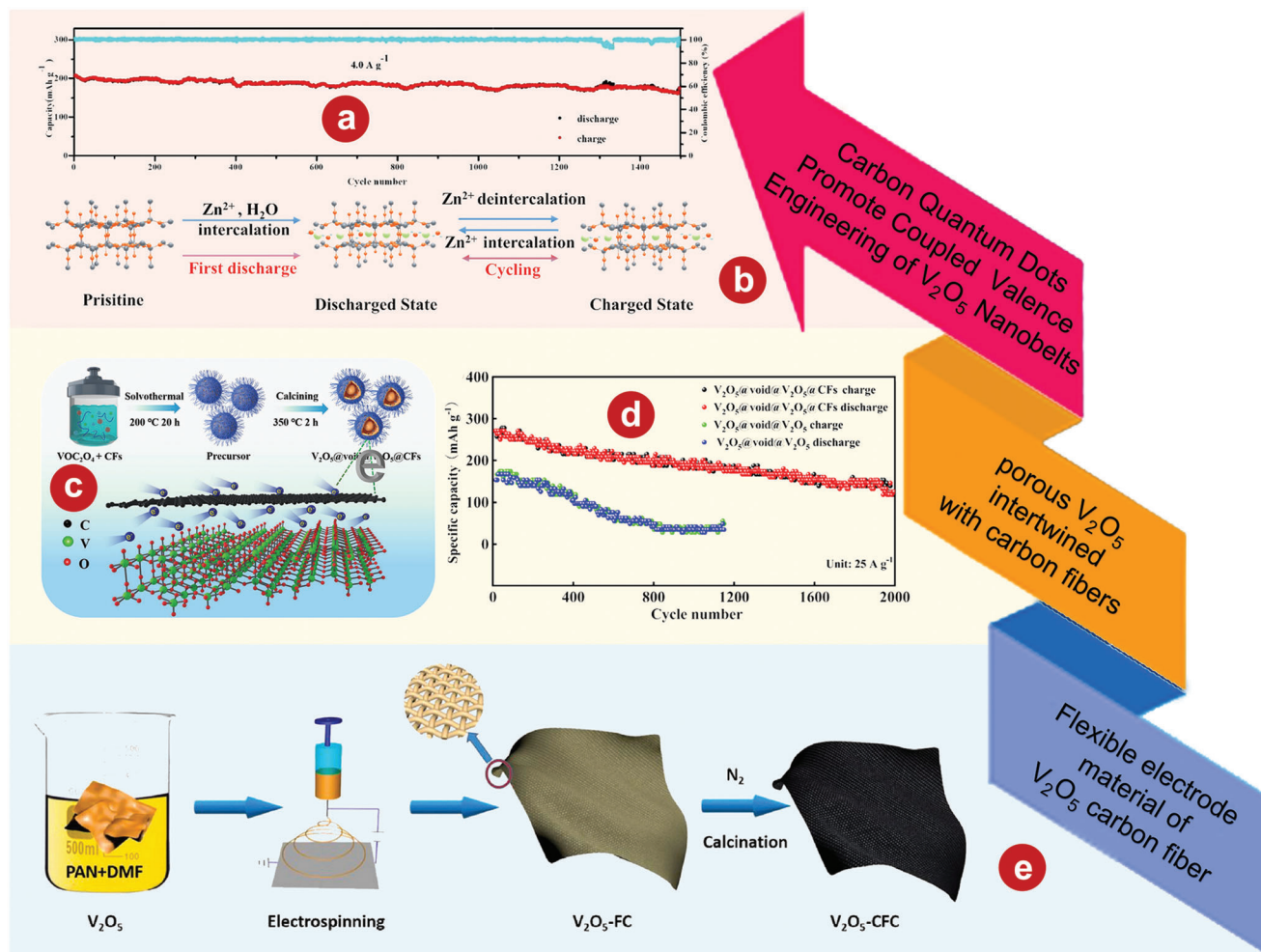
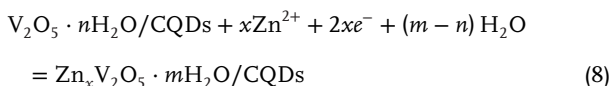


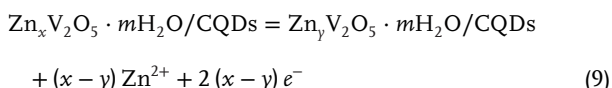
**Figure 6.** a) Cycling performance and CE of V<sub>2</sub>O<sub>5</sub>/CQDs at the current density of 4 A g<sup>-1</sup>. b) Schematic illustration of Zn<sup>2+</sup> and water co-intercalation into V<sub>2</sub>O<sub>5</sub>/CQDs electrode during the initial discharge process and reversible Zn<sup>2+</sup>. c) Illustration of synthetic procedure of V<sub>2</sub>O<sub>5</sub>@void@V<sub>2</sub>O<sub>5</sub>@CFs hybrid. d) Cycling performance comparison of V<sub>2</sub>O<sub>5</sub>@void@V<sub>2</sub>O<sub>5</sub> and V<sub>2</sub>O<sub>5</sub>@void@V<sub>2</sub>O<sub>5</sub>@CFs electrode at 25 A g<sup>-1</sup>. e) Mechanism for the development of flexible V<sub>2</sub>O<sub>5</sub>-CFC cathode material. a, b) Reproduced with permission.<sup>[173]</sup> Copyright 2021, Wiley-VCH. c, d) Reproduced with permission.<sup>[174]</sup> Copyright 2022, Elsevier. e) Reproduced with permission.<sup>[175]</sup> Copyright 2022, Elsevier.

which maintains 85% capacity at 4 A g<sup>-1</sup> over 1500 cycles. (Figure 6a). Zhang et al.<sup>[173]</sup> also studied its electrochemical kinetics and zinc ion storage mechanism (Figure 6b). The chemical reactions of cathode are as follows:

In first discharge process:



In subsequent cycles:



In order to give full play to the electrochemical properties of V<sub>2</sub>O<sub>5</sub>, Xiong et al.<sup>[174]</sup> first used a simple combination of

hydrothermal and calcination method to construct in situ a sphere-ball porous V<sub>2</sub>O<sub>5</sub> (V<sub>2</sub>O<sub>5</sub>@-void@V<sub>2</sub>O<sub>5</sub>@CFs) by wrapping carbon fibers (CFs) (Figure 6c). V<sub>2</sub>O<sub>5</sub>@-void@V<sub>2</sub>O<sub>5</sub>@CFs electrode to realize the high capacity of 149 mAh g<sup>-1</sup> at 25 A g<sup>-1</sup> after 2000 cycles (Figure 6d). The excellent energy storage performance of V<sub>2</sub>O<sub>5</sub>@-void@V<sub>2</sub>O<sub>5</sub>@CFs electrode is attributed to its unique architecture. The CFs in the composite act as strong shells and conductive bridges connecting the independent V<sub>2</sub>O<sub>5</sub> units, preventing the isolation of adjacent spheres, and providing fast interconnect paths for electrons and ions in electrochemical dynamics. In addition, Xu et al.<sup>[175]</sup> developed a novel vanadium-based AZIB by combining V<sub>2</sub>O<sub>5</sub> with carbon fiber cloth (V<sub>2</sub>O<sub>5</sub>-CFC) by electrospinning (Figure 6e), which had excellent flexibility and was designed with no binder and no collection device. The composite fiber structure can avoid the coacervation of V<sub>2</sub>O<sub>5</sub> nanosheets and reduce the volume effect in the (dis)charging process, which makes V<sub>2</sub>O<sub>5</sub>-CFC deliver excellent electrochemical properties.

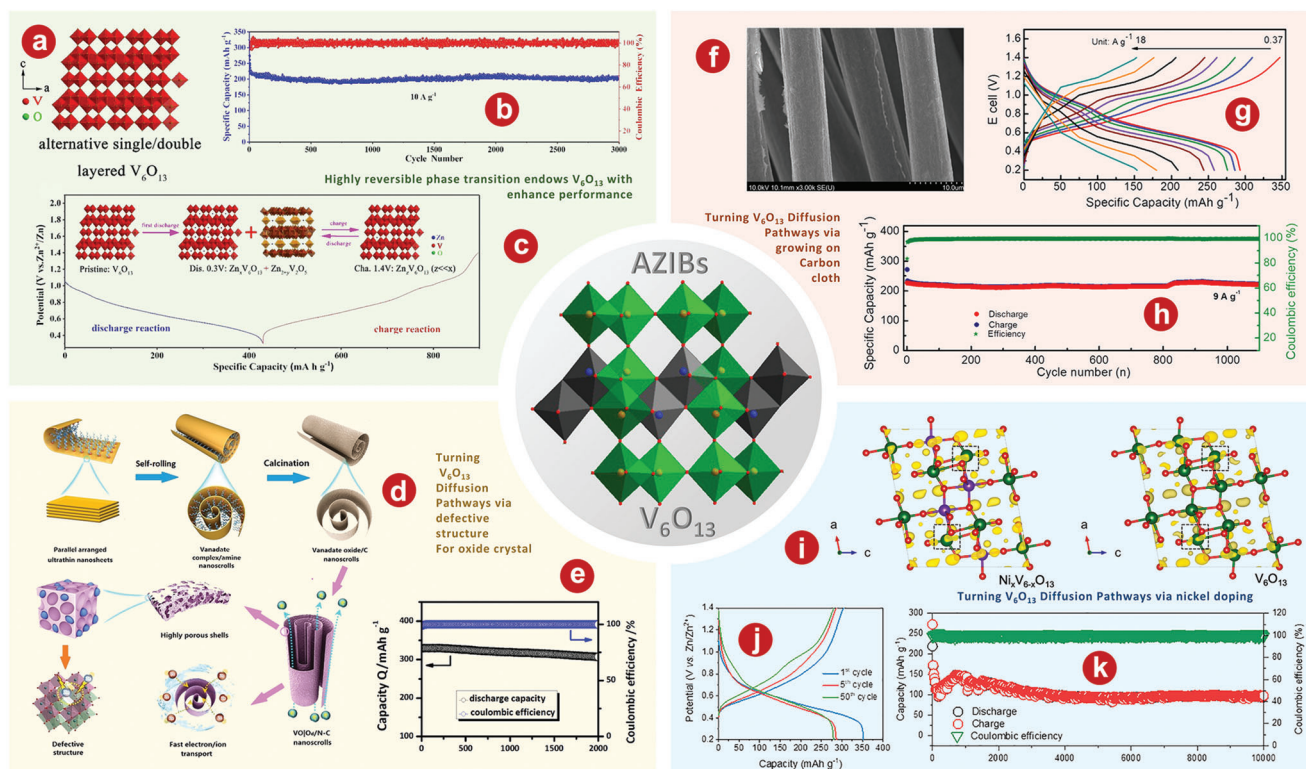


**Figure 7.** a) The crystal structures of  $V_6O_{13}$ . b) The cyclic performance at  $10\text{ A g}^{-1}$  of  $V_6O_{13}$  product. c) Schematic illustration of highly reversible phase transition during discharge-charge process of  $V_6O_{13}$ . d) Schematic illustration of the synthesis and structure of the  $(V_6O_{13-\delta})/C$  nanoscrolls. e) High-rate long-term cycling properties of the  $(V_6O_{13-\delta})/C$  sample at  $10\text{ A g}^{-1}$ . f) SEM image of  $V_6O_{13}@gCC$ . g) Discharge/charge profile of  $V_6O_{13}@gCC$  cathode at different current rates. h) Cycling performance at a current density of  $9\text{ A g}^{-1}$ . i) The differential charge density maps for  $Ni_xV_{6-x}O_{13}$  atomic layer slab and  $V_6O_{13}$  atomic layer slab with the iso-surface level of  $0.03\text{ e \AA}^{-3}$ . In the differential density map, yellow region indicates electro accumulation. Red O, green V, and pink Ni atoms. j) Charge/discharge profiles of  $Zn/Ni_{0.24}V_{5.76}O_{13}$  batteries at  $1.0\text{ A g}^{-1}$ . k) Cycling performance of  $Zn/Ni_{0.24}V_{5.76}O_{13}$  batteries at  $8.0\text{ A g}^{-1}$ . a–c) Reproduced with permission.<sup>[180]</sup> Copyright 2019, Wiley-VCH. d, e) Reproduced with permission.<sup>[181]</sup> Copyright 2020, Wiley-VCH. f–h) Reproduced with permission.<sup>[70]</sup> Copyright 2020, Elsevier. i–k) Reproduced with permission.<sup>[183]</sup> Copyright 2022, Elsevier.

### 3.4. $V_6O_{13}$

With perovskite-like framework structure, monoclinic  $V_6O_{13}$  is composed of twisted  $VO_6$  octahedrons arranged in a zigzag shape with a corporate edge or a corporate angle to form single and double layers.<sup>[176,177]</sup> The V(1) sites of the monolayer and the V(3) sites of the bilayer are occupied by  $V^{4+}$ , and the V(2) sites of the bilayer have the  $V^{5+}$  characteristic.<sup>[141,178]</sup>  $V_6O_{13}$  material with a theoretical capacity of  $417\text{ mAh g}^{-1}$  at  $900\text{ Wh kg}^{-1}$  has been studied as cathode of LIBs due to its high conductivity at room temperature.<sup>[177]</sup> In addition,  $V_6O_{13}$  has significant potential as a high-performance cathode material of AZIBs due to its special 3D open framework structure that can be used for  $Zn^{2+}$  (de)intercalation.<sup>[179]</sup> Shan et al.<sup>[180]</sup> proved that  $V_6O_{13}$  had better  $Zn^{2+}$  storage performance as a cathode for AZIBs by comparing it with  $VO_2$  and  $V_2O_5$ . The crystal structures of  $V_6O_{13}$  (Figure 7a) provide additional active sites for  $Zn^{2+}$  storage. Figure 7b delivers that  $V_6O_{13}$  can show excellent long-term cycling of  $206\text{ mA h}^{-1}$  after 3000 cycles at  $10\text{ A g}^{-1}$ . The schematic diagram of the energy storage mechanism of  $Zn/V_6O_{13}$  aqueous battery is shown in Figure 7c.

Recently, researchers also modified the properties of  $V_6O_{13}$  through various schemes. Lin and colleagues<sup>[181]</sup> prepared defec-

tive vanadate oxide ( $V_6O_{13-\delta}$ )/C (DVOC) nanoscrolls used as cathode materials for AZIBs due to their large spacing (Figure 7d). DVOC has good long-term cycle stability and stable charge and discharge performance. After 2000 cycles, at a current density of  $10\text{ A g}^{-1}$ , the CE of the DVOC is close to 100%, and 93.4% of the initial capacity is retained (Figure 7e). In addition, Tamilselvan et al.<sup>[70]</sup> coaxially grew interconnected  $V_6O_{13}$  nanobelts on carbon cloth fibers ( $V_6O_{13}@gCC$ ) through a facile hydrothermal process. SEM image of  $V_6O_{13}@gCC$  is shown in Figure 7f. As shown in Figure 7g, the current density of  $V_6O_{13}@gCC$  electrode increased from  $0.375$  to  $18\text{ A g}^{-1}$ , following the discharge capacity decrease from  $290\text{ mAh g}^{-1}$  to  $154\text{ mAh g}^{-1}$ . The  $V_6O_{13}@gCC$  electrode obtained an initial specific capacity of  $227\text{ mAh g}^{-1}$  at  $9\text{ A g}^{-1}$  and retained nearly 99% after 1000 cycles (Figure 7h).

Metallic ion doping is also proven to be effective to enhance the electrochemical performance of  $V_6O_{13}$ .<sup>[182]</sup> Our group<sup>[183]</sup> synthesized nickel-ion doped  $V_6O_{13}$  ( $Ni_xV_{6-x}O_{13}$ ) layers with abundant reaction sites, high spacing, and high conductivity, and also verified their feasibility as cathode for AZIBs. Figure 7i shows that carriers can be more efficiently transferred to the minimum conduction band of  $Ni_xV_{6-x}O_{13}$  layers compared with  $V_6O_{13}$ , which is conducive to the transport of  $Zn^{2+}$ .<sup>[184,185]</sup>  $Ni_{0.24}V_{5.76}O_{13}$  electrode shows the best electrochemical performance with the



discharge capacitance of 302.6 mAh g<sup>-1</sup> at 1 A g<sup>-1</sup> (Figure 7j). In addition, the Ni<sub>0.24</sub>V<sub>5.76</sub>O<sub>13</sub> cathode can reach a capacity of 96.5 mA h g<sup>-1</sup> with a CE of 99.01% after 10 000 cycles at 8.0 A g<sup>-1</sup> (Figure 7k).

### 3.5. The Intercalation of H<sub>2</sub>O

Vanadium oxides are one of the most promising cathodes for AZIBs due to their diversity in composition and crystal structure. However, they still have some problems, for instance, the slow electrochemical diffusion kinetics and limited reversibility seriously hinder their wide applications. Structural H<sub>2</sub>O molecules which are in the layers of vanadium oxides have been studied because hydrated vanadium oxides can reversibly absorb more guest ions than dehydrated vanadium oxides, due to the presence of structural H<sub>2</sub>O molecules between the layers, thus expanding the ion intercalation space.<sup>[186]</sup> Furthermore, the structural H<sub>2</sub>O molecules provide charge shielding to reduce electrostatic electric interactions between intercalated Zn<sup>2+</sup> and the host materials, thereby allowing rapid Zn<sup>2+</sup> diffusion.<sup>[187]</sup>

#### 3.5.1. V<sub>2</sub>O<sub>5</sub> nH<sub>2</sub>O

Different from the above V<sub>2</sub>O<sub>5</sub> with a typical layered structure, V<sub>2</sub>O<sub>5</sub> nH<sub>2</sub>O is composed of two [VO<sub>6</sub>] octahedral layers, showing a special double-layer structure. The water molecules are usually in the middle of the two layers and act as props, providing greater spacing between the inner layers.<sup>[61,188]</sup> In addition, the intercalation of water molecules can also reduce the effective charge of Zn<sup>2+</sup>, which makes the process of Zn<sup>2+</sup> deintercalation easier to carry out, thus showing better electrochemical performance.<sup>[189,190]</sup> Huang et al.<sup>[191]</sup> prepared a freestanding V<sub>2</sub>O<sub>5</sub> nH<sub>2</sub>O/CNTs film and applied it as AZIBs cathode in aqueous/organic hybrid electrolytes. In the hybrid electrolytes, the AZIB based on this cathode has excellent performance with an energy density of 102 Wh kg<sup>-1</sup> at high power of 1500 W kg<sup>-1</sup>. Yang et al.<sup>[192]</sup> oxidized interlayer-expanded VS<sub>2</sub> NH<sub>3</sub> hollow spheres to prepare V<sub>2</sub>O<sub>5</sub> nH<sub>2</sub>O with decreased nanometer size and ordered porous structure through in situ electrochemical oxidation strategies, which provides abundantly accessible sites and promotes the Zn<sup>2+</sup> diffusion process (Figure 8a). This V<sub>2</sub>O<sub>5</sub> nH<sub>2</sub>O cathode derived from VS<sub>2</sub> NH<sub>3</sub> shows an excellent long cyclic stability of 110% capacity retention after 2000 cycles at 3 A g<sup>-1</sup> (Figure 8b).

#### 3.5.2. The Intercalation of Organic Molecules in V<sub>2</sub>O<sub>5</sub> nH<sub>2</sub>O

It's found that the intercalation of conductive organic polymer (e.g., polyaniline, polypyrrole) into V<sub>2</sub>O<sub>5</sub> nH<sub>2</sub>O can enlarge the mesoporous, and improve the electrical conductivity of the nanocomposites, thus enhancing the performance of AZIBs.<sup>[193]</sup> Zeng et al.<sup>[194]</sup> employed a conjugated polymer and water co-intercalation strategy to greatly improve the kinetics of Zn<sup>2+</sup> diffusion in rose-like V<sub>2</sub>O<sub>5</sub> architectures (PVO) (Figure 8c). The cathode based on PVO shows a further enhanced rate perfor-

mance of 288.9 mA h g<sup>-1</sup> at 20 A g<sup>-1</sup> (Figure 8d). Figure 8e shows the reversible storage and formation mechanism of Zn<sup>2+</sup> in PVO cathode. Wang et al.<sup>[195]</sup> enhanced electrochemical dynamics and stability of V<sub>2</sub>O<sub>5</sub> nH<sub>2</sub>O, which was realized by pre-intercalation of aniline monomer and in situ polymerization in the oxide interlayers (PANI-VOH), as shown in Figure 8f. Compared to 255 mAh g<sup>-1</sup> in the first cycle, the reversible capacity of PANI-VOH increases to 323 mAh g<sup>-1</sup> after 6 cycles, possibly because of the improved wetting by electrolyte or material utilization (Figure 8g). The electrochemical mechanism of PANI-VOH was finally obtained by Zeng et al.<sup>[194]</sup> through analyzing the data shown in Figure 8h. In addition to PANI, the intercalation of PPy can greatly expand the layer spacing of the layered structure, effectively reduce the internal resistance of the main material, accelerate the ion transport speed, and improve the specific volume and structural properties of the V<sub>2</sub>O<sub>5</sub> nH<sub>2</sub>O. As shown in Figure 8i, Feng et al.<sup>[196]</sup> intercalated the conducting PPy into the V<sub>2</sub>O<sub>5</sub> nH<sub>2</sub>O layers to modulate the structure of the layered V<sub>2</sub>O<sub>5</sub> nH<sub>2</sub>O (PPy/VOH). PPy/VOH has a specific capacity of 383 mAh g<sup>-1</sup> at 0.1 A g<sup>-1</sup>, however, under the same conditions, the specific capacity of V<sub>2</sub>O<sub>5</sub> nH<sub>2</sub>O is only 168 mAh g<sup>-1</sup> (Figure 8j). The PPy/VOH cathode is assembled into AZIB, as shown in Figure 8k. On the basis of the experimental results of Feng et al.,<sup>[196]</sup> the electrochemical mechanism of Zn//PPy/VOH battery is shown in Figure 8l.

#### 3.5.3. V<sub>3</sub>O<sub>7</sub> H<sub>2</sub>O

For V<sub>3</sub>O<sub>7</sub>·H<sub>2</sub>O (H<sub>2</sub>V<sub>3</sub>O<sub>8</sub>) crystal structure, VO<sub>6</sub> octahedrons are connected to each other by corners and edges, and link with other VO<sub>5</sub> square pyramids to form 2D V<sub>3</sub>O<sub>8</sub> layers. The bc-plane·H<sub>2</sub>O molecules bonded with V atoms in VO<sub>5</sub> polyhedrons are on both sides of V<sub>3</sub>O<sub>8</sub> layers.<sup>[197,198]</sup> The two adjacent layers of V<sub>3</sub>O<sub>8</sub> are connected by H bonds. Due to the vibration of the H bonds, V<sub>3</sub>O<sub>8</sub> gets buffer layer space.<sup>[199]</sup> In the process of (de)intercalation of Zn<sup>2+</sup>, cell distortion is relatively easy to occur without damaging the crystal structure. There are particular H bonds in V<sub>3</sub>O<sub>7</sub> H<sub>2</sub>O that can accommodate the volume change during Zn<sup>2+</sup> (de)intercalation. Pang et al.<sup>[200]</sup> developed a composite of H<sub>2</sub>V<sub>3</sub>O<sub>8</sub> nanowires coated with graphene sheets (Figure 9a) as a cathode material for AZIBs. H<sub>2</sub>V<sub>3</sub>O<sub>8</sub> nanowires/graphene composite delivers a remarkable Zn<sup>2+</sup> storage performance with a high capacity of 394 mAh g<sup>-1</sup> at 0.1 A g<sup>-1</sup> (Figure 9b) and excellent retained capacity of 87% after 2000 cycles (Figure 9c) due to the synergistic effect between the structural characteristic of H<sub>2</sub>V<sub>3</sub>O<sub>8</sub> nanowires and the high conductivity of graphene networks. Pang et al.<sup>[200]</sup> also showed by DFT calculations that zinc is stable at the vacancy center and slightly distorts neighboring vanadium atoms (Figure 9d). Chen and colleagues<sup>[201]</sup> systematically investigated the Zn<sup>2+</sup> intercalation process in V<sub>3</sub>O<sub>7</sub> H<sub>2</sub>O and first discovered two-step Zn<sup>2+</sup> intercalation mechanism in V<sub>3</sub>O<sub>7</sub> H<sub>2</sub>O. The pathway for V<sub>3</sub>O<sub>7</sub> H<sub>2</sub>O synthesis is shown in Figure 9e. Figure 9f delivers two pairs of pseudo-platforms at 0.95/0.98 and 0.88/0.65 V, indicating that V<sub>3</sub>O<sub>7</sub> H<sub>2</sub>O will undergo a two-step process of Zn<sup>2+</sup> (de)intercalation during (dis)charge. Based on the two-step Zn<sup>2+</sup> intercalation mechanism, the structural evolution of a cathode material under different (dis)charge depths is



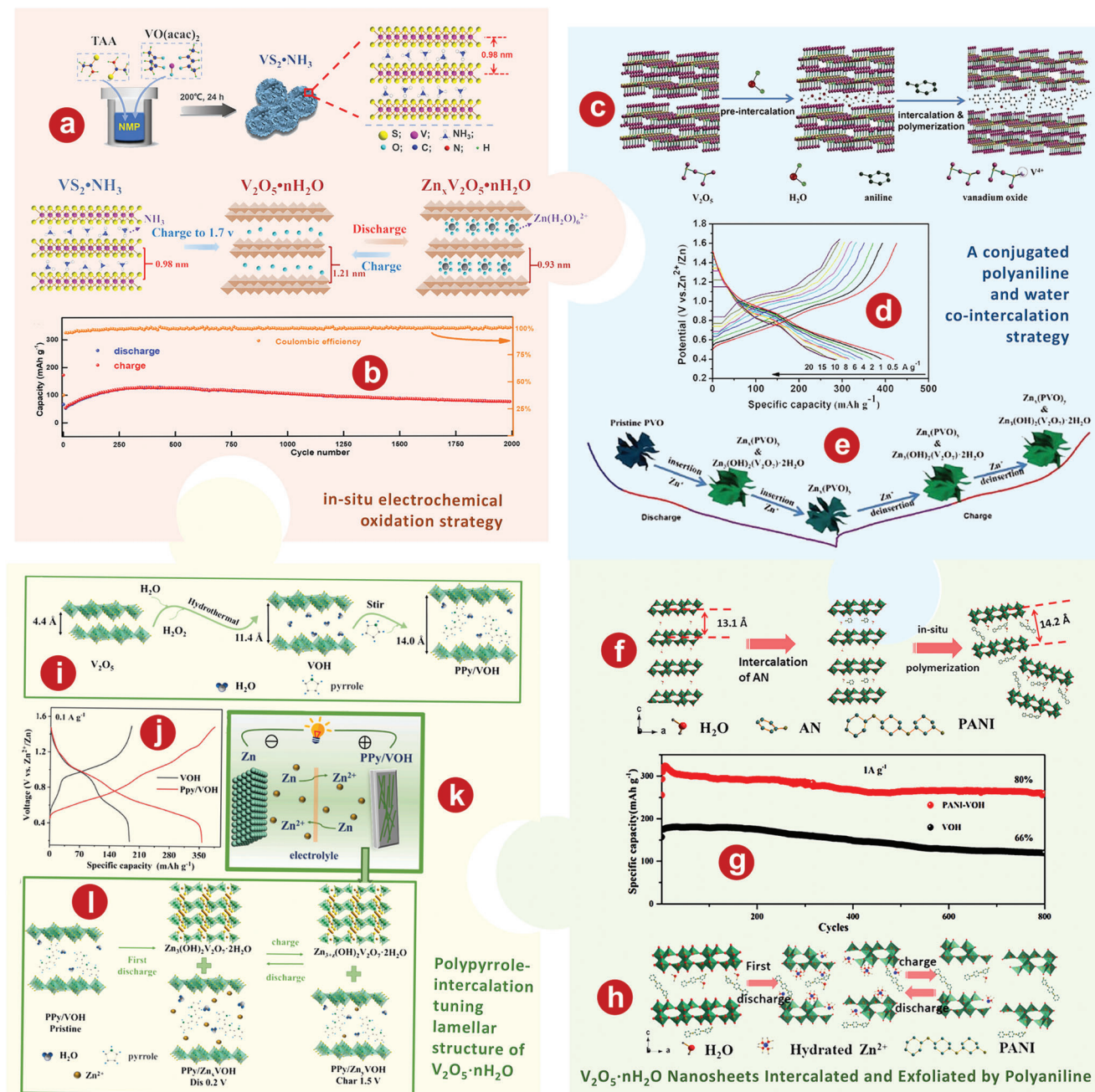


**Figure 8.** a) Schematic illustration of the synthesis of interlayer-expanded flower-like  $\text{VS}_2 \cdot \text{NH}_3$  hollow spheres, as well as the electrochemical oxidation of  $\text{VS}_2 \cdot \text{NH}_3$  process and the subsequent  $\text{Zn}^{2+}$  storage mechanism. b) Long-term stability at  $3.0 \text{ A g}^{-1}$ . c) Schematic diagram of the preparation processes of the PVO architectures. d) Discharge–charge curves at current densities ranging from  $0.5$  to  $20 \text{ A g}^{-1}$ . e) Schematic reversible storage mechanism of zinc species in the PVO cathode. f) Schematic illustration of the fabrication process for PANI–VOH. g) Cycling performance of PANI–VOH and  $\text{V}_2\text{O}_5 \cdot n\text{H}_2\text{O}$  at  $1 \text{ A g}^{-1}$ . h) Schematic illustration of the (dis)charging reaction mechanism. i) The diagram of synthesis of PPY/VOH composite. j) Specific capacity between  $\text{V}_2\text{O}_5 \cdot n\text{H}_2\text{O}$  and PPY/VOH at  $0.1 \text{ A g}^{-1}$ . k) The schematic configuring of metallic zinc//PPY/VOH AZIBs. l) Schematic diagram of the zinc (de)intercalation mechanism in the PPY/VOH cathode. a, b) Reproduced with permission.<sup>[192]</sup> Copyright 2022, Elsevier. c–e) Reproduced with permission.<sup>[194]</sup> Copyright 2019, The Royal Society of Chemistry. f–h) Reproduced with permission.<sup>[195]</sup> Copyright 2020, American Chemical Society. i–l) Reproduced with permission.<sup>[196]</sup> Copyright 2022, Elsevier.

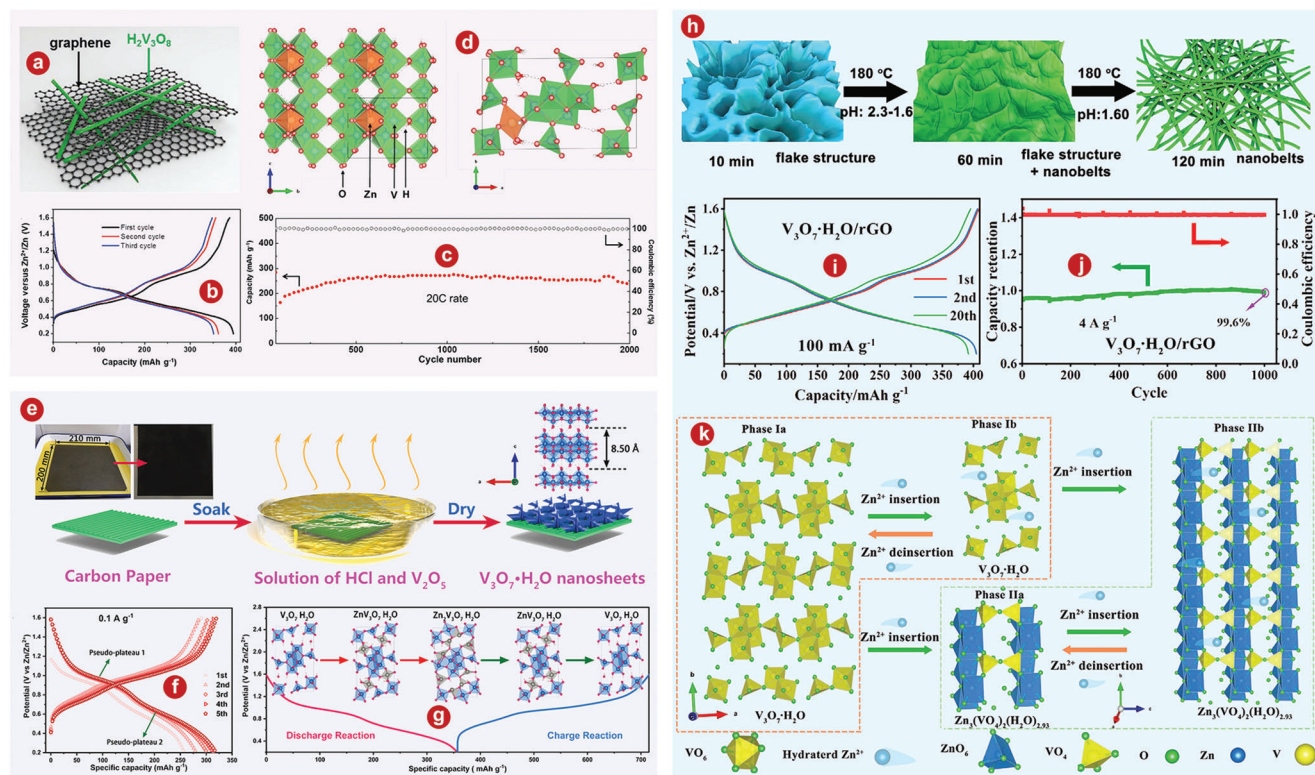
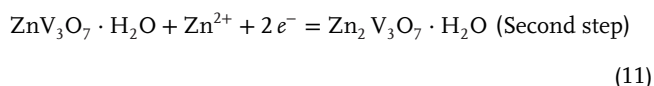
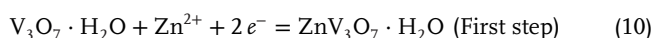


**Figure 9.** a) Schematic illustration of the structure of the  $\text{H}_2\text{V}_3\text{O}_8$  nanowires/graphene composite. b) Galvanostatic charge-discharge profiles of the  $\text{H}_2\text{V}_3\text{O}_8$ /graphene cathode at  $0.1 \text{ A g}^{-1}$ . c) Long cycling stability at  $20 \text{ C}$  rate ( $6 \text{ A g}^{-1}$ ). d) Potential intercalated Zn sites in the  $\text{H}_2\text{V}_3\text{O}_8$  crystal viewed along the  $[100]$  direction (left) and along the  $[001]$  direction (right). e) Schematic of the one-step synthesis process for the binder-free electrode material. f) Galvanostatic charge-discharge profiles at  $0.1 \text{ A g}^{-1}$ . g) Schematic of the stepwise uptake/extraction process of  $\text{Zn}^{2+}$  in different discharge/charge depths. h) Diagram illustrating the formation process of  $\text{V}_3\text{O}_7 \cdot \text{H}_2\text{O}$ /rGO nanobelts. i)  $\text{V}_3\text{O}_7 \cdot \text{H}_2\text{O}$ /rGO at a current density of  $0.1 \text{ A g}^{-1}$ . j) Long-term cycling performance of the  $\text{V}_3\text{O}_7 \cdot \text{H}_2\text{O}$ /rGO at a current density of  $4 \text{ A g}^{-1}$ . k) Illustration of the phase transition during  $\text{Zn}^{2+}$  (de)intercalation. The conversion in the pink and green dash box governs the initial cycles and long-term cycling, respectively. a–d) Reproduced with permission.<sup>[200]</sup> Copyright 2018, WILEY-VCH. e–g) Reproduced with permission.<sup>[201]</sup> Copyright 2021, Elsevier. h–k) Reproduced with permission.<sup>[202]</sup> Copyright 2021, WILEY-VCH.

shown in Figure 9g.



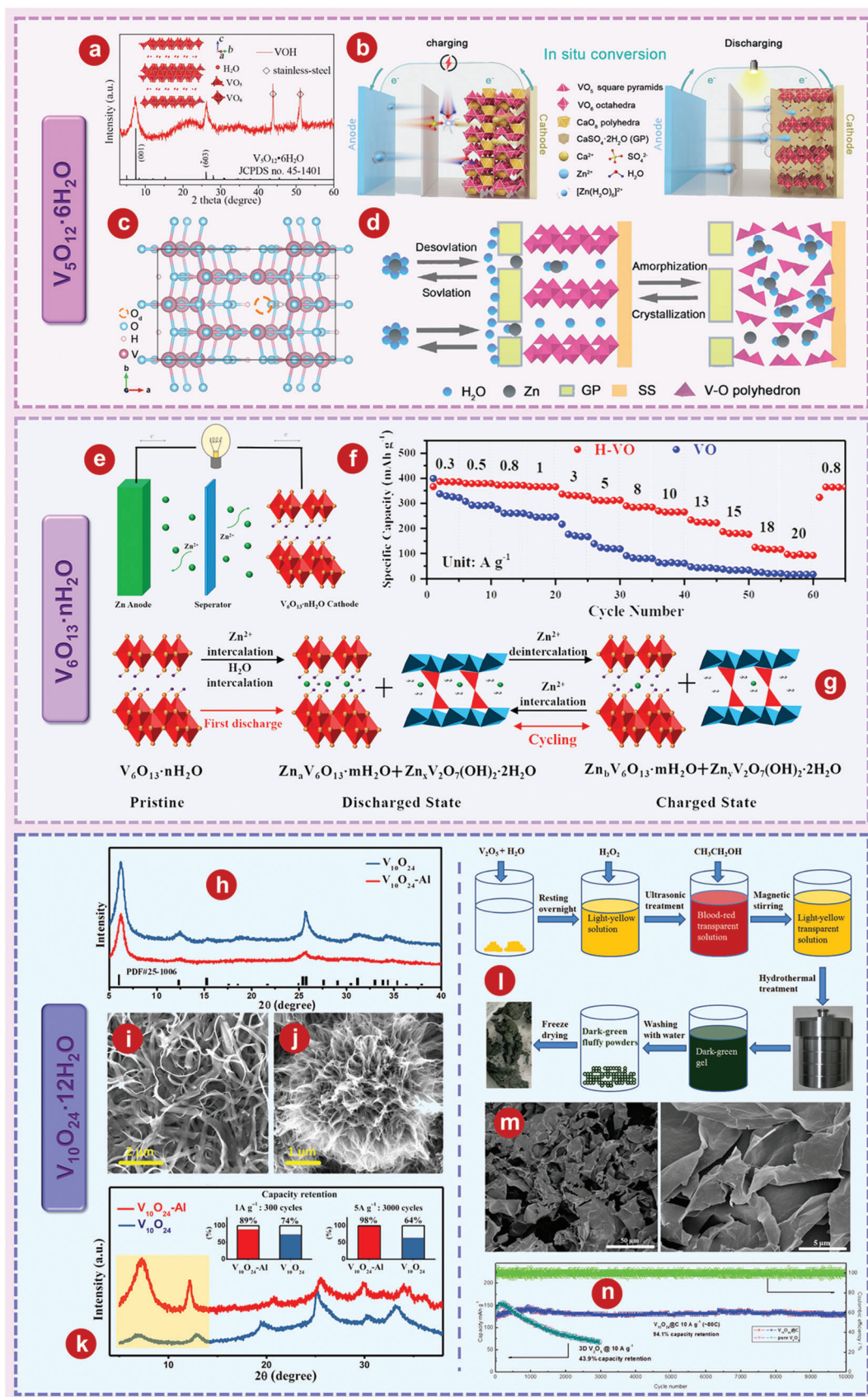
Cao et al.<sup>[202]</sup> developed a microwave-assisted method to one-step prepare  $\text{V}_3\text{O}_7 \cdot \text{H}_2\text{O}$  nanobelts/rGO composite through controlling pH with acids (Figure 9h). The  $\text{V}_3\text{O}_7 \cdot \text{H}_2\text{O}$  nanobelts/rGO composite shows excellent performance with a high initial capacity of  $404.7 \text{ mAh g}^{-1}$  at  $100 \text{ mA g}^{-1}$  (Figure 9i) and a retained capacity of 99.6% after 1000 cycles at  $4 \text{ A g}^{-1}$  (Figure 9j). Cao et al.<sup>[202]</sup> also demonstrated that the hypothesis of the  $\text{Zn}^{2+}$  (de)intercalation process in  $\text{V}_3\text{O}_7 \cdot \text{H}_2\text{O}$  cathode (Figure 9k) was consistent with the experimental results.

### 3.5.4. $\text{V}_5\text{O}_{12} \cdot 6\text{H}_2\text{O}$

Navajoite  $\text{V}_5\text{O}_{12} \cdot 6\text{H}_2\text{O}$ , consisting of bilayers ( $\text{VO}_6$  octahedron and  $\text{VO}_5$  square pyramid) stacked with stably bound

water molecules, is one of the representatives of the layered hydrated vanadium oxide.<sup>[59]</sup> Due to the characteristics of its structure,  $\text{V}_5\text{O}_{12} \cdot 6\text{H}_2\text{O}$  can provide a larger interlayer distance of about 1.18 nm, thus providing open channels for  $\text{Zn}^{2+}$  (de)intercalation. Zhang et al.<sup>[203]</sup> developed a high-performance cathode by uniformly placing the  $\text{V}_5\text{O}_{12} \cdot 6\text{H}_2\text{O}$  nanoribbon cathode on a stainless-steel substrate using a simple electrodeposition technique. Figure 10a shows the XRD pattern of the prepared  $\text{V}_5\text{O}_{12} \cdot 6\text{H}_2\text{O}$  sample. The discharge capacity of  $\text{V}_5\text{O}_{12} \cdot 6\text{H}_2\text{O}$  is  $354.8 \text{ mAh g}^{-1}$  ( $0.5 \text{ A g}^{-1}$ ), the initial CE is up to 99.5%, the energy density is up to  $194 \text{ Wh kg}^{-1}$  ( $2100 \text{ W kg}^{-1}$ ), and the capacity retention rate is up to 94% after 1000 cycles. Huang and coworkers<sup>[204]</sup> made  $\text{CaV}_4\text{O}_9$  cathode reconstruct as the oxygen-deficient  $\text{V}_5\text{O}_{12-x} \cdot 6\text{H}_2\text{O}$  coated by gypsum layers (GP-HVO<sub>d</sub>) through the initial electrochemically charging (Figure 10b). The crystal structure of  $\text{V}_5\text{O}_{12-x} \cdot 6\text{H}_2\text{O}$  (HVO<sub>d</sub>) is shown in Figure 10c. Based on its structure, Huang and colleagues<sup>[204]</sup> used DFT calculations to reveal the role of  $\text{O}_d$  in optimizing electronic properties. The overall  $\text{Zn}^{2+}$  storage mechanism of GP-HVO<sub>d</sub> was shown in Figure 10d. GP-HVO<sub>d</sub> exhibits good performance, with a high capacity of  $402.5 \text{ mAh g}^{-1}$  and excellent cycle stability of 99.7% capacity retention after 200 cycles at  $0.2 \text{ A g}^{-1}$ .





### 3.5.5. $V_6O_{13} \cdot nH_2O$

The intercalation of water in the interlayer expansion  $V_6O_{13} \cdot nH_2O$  is due to the strong intercalation of water molecules and lattice oxygen ions between monolayer and bilayer, forming hydroxyl radicals on each side. The expanded interlayer spacing due to the intercalation of water molecules provides good rate performance and cyclic stability for  $Zn^{2+}$  storage. In addition, the mixed valence of  $V^{4+}$  and  $V^{5+}$  within  $V_6O_{13}$  and high conductivity also provide excellent conditions for Zn ion storage. Lai et al.<sup>[205]</sup> prepared a highly reversible AZIB (Figure 10e) by employing  $V_6O_{13} \cdot nH_2O$  hollow micro-flowers composed of ultra-thin nanosheets as a cathode material. By increasing the current density from 0.3 to 10 A g<sup>-1</sup>, the  $V_6O_{13} \cdot nH_2O$  cathode shows excellent capacities of 386 and 270 mAh g<sup>-1</sup>, respectively, with only a 30% capacity loss, which is much better than  $V_6O_{13}$  cathode. The storage mechanism of  $Zn^{2+}$  is shown in figure 10g. We can clearly see the reaction of the first (dis)charge of  $V_6O_{13} \cdot nH_2O$  cathode and then the steady (dis)charge.

### 3.5.6. $V_{10}O_{24} \cdot 12H_2O$

$V_{10}O_{24} \cdot 12H_2O$  can be understood as a kind of oxygen-deficient  $V_2O_{5-x} \cdot nH_2O$  compound and also a type of typical hybrid valence hydrated vanadium oxide where the molar ratio of the  $V^{5+}/V^{4+}$  is 4.<sup>[206]</sup> However, the current synthesis process of  $V_{10}O_{24} \cdot 12H_2O$  is relatively complex, time-consuming, and less studied.<sup>[207]</sup> Li et al.<sup>[208]</sup> prepared an aluminum-doped  $V_{10}O_{24} \cdot 12H_2O$  as a cathode material for AZIBs. As shown in Figure 10h, there is no obvious peak position shift in aluminum-doped materials, which may be due to the low doping degree. SEM images of  $V_{10}O_{24} \cdot 12H_2O$  and aluminum-doped  $V_{10}O_{24} \cdot 12H_2O$  are shown in Figure 10i,j. Compared with the  $V_{10}O_{24} \cdot 12H_2O$ , the aluminum-doped  $V_{10}O_{24} \cdot 12H_2O$  consists of denser and finer bands mixed together to produce a unified urchin-like state. After 21 days of work and recharging to 1.6 V, the structure of aluminum-doped  $V_{10}O_{24} \cdot 12H_2O$  is not completely destroyed (high-intensity (002) peak), while the layer structure of  $V_{10}O_{24} \cdot 12H_2O$  is almost destroyed (broader and attenuated (002) and (004) peaks), shown in Figure 10k. Wu et al.<sup>[209]</sup> synthesized  $V_{10}O_{24} \cdot 12H_2O$  nanosheets coated with carbon ( $V_{10}O_{24} @C$ ) used as cathode materials for AZIBs (Figure 10l). It's observed that  $V_{10}O_{24} @C$  is a porous 3D structure consisting of a large number of intercalated curved nanosheets, similar to the reported 3D  $V_2O_5$  network and 3D graphene networks (Figure 10m).<sup>[210–215]</sup> As shown in Figure 10n, the  $V_{10}O_{24} @C$  cathode delivers superior perfor-

mance with a capacity retention of 94.1% after 10 000 cycles at a 10 A g<sup>-1</sup>.

## 4. Vanadates

Vanadates have abundant chemical valence vanadium and V–O polyhedron and are easy to deform. Generally, many vanadates are prepared by intercalating vanadate oxides with different kinds of cations. The intercalation of cation can increase vanadium oxide's internal spacing, thus effectively easing the capacity loss of vanadium oxides. In addition, the intercalation of cation has been shown to have a “pillar effect”, enhancing the layered structure and inhibiting “lattice respiration”, thereby enhancing the cycling stability.<sup>[239,240]</sup> So far, researchers have designed many different kinds of metal ions (including monovalent alkali metal cations Li<sup>+</sup>, Na<sup>+</sup>, K<sup>+</sup>, multivalent alkali metal cations Ca<sup>2+</sup>, Mg<sup>2+</sup>, transition metal cations Cu<sup>2+</sup>, Ag<sup>+</sup>, nonmetal cations NH<sub>4</sub><sup>+</sup>, etc.) to intercalate between layers of vanadium oxides to use as cathode materials for AZIBs. In addition, as the important branch of vanadates, hydrated vanadates exhibit unique properties due to the intercalation of water molecules.

### 4.1. Monovalent Alkali Metal Cations

#### 4.1.1. The Intercalation of Li<sup>+</sup>

**$Li_xV_3O_8$ :**  $Li_xV_3O_8$  consists of two edge-shared  $VO_6$  and  $VO_5$  units via corner-sharing, and the  $V_3O_8$ <sup>-</sup> layers are connected by Li<sup>+</sup> at the interstitial octahedral and tetrahedral sites. The stable layered structure of  $Li_{1+x}V_3O_8$ , with high ion diffusion rate, can provide many vacancies for  $Zn^{2+}$  to occupy. In addition, the possibility of metal ion intercalation and the extensive charge balance characteristics of the vanadium redox couple ( $V^{5+}/V^{4+}/V^{3+}$ ) make the layered  $Li_{1+x}V_3O_8$  as a candidate cathode material of AZIBs. Alfuruqi and colleagues<sup>[241]</sup> prepared layered-type  $LiV_3O_8$  as a promising cathode material for AZIBs with high capacity. The schematic diagram of the assembled AZIB based on layered-type  $LiV_3O_8$  cathode is shown in Figure 11a. At 133 mA g<sup>-1</sup>, the  $LiV_3O_8$  cathode has a high specific capacity of 172 mAh g<sup>-1</sup> after 65 cycles, as well as the CE is ≈100%. The electrochemical insertion of  $Zn^{2+}$  in  $LiV_3O_8$  is mainly described by a storage mechanism that shows that zinc transitions in  $LiV_3O_8$  in a single-phase step by step and transitions to  $Zn_xLiV_3O_8$  phase (Figure 11b).

**$Li_3V_6O_{16}$ :** Interestingly, the  $Li_3V_6O_{16}$  and  $Li_xV_3O_8$  are homogeneous and multi-image variants with the same hierarchical

**Figure 10.** a) XRD pattern of the as-prepared VOH cathode grown on stainless-steel mesh. The inset schematically represents the layered structure of VOH. b) Schematic illustration of the crystal structure evolution from CVO to GP-HVO<sub>d</sub>. c) Crystal structure of HVO<sub>d</sub>. d) Schematic diagram of zinc storage mechanism for GP-HVO<sub>d</sub>. e) Schematic illustration of an AZIB Based on  $V_6O_{13} \cdot nH_2O$  cathode and metallic Zn foil anode. f) Rate capabilities of  $V_6O_{13} \cdot nH_2O$  and  $V_6O_{13}$  electrodes. g) Schematic illustration of  $Zn^{2+}$  and water co-intercalation into  $V_6O_{13} \cdot nH_2O$  electrode during the initial discharge process and reversible  $Zn^{2+}$  (de)intercalation in the subsequent process. h) XRD patterns of  $V_{10}O_{24} \cdot 12H_2O$  and aluminum-doped  $V_{10}O_{24} \cdot 12H_2O$ . SEM images of i) pure  $V_{10}O_{24} \cdot 12H_2O$  and j) Al-doped  $V_{10}O_{24} \cdot 12H_2O$ . k) XRD patterns of  $V_{10}O_{24} \cdot 12H_2O$  and aluminum-doped  $V_{10}O_{24} \cdot 12H_2O$  electrodes obtained at the fully charged state after long-term cycles for 21 days (collected at 100 mA g<sup>-1</sup> after 140 cycles). The inserted bar graph provides the comparison of capacity retention at different currents. l) Schematic illustration of fabricating 3D structures of  $V_{10}O_{24} \cdot 12H_2O$  nanosheets coated with carbon ( $V_{10}O_{24} @C$ ). m) SEM images of  $V_{10}O_{24} @C$ . n) The batteries were tested in 3 M aqueous  $Zn(CF_3SO_3)_2$  electrolyte. a) Reproduced with permission.<sup>[203]</sup> Copyright 2019, WILEY-VCH. b–d) Reproduced with permission.<sup>[204]</sup> Copyright 2022, WILEY-VCH. e–g) Reproduced with permission.<sup>[205]</sup> Copyright 2019, American Chemical Society. h–k) Reproduced with permission.<sup>[208]</sup> Copyright 2019, American Chemical Society. l–n) Reproduced with permission.<sup>[209]</sup> Copyright 2021, American Chemical Society.



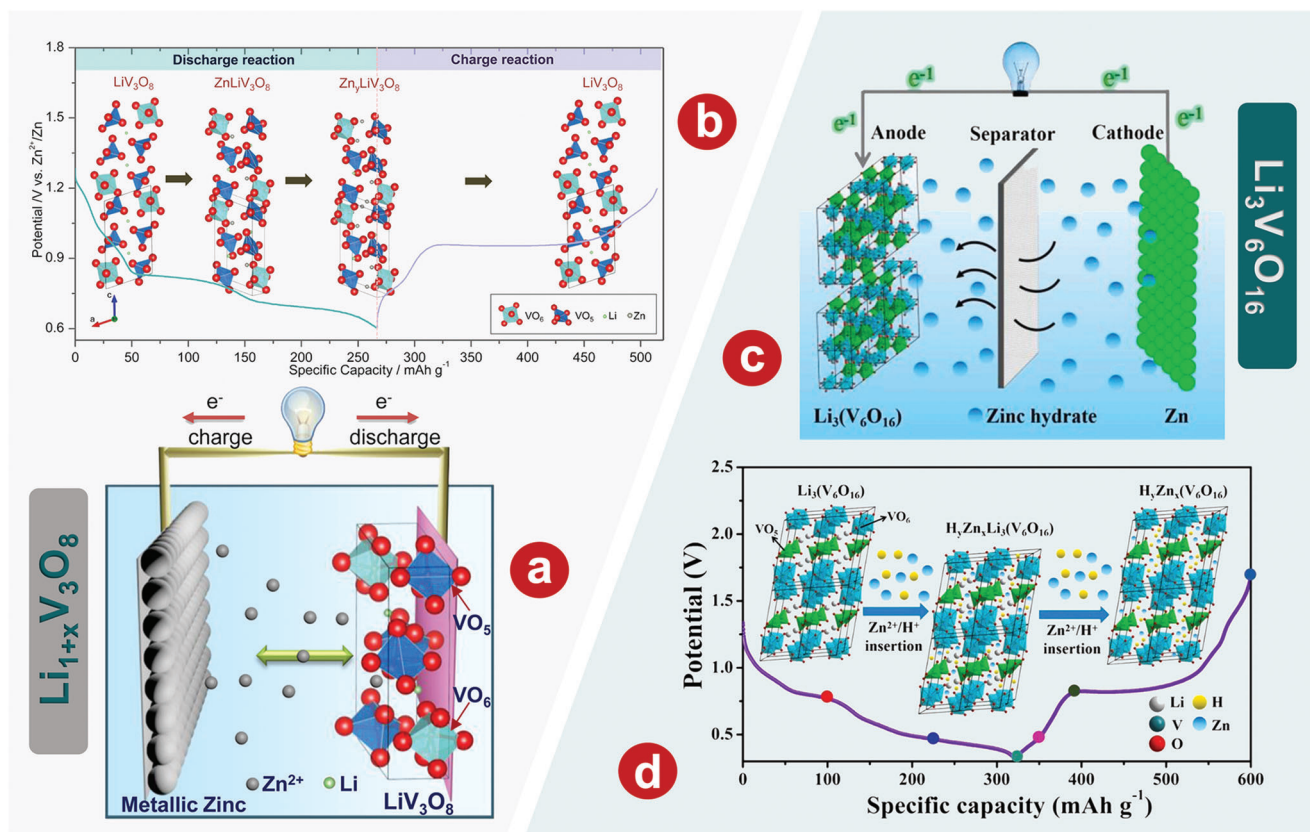


**Figure 11.** a) Schematic diagram of Zn-LiV<sub>3</sub>O<sub>8</sub> battery. b) Schematic of the Zn-intercalation mechanism in the present LiV<sub>3</sub>O<sub>8</sub> cathode. c) Schematic diagram of Zn-Li<sub>3</sub>V<sub>6</sub>O<sub>16</sub> battery. d) Schematic diagram of the storage mechanism of Zn<sup>2+</sup> in the Li<sub>3</sub>V<sub>6</sub>O<sub>16</sub>//Zn battery. (a, b) Reproduced with permission.<sup>[241]</sup> Copyright 2017, American Chemical Society. c, d) Reproduced with permission.<sup>[242]</sup> Copyright 2022, Elsevier.

structure and similar performance. Ran et al.<sup>[242]</sup> prepared the Li<sub>3</sub>V<sub>6</sub>O<sub>16</sub> as cathode material of AZIBs with high storage capacity via a one-step molten salt method. The schematic diagram of the AZIB based on Li<sub>3</sub>V<sub>6</sub>O<sub>16</sub> cathode is shown in Figure 12c. The Li<sub>3</sub>V<sub>6</sub>O<sub>16</sub> shows superior electrochemical performance with 350 mAh g<sup>-1</sup> at 0.1 A g<sup>-1</sup>. As shown in Figure 12d, Ran et al.<sup>[242]</sup> also proved that the electrochemical mechanism of the Li<sub>3</sub>V<sub>6</sub>O<sub>16</sub> cathode is Zn<sup>2+</sup> and H<sup>+</sup> co-intercalation.

#### 4.1.2. The Intercalation of Na<sup>+</sup>

**Na<sub>1.1</sub>V<sub>3</sub>O<sub>7.9</sub>:** Na<sub>1.1</sub>V<sub>3</sub>O<sub>7.9</sub> shows a layered structure that consists of alternating VO<sub>6</sub> octahedron and VO<sub>4</sub> tetrahedron, connected by O atoms with shared corners. The sodium ions occupy two separate positions. One is a fully occupied octahedral site and the other is a partially occupied tetrahedral site. In this layered structure, sodium or zinc ions have an open and stable interstitial channel during de(inter)calation.<sup>[243–245]</sup> Cai and coworkers<sup>[246]</sup> first synthesized the ignition Na<sub>1.1</sub>V<sub>3</sub>O<sub>7.9</sub> nanoribbons/graphene composites, by a simple hydrothermal method, followed by freeze-drying (Figure 12a). The schematic diagram of the structural framework of Na<sub>1.1</sub>V<sub>3</sub>O<sub>7.9</sub> is shown in Figure 12b. When used as a cathode material for AZIBs, the composite can reach a maximum value of 223 mA h g<sup>-1</sup> after 14 cycles at 300 mA g<sup>-1</sup> (Figure 12c) and has good cycle stability, indicat-

ing that Na<sub>1.1</sub>V<sub>3</sub>O<sub>7.9</sub> is a good candidate material for the cathode of AZIBs. Islam et al.<sup>[247]</sup> used PPy coating to enhance the electrochemical performance of Na<sub>1.1</sub>V<sub>3</sub>O<sub>7.9</sub>. Na<sub>1.1</sub>V<sub>3</sub>O<sub>7.9</sub> coated with PPy (P-NVO) was synthesized by microwave-assisted hydrothermal method followed by calcined, and finally mixed with PPy in dry ethanol (Figure 12d). The highly conductive polypyridine surface coating is of great significance to improve the conductivity of Zn<sup>2+</sup> and the kinetics of Zn<sup>2+</sup> diffusion, which can enable the Na<sub>1.1</sub>V<sub>3</sub>O<sub>7.9</sub> cathode to perform V<sup>3+</sup>/V<sup>4+</sup>/V<sup>5+</sup> multiple redox reactions in AZIBs. Even at high current densities of 6000 mA g<sup>-1</sup>, the P-NVO cathode shows unprecedented cycle stability over 1100 cycles without capacity loss.

**The Intercalation of Organic Molecules in Na<sub>0.76</sub>V<sub>6</sub>O<sub>15</sub>:** Na<sub>0.76</sub>V<sub>6</sub>O<sub>15</sub> have a 3D rigid tunnel structure, can effectively alleviate the collapse of the structure, and the Zn<sup>2+</sup> is reversible de(inter)calation. The tunneled Na<sub>0.76</sub>V<sub>6</sub>O<sub>15</sub> consists of VO<sub>6</sub> octahedron, which is connected to each other by V–O<sub>b</sub> bonds and to the layer by V–O<sub>c</sub> bonds. Based on crystal symmetry, there are three sites in tunnel Na<sub>0.76</sub>V<sub>6</sub>O<sub>15</sub>: O<sub>v</sub> (Site 1), O<sub>b</sub> (Site 2), and O<sub>c</sub> (Site 3), as shown in Figure 12e. Bi et al.<sup>[248]</sup> investigated the application of poly(3,4-ethylenedioxythiophene) (PEDOT) coatings in AZIBs by in situ polymerization to introduce oxygen vacancies in Na<sub>0.76</sub>V<sub>6</sub>O<sub>15</sub> nanoribbons (Vo<sup>••</sup>-PNVO). The rapid reversible diffusion and intercalation of Zn<sup>2+</sup> are achieved by introducing “oxygen vacancies”, which enlarge the interplanar space and weakened the electrostatic interaction. At 50 mA g<sup>-1</sup>,

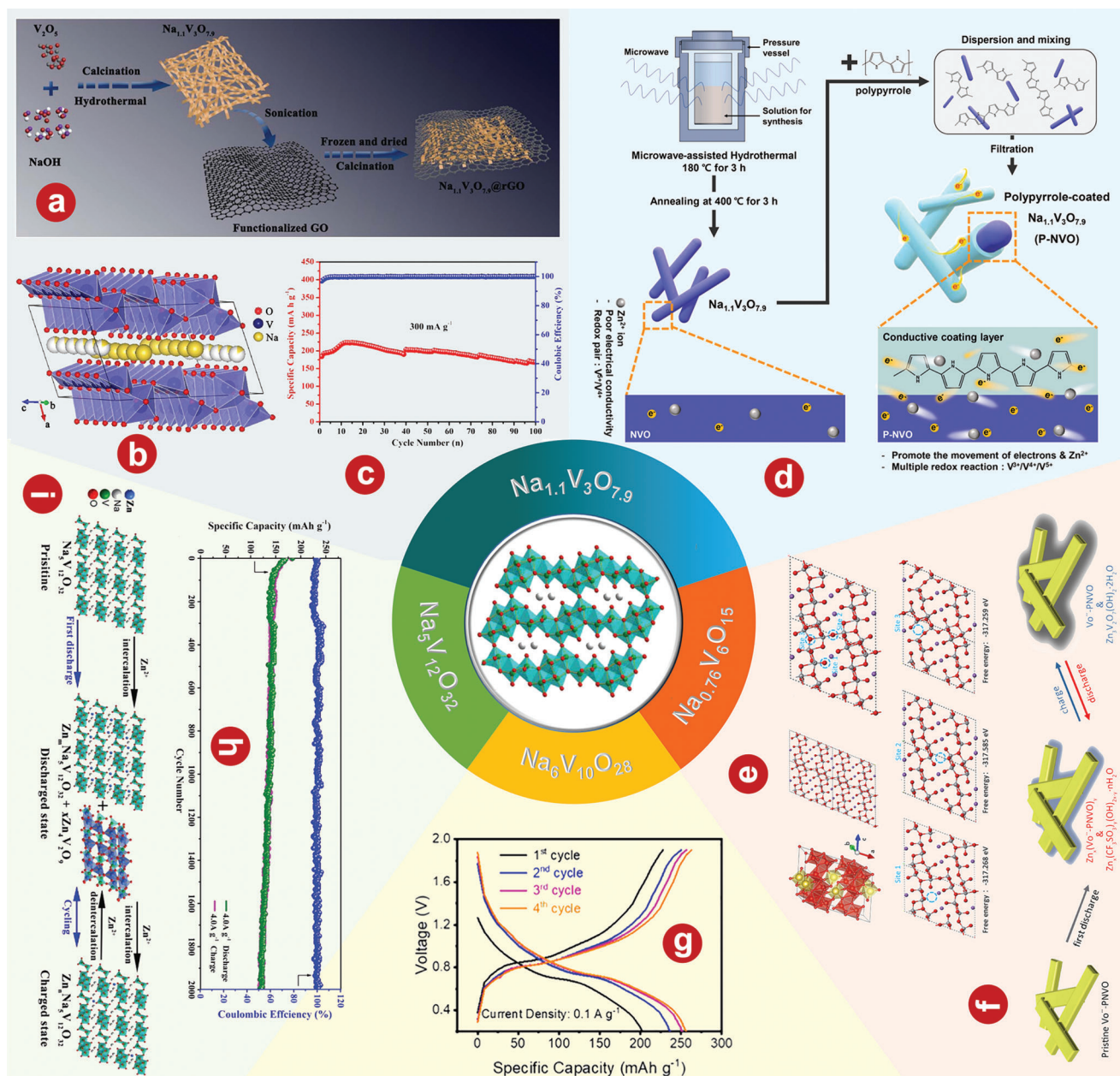


**Figure 12.** a) Illustration of synthesis procedure of pilotaxitic  $\text{Na}_{1.1}\text{V}_3\text{O}_{7.9}$  nanoribbons/rGO. b) The structural framework of  $\text{Na}_{1.1}\text{V}_3\text{O}_{7.9}$ . c) The cycling performance of  $\text{Na}_{1.1}\text{V}_3\text{O}_{7.9}$ @rGO for AZIBs at  $300 \text{ mA g}^{-1}$ . d) Schematic illustration of the synthesis of  $\text{Na}_{1.1}\text{V}_3\text{O}_{7.9}$  and  $\text{Na}_{1.1}\text{V}_3\text{O}_{7.9}$ /PPy cathode for AZIBs. e) The crystal structure of NVO, the possible sites for oxygen vacancies in  $\text{Na}_{0.76}\text{V}_6\text{O}_{15}$  nanobelts (left), and corresponding calculated free energy. The smallest free energy on Site 2 suggests  $\text{O}_b$  site is the location of oxygen vacancies in  $\text{Vo}^{\cdot\cdot}$ -PNVO (right). f) Illustration of the energy storage mechanism of  $\text{Vo}^{\cdot\cdot}$ -PNVO. g) Galvanostatic charge-discharge plots of the first four cycles at a current density of  $0.1 \text{ A g}^{-1}$  of  $\text{Na}_5\text{V}_{10}\text{O}_{28}$ . h) Long-term cycling performance at  $4 \text{ A g}^{-1}$  of  $\text{Na}_5\text{V}_{10}\text{O}_{28}$ . i) Schematic illustration of  $\text{Zn}^{2+}$  (de)intercalation process of  $\text{Na}_5\text{V}_{10}\text{O}_{28}$  during cycling. a–c) Reproduced with permission.<sup>[246]</sup> Copyright 2018, Elsevier. d) Reproduced with permission.<sup>[247]</sup> Copyright 2022, Elsevier. e, f) Reproduced with permission.<sup>[248]</sup> Copyright 2021, Elsevier. g) Reproduced with permission.<sup>[250]</sup> Copyright 2022, Elsevier. h, i) Reproduced with permission.<sup>[254]</sup> Copyright 2018, WILEY-VCH.

$\text{Vo}^{\cdot\cdot}$ -PNVO cathode exhibits an improved specific capacity of  $355 \text{ mA h g}^{-1}$ . According to the ex situ XRD, XPS, and SEM results, the energy storage mechanism of  $\text{Vo}^{\cdot\cdot}$ -PNVO is shown in Figure 12f.

$\text{Na}_6\text{V}_{10}\text{O}_{28}$ : PVOs-typed  $\text{Na}_6\text{V}_{10}\text{O}_{28}$  is composed of 1  $\text{V}_{10}\text{O}_{28}^{6-}$ , 2  $\text{Na}(\text{H}_2\text{O})_4^+$ , 2  $\text{Na}_2(\text{H}_2\text{O})_3^{2+}$  and 4 additional water

molecules, respectively. The  $\text{V}_{10}\text{O}_{28}^{6-}$  is composed of 10  $\text{VO}_6$  polyhedron, among which 6  $\text{VO}_6$  octahedrons are arranged in a  $2 \times 3$  rectangular array by shared edges and the remaining 4  $\text{VO}_6$  octahedrons are distributed on the upper and lower sides through shared sloping edges.<sup>[249]</sup> In accordance with the above structure, discrete components of polyanion, and extended the



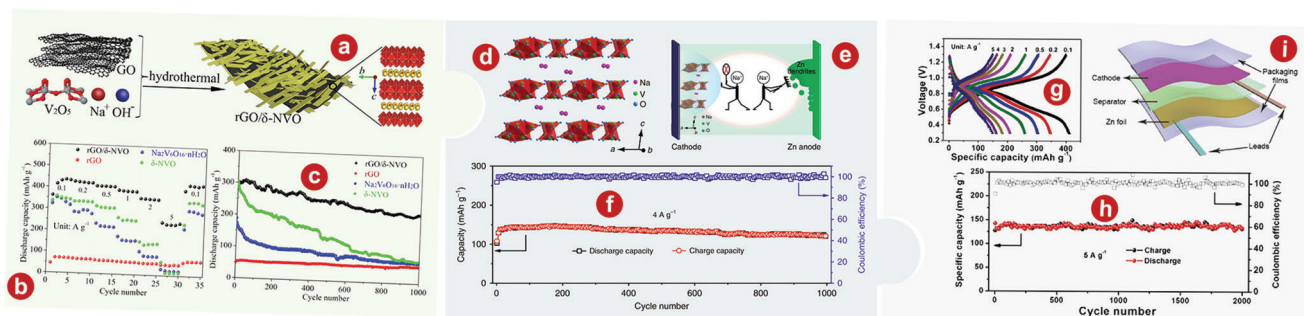


**Figure 13.** a) The synthesis procedure and crystallographic structure of  $\delta$ -type  $\text{Na}_x\text{V}_2\text{O}_5 \cdot n\text{H}_2\text{O}$ . b) Rate performances of four samples at current densities from 0.1 to 5  $\text{A g}^{-1}$ . c) Cycling performances at 2  $\text{A g}^{-1}$ . d) Crystal structure of  $\text{NaV}_3\text{O}_8 \cdot 1.5\text{H}_2\text{O}$  nanobelts,  $\text{Na}^+$  exists in the form of hydrated ion. e) Schematic diagram:  $\text{Na}_2\text{SO}_4$  additive suppresses the dissolution of  $\text{NaV}_3\text{O}_8 \cdot 1.5\text{H}_2\text{O}$  nanobelts and the formation of zinc dendrites. f) Long-term cycle life of  $\text{Zn}/\text{NaV}_3\text{O}_8 \cdot 1.5\text{H}_2\text{O}$  batteries in 1 M  $\text{ZnSO}_4$  electrolyte with 1 M  $\text{Na}_2\text{SO}_4$  additive at 4  $\text{A g}^{-1}$ . g) Charge/discharge curves of  $\text{rGO}/\text{NVO}$ -70% composite film-based AZIBs at different current densities. h) Long cycle life of  $\text{rGO}/\text{NaV}_3\text{O}_8 \cdot 1.5\text{H}_2\text{O}$  -70% composite film-based AZIBs at 5  $\text{A g}^{-1}$ . i) Schematic diagram of flexible soft-packaged AZIBs. a–c) Reproduced with permission.<sup>[256]</sup> Copyright 2019, Elsevier. d–f) Reproduced with permission.<sup>[62]</sup> Copyright 2018, Nature. g, h) Reproduced with permission.<sup>[259]</sup> Copyright 2019, Springer.

absence of the crystal structure, making the storage of  $\text{Zn}^{2+}$  easier to (de)intercalate. In addition, the storage mechanism for this process is (de)intercalate of  $\text{Zn}^{2+}$  between  $\text{V}_{10}\text{O}_{28}^{6-}$  rather than entry into the crystal structure. Zhou et al.<sup>[250]</sup> first applied PVOs-typed  $\text{Na}_6\text{V}_{10}\text{O}_{28}$  as a cathode material for AZIB and verified its feasibility. The high stability of the  $\text{V}_{10}\text{O}_{28}^{6-}$  cluster allows the material to support reversible intercalation of  $\text{Zn}^{2+}$ . Thus, the  $\text{Na}_6\text{V}_{10}\text{O}_{28}$  cathode provides a high capacity of 279.5  $\text{mAh g}^{-1}$  (Figure 12g) and excellent cycle performance.

**$\text{Na}_5\text{V}_{12}\text{O}_{32}$ :** Among the sodium vanadates,  $\text{Na}_5\text{V}_{12}\text{O}_{32}$  has many oxidation states, high specific capacity, good structural stability, low cost, and safety, which is considered as a promising cathode material.<sup>[251]</sup> The crystal structure of  $\text{Na}_5\text{V}_{12}\text{O}_{32}$  is a layered structure composed of  $\text{V}_3\text{O}_8$  polyhedral layers, and sodium ions are mainly located in the octahedral position between the layers. The sodium ions located in the octahedral position act as pillar cations to stabilize the structure, making this structure very favorable.<sup>[252,253]</sup> Guo et al.<sup>[254]</sup> purposefully selected and constructed three sodium vanadate nanoribbons with typical  $\text{NaV}_3\text{O}_8$  layered structures ( $\text{Na}_5\text{V}_{12}\text{O}_{32}$ ,  $\text{HNaV}_6\text{O}_{16} \cdot 4\text{H}_2\text{O}$  and  $\text{Na}_{0.76}\text{V}_6\text{O}_{15}$ ), and applied them in AZIBs.  $\text{Na}_5\text{V}_{12}\text{O}_{32}$  has a higher capacity than  $\text{Na}_{0.76}\text{V}_6\text{O}_{15}$ , with a long-term cycle performance of up to 2000 cycles at 4.0  $\text{A g}^{-1}$  despite capacity reduction (Figure 12h). Based on ex situ transmission electron microscopy (TEM) images and ex situ X-ray photoelectron spectroscopy (XPS), Guo et al.<sup>[254]</sup> demonstrated the  $\text{Zn}^{2+}$  de(inter)calation process during  $\text{Na}_5\text{V}_{12}\text{O}_{32}$  cycling (Figure 12i).

#### 4.1.3. The Co-Intercalation of $\text{Na}^+$ and $\text{H}_2\text{O}$

**$\text{Na}_x\text{V}_2\text{O}_5 \cdot n\text{H}_2\text{O}$ :** In crystal structure of  $\delta$ -type  $\text{Na}_x\text{V}_2\text{O}_5 \cdot n\text{H}_2\text{O}$ , interlayer  $\text{H}_2\text{O}$  molecules and  $\text{Na}^+$  can act as pillars to stabilize the  $\text{V}_2\text{O}_5$  layer and shield electrostatic interactions between cations intercalation during (de)charging. However,  $\delta$ -type  $\text{Na}_x\text{V}_2\text{O}_5 \cdot n\text{H}_2\text{O}$  has low conductivity compared with other vanadium-based compounds, which is not conducive to electrochemical energy storage. Graphene is proving to be an excellent functional material as the scaffold to solve the problem of low conductivity of vanadium-based cathode materials.<sup>[255]</sup> Zhou

et al.<sup>[256]</sup> first prepared a  $\delta$ -type  $\text{Na}_x\text{V}_2\text{O}_5 \cdot n\text{H}_2\text{O}$  hybrid with rGO (Figure 13a), which showed better electrochemical performance than  $\text{Na}_2\text{V}_6\text{O}_{16} \cdot n\text{H}_2\text{O}$  under the same conditions. The prepared  $\delta$ -type  $\text{Na}_x\text{V}_2\text{O}_5 \cdot n\text{H}_2\text{O}$  hybrid with rGO has a good reversible capacity of 433.5  $\text{mAh g}^{-1}$  at 0.1  $\text{A g}^{-1}$ , an excellent rate capability of 244.1  $\text{mAh g}^{-1}$  at 5  $\text{A g}^{-1}$  (Figure 13b). In addition, the  $\delta$ -type  $\text{Na}_x\text{V}_2\text{O}_5 \cdot n\text{H}_2\text{O}$  hybrid with rGO also shows superior cycling stability of 70.5% more than 1000 cycles (Figure 13c).

**$\text{NaV}_3\text{O}_8 \cdot 1.5\text{H}_2\text{O}$ :** In the crystal structure of  $\text{NaV}_3\text{O}_8 \cdot 1.5\text{H}_2\text{O}$  (Figure 13d), hydrated  $\text{Na}^+$  are positioned between layers  $\text{V}_3\text{O}_8$  as pillars to stabilize the layered structure composed of a  $\text{VO}_5$  tetragonal bipyramid and a  $\text{VO}_6$  octahedron. Except for  $\text{Na}^+$ , which is easy to intercalate, the interlayer distance of  $\text{NaV}_3\text{O}_8$  (7.08 Å) is large enough to intercalate  $\text{Zn}^{2+}$  (0.74 Å), and  $\text{H}^+$  can stably exist between layers of  $\text{V}_3\text{O}_8$ .<sup>[257,258]</sup> Wang et al.<sup>[62]</sup> developed a highly reversible zinc vanadate/sodium vanadate system with  $\text{NaV}_3\text{O}_8 \cdot 1.5\text{H}_2\text{O}$  nanoribbon as the positive electrode and zinc sulfate aqueous solution of sodium sulfate additive as the electrolyte.  $\text{Na}_2\text{SO}_4$  additive inhibited the dissolution of  $\text{NaV}_3\text{O}_8 \cdot 1.5\text{H}_2\text{O}$  nanoribbons and the formation of zinc dendrites (Figure 13e). The reversible capacity of the zinc/sodium vanadate hydrate cell is 380  $\text{mAh g}^{-1}$ , and the capacity retention rate is up to 82% after 1000 cycles (Figure 13f). On the basis of the above research, Wan et al.<sup>[259]</sup> prepared an independent  $\text{rGO}/\text{NaV}_3\text{O}_8 \cdot 1.5\text{H}_2\text{O}$  nanocomposite film by vacuum filtration method to solve the problem of low conductivity of  $\text{NaV}_3\text{O}_8 \cdot 1.5\text{H}_2\text{O}$ . The  $\text{rGO}/\text{NaV}_3\text{O}_8 \cdot 1.5\text{H}_2\text{O}$  composite films have a unique interconnected multilayer structure and many pores, so they have high electronic conductivity and abundant ion transport channels, showing a high capacity of 410  $\text{mAh g}^{-1}$  at 0.1  $\text{A g}^{-1}$  (Figure 13g) and superior cycling stability with 94% after 2000 cycles (Figure 13h). In addition, Wan et al.<sup>[259]</sup> also made based on flexible soft  $\text{rGO}/\text{NaV}_3\text{O}_8 \cdot 1.5\text{H}_2\text{O}$  composite film packaging AZIBs to prove the concept (Figure 13i).

#### 4.1.4. The Intercalation of $\text{K}^+$

**$\text{K}_x\text{V}_2\text{O}_5$ :** In the structure of  $\text{K}_x\text{V}_2\text{O}_5$ , potassium ions are intercalated into the gap between the  $\text{VO}_6$  octahedron,<sup>[260,261]</sup> which



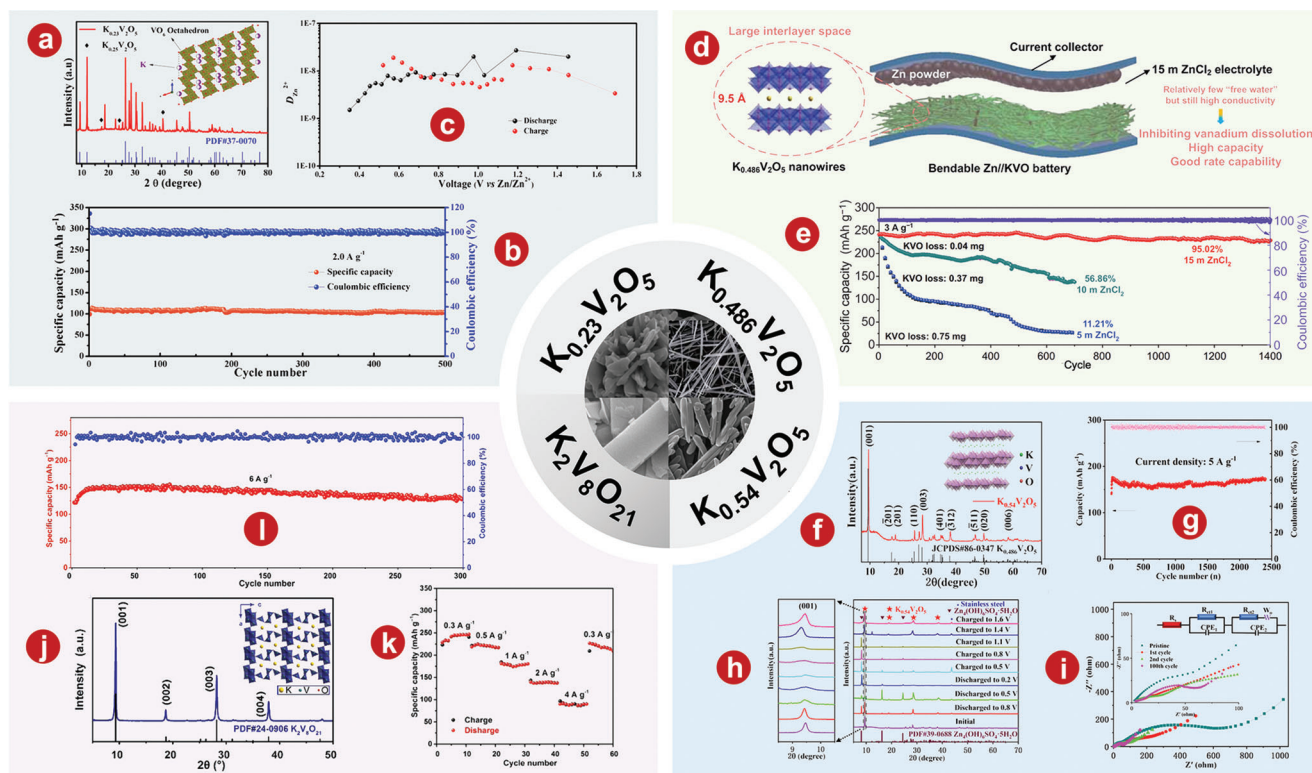


**Figure 14.** a) XRD pattern and the crystal structure of  $\text{K}_{0.23}\text{V}_2\text{O}_5$ . b) Cyclic performance of the  $\text{K}_{0.23}\text{V}_2\text{O}_5$  electrode measured at  $2.0 \text{ A g}^{-1}$ . c) Diffusion coefficients of  $\text{Zn}^{2+}$  in the  $\text{K}_{0.23}\text{V}_2\text{O}_5$  during charge/discharge process. d) Schematic illustration of bendable  $\text{Zn} // \text{K}_{0.486}\text{V}_2\text{O}_5$  battery with regulating electrolyte concentration. e) Cycle stability comparison in 5, 10, and 15 m  $\text{ZnCl}_2$  electrolytes at  $3 \text{ A g}^{-1}$ . f) XRD pattern and the crystal structure of  $\text{K}_{0.54}\text{V}_2\text{O}_5$ . g) Long cycle performance of  $\text{K}_{0.54}\text{V}_2\text{O}_5$  at  $5.0 \text{ A g}^{-1}$ . h) XRD patterns of  $\text{K}_{0.54}\text{V}_2\text{O}_5$  during the initial discharge and charge cycle. i) EIS spectrum of the  $\text{K}_{0.54}\text{V}_2\text{O}_5$  electrode before and after cycling. j) XRD pattern and the crystal structure of  $\text{K}_2\text{V}_8\text{O}_{21}$ . k) Rate capability of the  $\text{Zn} // \text{K}_2\text{V}_8\text{O}_{21}$  battery. l) Long-term cycling performance at  $6 \text{ A g}^{-1}$  of the  $\text{Zn} // \text{K}_2\text{V}_8\text{O}_{21}$  battery. a–c) Reproduced with permission. [266] Copyright 2019, Elsevier. d, e) Reproduced with permission. [267] Copyright 2021, Springer. f–i) Reproduced with permission. [268] Copyright 2022, American Chemical Society. j–l) Reproduced with permission. [269] Copyright 2018, Elsevier

increases the d spacing during  $\text{Zn}^{2+}$  (de)intercalation and reduces the charge polarization effect, thus enhancing the structural stability and electrochemical performance. [262] In addition, the atomic radius of  $\text{K}^+$  is larger than that of  $\text{Li}^+$ ,  $\text{Na}^+$ , and  $\text{Zn}^{2+}$ , which can become a stronger “pillar” between vanadium and oxygen layers, [263] thus enhancing the structural stability of the material. [264,265] Zhang et al. [266] synthesized  $\text{K}_{0.23}\text{V}_2\text{O}_5$  with tunnel structure by hydrothermal method, which was first used as a cathode material for AZIBs. The XRD pattern and the crystal structure of  $\text{K}_{0.23}\text{V}_2\text{O}_5$  are shown in Figure 14a. The  $\text{K}_{0.23}\text{V}_2\text{O}_5$  cathode has excellent structural stability and high-capacity retention of 92.8% after 500 cycles at  $2.0 \text{ A g}^{-1}$  (Figure 14b). Furthermore, as shown in Figure 14c, the ion diffusion rate is up to  $1.88 \times 10^{-9}$ – $2.6 \times 10^{-8} \text{ cm}^2 \text{ s}^{-1}$ , which is much higher than most other cathode materials of AZIBs. Li et al. [267] further developed a AZIB with high performance consisting of a layered  $\text{K}_{0.486}\text{V}_2\text{O}_5$  nanowire cathode with large interlayer spacing and a Zn powder anode (Figure 14d). When the optimum concentration of  $\text{ZnCl}_2$  electrolyte is 15 m, the cycle stability of  $\text{K}_{0.486}\text{V}_2\text{O}_5$  is the best, and the capacity retention rate is 95.02% after 1400 cycles (Figure 14e). The work of Li et al. [267] illustrates the feasibility of using moderately concentrated electrolytes to solve the stability problem of aqueous-soluble electrode materials. In addition,

Wu et al. [268] prepared a nanorod-shaped  $\text{K}_{0.54}\text{V}_2\text{O}_5$ , which is a promising cathode material for AZIBs. The crystal structure information of the  $\text{K}_{0.54}\text{V}_2\text{O}_5$  is shown in the XRD pattern in Figure 14f. The  $\text{K}_{0.54}\text{V}_2\text{O}_5$  cathode delivers superior electrochemical performance with a capacity retention rate of 97% ( $176 \text{ mA h g}^{-1}$ ) after 2400 cycles at  $5 \text{ A g}^{-1}$ , as shown in Figure 14g. In addition, as shown in Figure 14h, the discharge diffraction peak of the 50th sample is similar to that of the 100th sample, which also proves its excellent performance and cyclic stability. As shown in Figure 14i, the curve radius changed a little after the second cycle and the 100th cycle, which indicates that this material structure tends to be stable during the process of  $\text{Zn}^{2+}$  (de)intercalation.

$\text{K}_2\text{V}_8\text{O}_{21}$ : The tunnel structure of  $\text{K}_2\text{V}_8\text{O}_{21}$  consists of a vanadate framework consisting of a  $\text{VO}_6$  octahedron and a  $\text{VO}_5$  pyramid forming  $[\text{V}_8\text{O}_{21}]^{2-}$  units along the b-axis, while  $\text{K}^+$  fill the tunnel as “pillars” to stabilize the structure. Tang et al. [269] successfully synthesized  $\text{K}_2\text{V}_8\text{O}_{21}$  nanobelts,  $\text{K}_{0.25}\text{V}_2\text{O}_5$  nanobelts,  $\text{KV}_3\text{O}_8$  nanobelts, and  $\text{K}_2\text{V}_6\text{O}_{16} \cdot 1.57\text{H}_2\text{O}$  nanobelts, and applied them to AZIBs cathode for the first time. Figure 14j shows the XRD pattern of  $\text{K}_2\text{V}_8\text{O}_{21}$ . Of the four potassium vanadates,  $\text{K}_2\text{V}_8\text{O}_{21}$  cathode showed the best zinc storage performance due to the stable tunnel structure, with a capacity of  $247 \text{ mAh g}^{-1}$  at  $0.3 \text{ A g}^{-1}$  (Figure 14k), and superior capacity retention

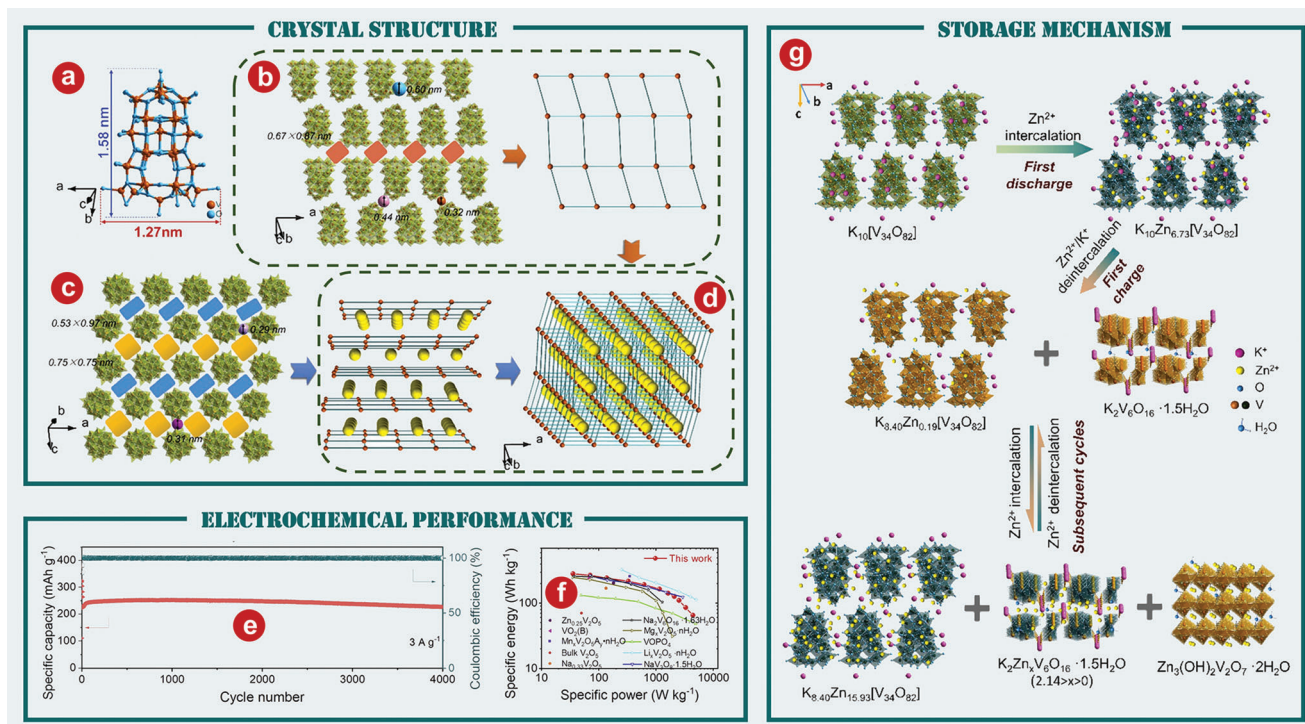


**Figure 15.** a) The molecular structure of the  $[V^{IV}_{16}V^{V}_{18}O_{82}]^{10-}$  polyoxoanion in  $K_{10}[V^{IV}_{16}V^{V}_{18}O_{82}] \cdot 20H_2O$ . Vanadium: orange, oxygen: blue. b) View of the staggered packing of  $[V^{IV}_{16}V^{V}_{18}O_{82}]^{10-}$  along the (0 1 -1) face and its topological view in  $K_{10}[V^{IV}_{16}V^{V}_{18}O_{82}] \cdot 20H_2O$ . c) The (0 1 1) face of  $[V^{IV}_{16}V^{V}_{18}O_{82}]^{10-}$  arrangement and their  $Zn^{2+}$  migration channels highlighted by the rectangles (blue and yellow) and the balls (purple and pink). d) Topologic images of hierarchical interconnected channels based on (0 1 -1) face stacked along b axis. The continuous yellow balls highlight the migration pathways. e) Long-cycle performance of the battery equipped with  $K_{10}[V^{IV}_{16}V^{V}_{18}O_{82}]$  cathode at  $3 A g^{-1}$ . f) Ragone plots: comparison of energy and power densities of the Zn/ $K_{10}[V^{IV}_{16}V^{V}_{18}O_{82}]$  battery with ZIBs based on other reported cathodes. g) Schematic illustration of  $Zn^{2+}$  intercalation/deintercalation process of the  $K_{10}[V^{IV}_{16}V^{V}_{18}O_{82}]$  cathode during cycling. Reproduced with permission.<sup>[270]</sup> Copyright 2020, Elsevier.

of 83% after 300 cycles even at a high current density of  $6 A g^{-1}$  (Figure 14l).

**$K_{10}[V^{IV}_{16}V^{V}_{18}O_{82}]$ :** The nanosized ellipsoid-shaped  $[V^{IV}_{16}V^{V}_{18}O_{82}]^{10-}$  polyoxoanion is constructed from a central  $V_4O_8$  cube and 30  $VO_5$  square pyramids through 26  $\mu_2$ - and 4  $\mu_3$ -oxygen atoms. In addition, the 3D packing alignment of  $[V^{IV}_{16}V^{V}_{18}O_{82}]^{10-}$  polyoxoanions and  $K^+$  ions result in available multidimensional interconnected  $Zn^{2+}$  (de)intercalation channels. Yang et al.<sup>[270]</sup> first prepared the hybrid valence  $K_{10}[V^{IV}_{16}V^{V}_{18}O_{82}]$  cluster with nanoscale as cathode material of AZIBs for  $Zn^{2+}$  energy storage. The  $K_{10}[V^{IV}_{16}V^{V}_{18}O_{82}]$  was obtained by drying  $K_{10}[V^{IV}_{16}V^{V}_{18}O_{82}] \cdot 20H_2O$  in a nitrogen atmosphere at  $200^\circ C$  for three hours. The molecular structure of the  $[V^{IV}_{16}V^{V}_{18}O_{82}]^{10-}$  polyoxoanion in  $K_{10}[V^{IV}_{16}V^{V}_{18}O_{82}] \cdot 20H_2O$  is shown in Figure 15a. Figure 15b–d gives a deeper description of the structure of  $K_{10}[V^{IV}_{16}V^{V}_{18}O_{82}] \cdot 20H_2O$ . The  $K_{10}[V^{IV}_{16}V^{V}_{18}O_{82}]$  cluster constructed hierarchical interconnected migration channels in different spatial dimensions and improved the  $Zn^{2+}$  transport capacity. The prepared Zn/ $K_{10}[V^{IV}_{16}V^{V}_{18}O_{82}]$  battery has good cycle stability with a capacity retention rate of 93% over 4000 cycles at  $3 A g^{-1}$  (Figure 15e), and good energy of  $285 Wh kg^{-1}$  and power density of  $4.5 kW kg^{-1}$  (Figure 15f). According to the previous research,<sup>[269]</sup> Yang et al.<sup>[270]</sup> came up with a logical storage mechanism for the  $K_{10}[V^{IV}_{16}V^{V}_{18}O_{82}]$  cathode during cycling, as shown in Figure 15g.

#### 4.1.5. The Co-Intercalation of $K^+$ and $H_2O$

**$KV_3O_8 \cdot 0.75H_2O$ :** Due to less structural water,  $KV_3O_8 \cdot 0.75H_2O$  exhibits better structural stability than  $NaV_3O_8 \cdot 1.5H_2O$  in aqueous solution.<sup>[62]</sup> The  $KV_3O_8 \cdot 0.75H_2O$  cathode uses  $V_3O_8$  as the skeleton layer, which has a high capacity due to the redox effect of  $V^{3+}/V^{5+}$  pairs and large layer spacing. Wan et al.<sup>[271]</sup> prepared  $KV_3O_8 \cdot 0.75H_2O$  and further integrated it into SWCNTs (SW = single wall) network by a spray printing strategy to achieve independent  $KV_3O_8 \cdot 0.75H_2O$ /SWCNTs composite films (Figure 16a). The  $KV_3O_8 \cdot 0.75H_2O$  cathode delivers a high capacity of  $379 mAh g^{-1}$ , superior rate capability, as well as a high capacity of 91% to maintain stable cycling performance after 10 000 cycles at  $5 A g^{-1}$  (Figure 16b). As shown in Figure 16c, Wan et al.<sup>[271]</sup> also studied the structural evolution of  $KV_3O_8 \cdot 0.75H_2O$  during (dis)charging by using in situ XRD.

**$K_{1.15}V_5O_{13} \cdot 1.3H_2O$ :** On the basis of the work proposed by Wan et al. to composite  $KV_3O_8 \cdot 0.75H_2O$  with SWCNTs, Qiu and colleagues<sup>[272]</sup> reported potassium vanadate nanoribbons as a promising cathode for AZIBs. By XRD pattern (Figure 16d) and energy dispersive spectrometer (EDS) of sample, the molecular formula of the sample is  $K_{1.15}V_5O_{13} \cdot 1.3H_2O$ . The  $K_{1.15}V_5O_{13} \cdot 1.3H_2O$  cathode along with acetylene black enhanced zinc foil (AB-Zn) has a high discharge capacity of  $461 mAh g^{-1}$  at  $0.2 A g^{-1}$  (Figure 16e) and a capacity retention rate of 96.2% in 4000



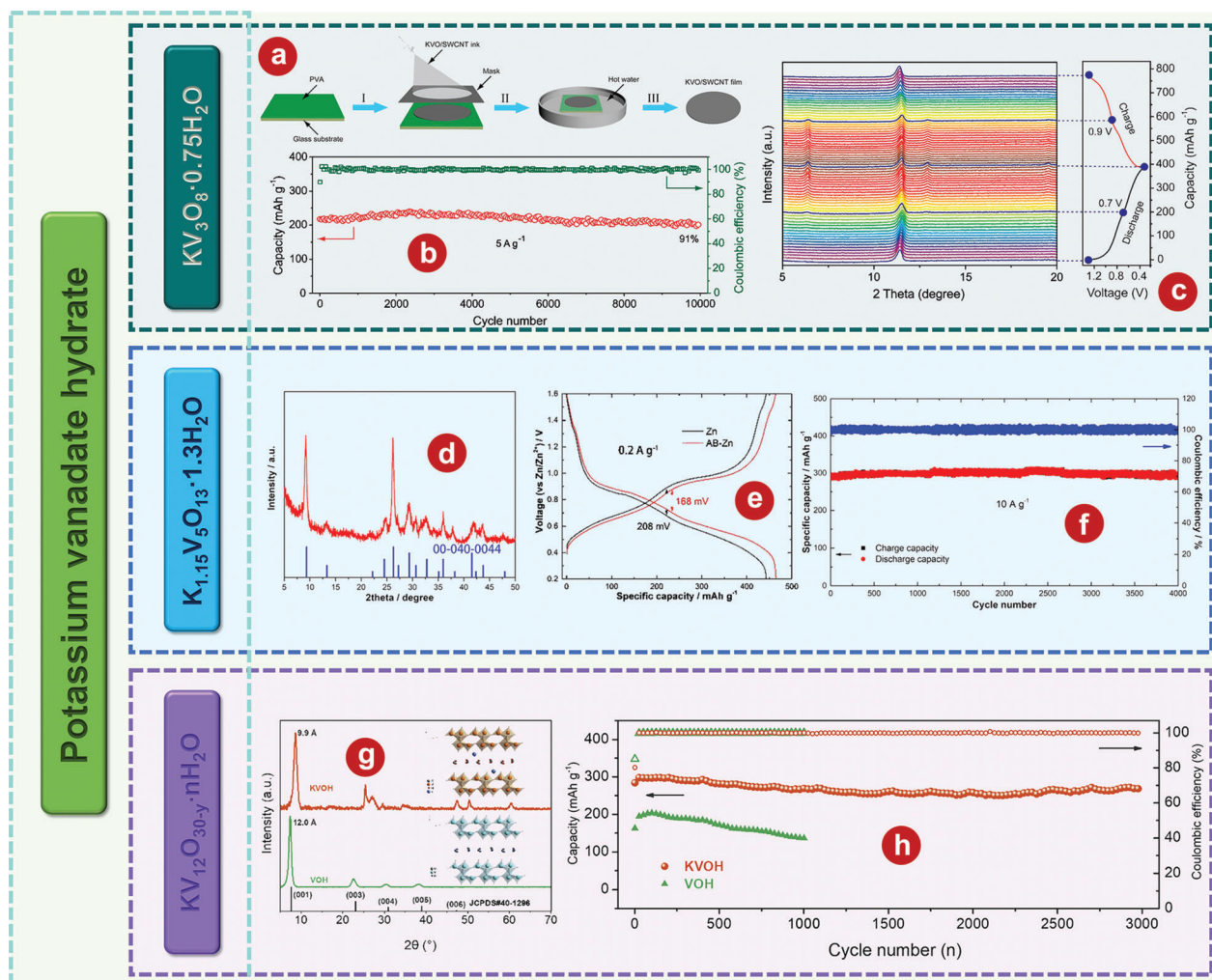


**Figure 16.** a) Schematic diagram of  $\text{KV}_3\text{O}_8 \cdot 0.75\text{H}_2\text{O}/\text{SWCNTs}$  films. b) Long-term cycle life at a  $5 \text{ A g}^{-1}$ . c) In situ XRD patterns of  $\text{KV}_3\text{O}_8 \cdot 0.75\text{H}_2\text{O}/\text{SWCNTs}$  electrode during (dis)charge process. d) XRD patterns of  $\text{K}_{1.15}\text{V}_5\text{O}_{13} \cdot 1.3\text{H}_2\text{O}$ . e) Typical charge-discharge profiles for the  $\text{Zn}/\text{K}_{1.15}\text{V}_5\text{O}_{13} \cdot 1.3\text{H}_2\text{O}$  and  $\text{AB-Zn}/\text{K}_{1.15}\text{V}_5\text{O}_{13} \cdot 1.3\text{H}_2\text{O}$  in  $3 \text{ M Zn}(\text{OTf})_2 \text{ AE}$  at  $0.2 \text{ A g}^{-1}$ . f) Cycling performance of  $\text{K}_{1.15}\text{V}_5\text{O}_{13} \cdot 1.3\text{H}_2\text{O}$  at  $10 \text{ A g}^{-1}$ . g) XRD patterns of samples (inset are possible schematic frameworks). h) Long-term cycle life of samples tested at  $5 \text{ A g}^{-1}$ . a–c) Reproduced with permission.<sup>[271]</sup> Copyright 2020, American Chemical Society. d–f) Reproduced with permission.<sup>[272]</sup> Copyright 2021, American Chemical Society. g, h) Reproduced with permission.<sup>[274]</sup> Copyright 2020, Elsevier.

cycles at  $10 \text{ A g}^{-1}$  (Figure 16f), which is expected to provide clues in the pursuit of energy storage devices with superior performance.

**$\text{KV}_{12}\text{O}_{30-y} \cdot n\text{H}_2\text{O}$ :** In the structure of  $\text{KV}_{12}\text{O}_{30-y} \cdot n\text{H}_2\text{O}$ , there are more low-price  $\text{V}^{4+}$  and more oxygen vacancies in the structure after the addition of  $\text{K}^+$ . This phenomenon can also be observed in the previously published insert of hydrated  $\text{Mn}^{2+}$  into vanadate.<sup>[273]</sup> Tian et al.<sup>[274]</sup> prepared the structurally unique  $\text{KV}_{12}\text{O}_{30-y} \cdot n\text{H}_2\text{O}$  by intercalating  $\text{K}^+$  into  $\text{V}_2\text{O}_5 \cdot n\text{H}_2\text{O}$  via a structural engineering method. As shown in Figure 16g,  $\text{V}_2\text{O}_5 \cdot n\text{H}_2\text{O}$  exhibits a typical bilayer structure similar to  $\text{V}_2\text{O}_5 \cdot 1.6\text{H}_2\text{O}$ . For  $\text{KV}_{12}\text{O}_{30-y} \cdot n\text{H}_2\text{O}$ , it exhibits a unique XRD pattern, which is different from the  $\text{K}^+$  integration structure reported in the literature.<sup>[269,275]</sup>  $\text{KV}_{12}\text{O}_{30-y} \cdot n\text{H}_2\text{O}$  cathode delivers superior long-term cycle life over 3000 cycles with 92% capacity retention at  $5 \text{ A g}^{-1}$  (Figure 16h), high energy density of  $308 \text{ Wh kg}^{-1}$ , and power density of  $7502 \text{ W kg}^{-1}$ , and enhanced energy efficiency.

## 4.2. Multivalent Alkali Metal Cations

### 4.2.1. The Co-Intercalation of $\text{Mg}^{2+}$ and $\text{H}_2\text{O}$

**$\text{Mg}_{0.19}\text{V}_2\text{O}_5 \cdot 0.99\text{H}_2\text{O}$ :** The  $\text{H}_2\text{O}$  molecules and  $\text{Mg}^{2+}$  between the layers can act as pillars to stabilize the  $\text{V}_2\text{O}_5$  layer during the (dis)charging process.<sup>[276–278]</sup> In addition, interlayer  $\text{H}_2\text{O}$  molecules can expand the layer spacing and weaken strong electrostatic interactions, thus providing the benefit of the “lubrication effect” revealed by Mai and Liang et al.<sup>[61,279]</sup> Currently, the mass loading of active substances used in almost all scientific reports is usually much lower than commercial levels.<sup>[280–283]</sup> To solve this problem, Zhou and colleagues<sup>[284]</sup> prepared a commercial-level  $\text{Mg}_{0.19}\text{V}_2\text{O}_5 \cdot 0.99\text{H}_2\text{O}$  cathode with a mass load of  $10 \text{ mg cm}^{-2}$ , which has a large interlayer spacing of  $13.4 \text{ \AA}$ , and applied it to AZIBs (Figure 17a). In addition, the  $\text{Mg}_{0.19}\text{V}_2\text{O}_5 \cdot 0.99\text{H}_2\text{O}$  cathode is assembled in combination with



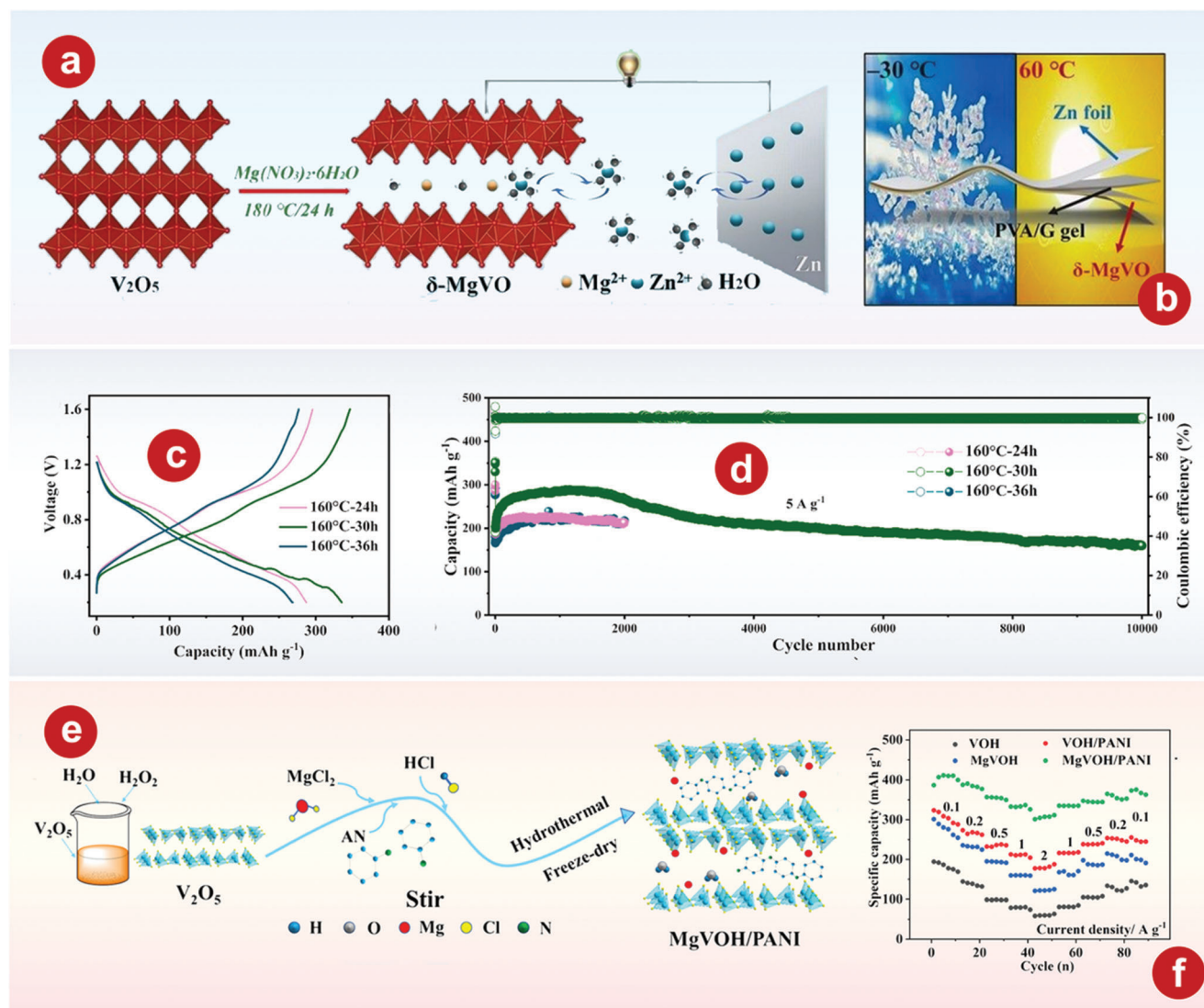


**Figure 17.** a) Schematic diagram showing the formation process of  $\text{Mg}_{0.19}\text{V}_2\text{O}_5 \cdot 0.99\text{H}_2\text{O}$  and the working principal of Zn// $\text{Mg}_{0.19}\text{V}_2\text{O}_5 \cdot 0.99\text{H}_2\text{O}$  battery. b) Schematic diagram of the thin-film PVA/G Zn// $\text{Mg}_{0.19}\text{V}_2\text{O}_5 \cdot 0.99\text{H}_2\text{O}$  battery. c) Cycling performance at  $0.1\text{ A g}^{-1}$ . d) Long cycling performance at  $5\text{ A g}^{-1}$ . e) Schematic diagram of the synthesis of ternary material  $\text{MgVOH/PANI}$ . f) Rate capability of samples. a, b): Reproduced with permission.<sup>[284]</sup> Copyright 2020, The Royal Society of Chemistry. c, d) Reproduced with permission.<sup>[289]</sup> Copyright 2022, Elsevier. e, f) Reproduced with permission.<sup>[290]</sup> Copyright 2022, The Royal Society of Chemistry.

the PVA/glycerol gel electrolyte to form a quasi-solid battery (Figure 17b), which shows high ionic conductivity over a wide temperature range, such as  $10.7\text{ mS cm}^{-1}$  at  $-30^\circ\text{C}$ , and good compatibility with the zinc foil anode. Because of this, quasi solid-state battery shows excellent performance at  $-30$  to  $60^\circ\text{C}$ .

**$\text{Mg}_{0.2}\text{V}_2\text{O}_5 \cdot n\text{H}_2\text{O}$ :** MXenes ( $\text{M}_{n+1}\text{X}_n\text{T}_x$ ,  $n = 1, 2, 3$ ), where M is transition metal (e.g., Ti, Nb, V, Mo, etc.), X is N and/or C,  $\text{T}_x$  is surface group (e.g.,  $-\text{F}$ ,  $-\text{OH}$ ,  $=\text{O}$ , etc.), as 2D layered inorganic compounds with good conductivity, excellent hydrophilicity, nested structure, high specific surface area, and abundant active sites, have become hot materials in the field of electrochemical storage.<sup>[285–288]</sup> In addition, metal vanadate can be prepared by derivation of MXenes, followed by intercalation of metal ions. Guan et al.<sup>[289]</sup> designed and prepared  $\text{V}_2\text{O}_5 \cdot n\text{H}_2\text{O}$  nanoribbons with  $\text{Mg}^{2+}$  pre-intercalation ( $\text{Mg}_{0.2}\text{V}_2\text{O}_5 \cdot n\text{H}_2\text{O}$ ) derived from con-

ductive  $\text{V}_4\text{C}_3$  MXenes as the cathode of AZIBs, exhibiting a high reversible capacity of  $346\text{ mAh g}^{-1}$  at  $0.1\text{ A g}^{-1}$  (Figure 17c) and a capacity retention rate of 83.7% after 10 000 cycles at  $5\text{ A g}^{-1}$  (Figure 17d).

#### 4.2.2. The Co-Intercalation of $\text{Mg}^{2+}$ and Polyaniline in Hydrated $\text{V}_2\text{O}_5$

**$\text{Mg}_{0.1}\text{V}_2\text{O}_5 \cdot n\text{H}_2\text{O}/\text{PANI}$ :** Feng et al.<sup>[290]</sup> used the “co-intercalation mechanism” to simultaneously insert  $\text{Mg}^{2+}$  and PANI into the hydrated  $\text{V}_2\text{O}_5$  layer by a one-step hydrothermal method (Figure 17e).  $\text{Mg}^{2+}$  and PANI can expand the hydrated  $\text{V}_2\text{O}_5$  layer spacing to  $14.2\text{ \AA}$  like pillars, which greatly reduces the coulomb interaction between  $\text{Zn}^{2+}$  and  $\text{V}_2\text{O}_5$ , thus speeding

up the diffusion rate of  $\text{Zn}^{2+}$  and enhancing the storage performance of  $\text{Zn}^{2+}$ .<sup>[88,291]</sup> In addition, PANI can also store  $\text{Zn}^{2+}$  as a guest, and  $\text{Mg}^{2+}$  can improve the conductivity and stability of the hydrated  $\text{V}_2\text{O}_5$ . The specific capacity of  $\text{Mg}_{0.1}\text{V}_2\text{O}_5 \cdot n\text{H}_2\text{O}/\text{PANI}$  can reach  $412 \text{ mAh g}^{-1}$  at  $0.1 \text{ A g}^{-1}$  (Figure 17f), and the capacity retention rate can reach 98% after 1000 cycles.

#### 4.2.3. The Co-Intercalation of $\text{Ca}^{2+}$ and $\text{H}_2\text{O}$

$\text{Ca}_{0.04}\text{V}_2\text{O}_5 \cdot 1.74\text{H}_2\text{O}$ :  $\text{Ca}_{0.04}\text{V}_2\text{O}_5 \cdot 1.74\text{H}_2\text{O}$  has a similar structure to hydrated vanadium pentoxide. The lattice spacing of (001) plane for  $\text{Ca}_{0.04}\text{V}_2\text{O}_5 \cdot 1.74\text{H}_2\text{O}$  is  $12.48 \text{ \AA}$ , which is larger than the  $\text{V}_2\text{O}_5 \cdot n\text{H}_2\text{O}$  and the previously reported hydrated vanadium pentoxide ( $11.5 \text{ \AA}$ ).<sup>[292]</sup> indicating that the insertion of a small amount of  $\text{Ca}^{2+}$  plays a key role in widening the lattice spacing.<sup>[293]</sup> Du et al.<sup>[294]</sup> prepared a small amount of  $\text{Ca}^{2+}$  pre-intercalated  $\text{V}_2\text{O}_5$  by hydrothermal method. The stable chemical bond energy between Ca and O atoms in  $\text{VO}_x$  is greater than that of  $\text{Zn}-\text{O}$ ,<sup>[295]</sup> which provides a fixed effect for the robust  $\text{Ca}_{0.04}\text{V}_2\text{O}_5 \cdot 1.74\text{H}_2\text{O}$  structure, enabling reversible  $\text{Zn}^{2+}$  intercalation and fast ion transport. The  $\text{Ca}_{0.04}\text{V}_2\text{O}_5 \cdot 1.74\text{H}_2\text{O}$  cathode has a high specific capacity of  $400 \text{ mAh g}^{-1}$  at  $0.05 \text{ A g}^{-1}$  and a capacity retention rate of 100% at  $10 \text{ A g}^{-1}$  after 3000 cycles.

$\text{CaV}_6\text{O}_{16} \cdot 3\text{H}_2\text{O}$ :  $\text{CaV}_6\text{O}_{16} \cdot 3\text{H}_2\text{O}$  is a typical vanadium-bronze mineral, in which  $\text{Ca}^{2+}$  is in the interlayer space, coordinated by oxygens from the two vanadium slabs, facing each other, and by oxygens belonging to bound water molecules. Thus, the  $\text{Ca}^{2+}$  may act as pillaring agents to stabilize the structure of vanadium oxide, just as alkali metal ions do. Compared with the alkali vanadium bronze with molecular formulas  $\text{M}_x\text{V}_2\text{O}_5$ ,  $\text{MV}_3\text{O}_8$ ,  $\text{MV}_6\text{O}_{15}$ , and  $\text{M}_2\text{V}_6\text{O}_{16}$  ( $\text{M} = \text{Li}, \text{Na}, \text{or K}$ ),  $\text{CaV}_6\text{O}_{16} \cdot 3\text{H}_2\text{O}$  has a larger interlayer distance, which is conducive to shuttle ion intercalation. Liu and co-workers<sup>[296]</sup> prepared  $\text{CaV}_6\text{O}_{16} \cdot 3\text{H}_2\text{O}$  through a highly efficient and fast microwave reaction, and used it as a cathode material for AZIBs. Liu and co-workers<sup>[296]</sup> also demonstrated the reversibility of the process of  $\text{Zn}^{2+}$  (de)intercalation and the high structural stability of  $\text{CaV}_6\text{O}_{16} \cdot 3\text{H}_2\text{O}$  by ex situ XRD measurement.

#### 4.2.4. The Co-Intercalation of $\text{Al}^{3+}$ and $\text{H}_2\text{O}$

$\text{H}_{11}\text{Al}_2\text{V}_6\text{O}_{23.2}$ : It is possible to find V-based cathode materials with zero-strain properties, crystal plane “soft bond” ion channels with large interlayer spacing, and stable structures to improve easy  $\text{Zn}^{2+}$  (de)intercalation. Wei et al.<sup>[47]</sup> prepared  $\text{H}_{11}\text{Al}_2\text{V}_6\text{O}_{23.2}$  microspheres with large interlayer distances as cathode materials for AZIBs. The lattice structure remains well maintained even after 1000 cycles, and  $\text{H}_{11}\text{Al}_2\text{V}_6\text{O}_{23.2}$  cathode has excellent reversibility, maintaining 88.6% capacity after 7000 cycles.

### 4.3. Transition Metal Cations

#### 4.3.1. The Intercalation of $\text{Ag}^+$

$\beta\text{-AgVO}_3$ : The monoclinic channel-structured  $\beta\text{-AgVO}_3$  consists of an infinite number of  $[\text{V}_4\text{O}_{12}]_n$  double chains of edge-shared  $\text{VO}_6$  octahedron, where the chains are zigzag in shape and

double.<sup>[297,298]</sup> In addition, the  $[\text{V}_4\text{O}_{12}]_n$  double chains are composed of  $\text{AgO}_6$  octahedrons and tightly connected by  $\text{Ag}_2\text{O}_5$  and  $\text{Ag}_3\text{O}_5$  square pyramids to construct the robust open 3D network required for AZIBs. Liu et al.<sup>[299]</sup> prepared an  $\beta\text{-AgVO}_3$  with excellent performance for the cathode of AZIBs for the first time and demonstrated the basic storage mechanism of  $\text{Zn}^{2+}$  in detail. As can be seen from the XRD pattern in Figure 18a, all the diffraction peaks belong to  $\beta\text{-AgVO}_3$  monoclinic phase with channel structure, indicating high purity of the product. The in situ generation of  $\text{Ag}^0$  and residual  $\text{Ag}^+$  and structural water in the frame provide high electronic and ionic conductivity, which enhances the (de)intercalation kinetics of  $\text{Zn}^{2+}$  in the layered phase. The  $\beta\text{-AgVO}_3$  cathode can provide an excellent rate performance of  $103 \text{ mAh g}^{-1}$  at  $5 \text{ A g}^{-1}$  (Figure 18b) and superior cycle stability of  $95 \text{ mAh g}^{-1}$  at  $2 \text{ A g}^{-1}$  after 1000 cycles (Figure 18c). Liu et al.<sup>[299]</sup> also proved the energy storage mechanism of  $\beta\text{-AgVO}_3$ , as shown in Figure 18d.

$\text{Ag}_2\text{V}_4\text{O}_{11}$ : The crystal structure of  $\text{Ag}_2\text{V}_4\text{O}_{11}$  consists of  $[\text{V}_4\text{O}_{16}]$  units made of  $\text{VO}_6$  distorted octahedrons sharing their apexes, which build infinite  $[\text{V}_4\text{O}_{12}]_n$  quadruple strings. These quadruple strings are linked by corner-shared oxygen to provide continuous  $[\text{V}_4\text{O}_{11}]_n$  layers separated by Ag atoms.<sup>[300–302]</sup> Li and colleagues<sup>[303]</sup> prepared a layered  $\text{Ag}_2\text{V}_4\text{O}_{11}$  via a facile hydrothermal method and used it as a novel cathode material for AZIBs. The XRD pattern can be labeled monoclinic  $\text{Ag}_2\text{V}_4\text{O}_{11}$  (Figure 18e). Ex situ XRD patterns of first two cycles within the working potential window of  $0.4\text{--}1.7 \text{ V}$  are shown in Figure 18f to study the electrochemical mechanism. For electrochemical performance of the  $\text{Ag}_2\text{V}_4\text{O}_{11}$  cathode, as shown in Figure 18g, when the scanning rate is from  $0.1$  to  $0.5 \text{ mV s}^{-1}$ , the CVs shape doesn't change significantly, showing that its stability is good. In addition, the  $\text{Ag}_2\text{V}_4\text{O}_{11}$  cathode also delivers a specific capacity of  $213 \text{ mAh g}^{-1}$  (Figure 18h) and superior cycling performance with a capacity retention rate of 93% at  $5 \text{ A g}^{-1}$  after 6000 cycles (Figure 18i).

#### 4.3.2. The Intercalation of $\text{Zn}^{2+}$

$\text{ZnV}_2\text{O}_4$ : The crystal structure of  $\text{ZnV}_2\text{O}_4$  belongs to the FCC-type crystal structure with  $\text{Fd}\bar{3}m$  symmetric groups. The  $\text{ZnO}_4$  tetrahedron and  $\text{VO}_6$  octahedron form the crystal structure of  $\text{ZnV}_2\text{O}_4$ . Zn atoms are located at the (8a) tetrahedral position, while V atoms are located at the 16d tetrahedral position, forming a network of tetrahedral structures with shared angles. In addition, the O atoms are located at 32e.<sup>[304,305]</sup> Liu et al.<sup>[306]</sup> studied a typical spinel  $\text{ZnV}_2\text{O}_4$  as an AZIB cathode and observed an electroactivation reaction during the initial electrochemical cycle. The electroactivation reaction, which enhances surface electrochemical reactions through adaptive adjustment of lattice structures, is analyzed by in situ XRD, ex situ atomic pair distribution function (Figure 19a), and various electrochemical measurements. The  $\text{ZnV}_2\text{O}_4$  cathode delivers a high reversible capacity of  $312 \text{ mAh g}^{-1}$  and superior cycling performance with a capacity retention rate of  $206 \text{ mAh g}^{-1}$  after 1000 cycles at  $10 \text{ C}$  after electroactivation.

$\text{Zn}_2\text{V}_2\text{O}_7$ :  $\text{Zn}_2\text{V}_2\text{O}_7$  delivers polymorphism crystallizing in  $\alpha$ - ( $\text{C2/c}$  space group) and  $\beta$ - ( $\text{C2/m}$  space group) forms.<sup>[307,308]</sup> Among them,  $\alpha\text{-Zn}_2\text{V}_2\text{O}_7$  is a promising yellow phosphor and an

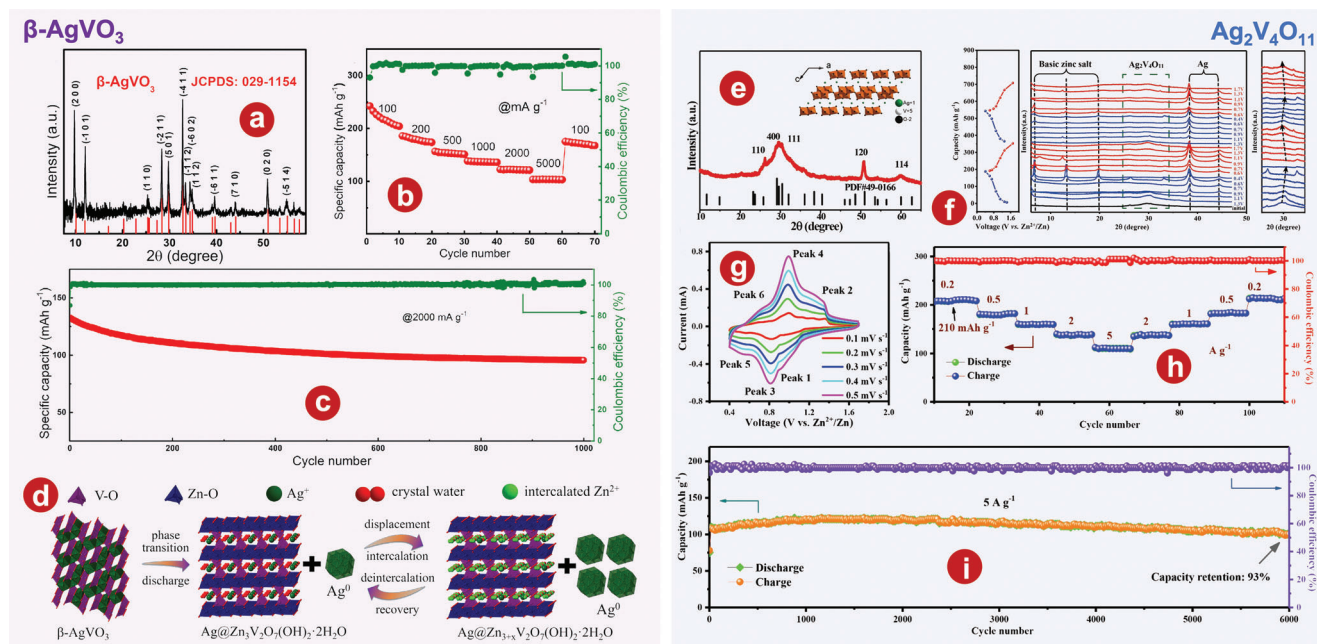


**Figure 18.** a) XRD pattern of  $\beta$ - $\text{AgVO}_3$ . b) Rate performance of  $\beta$ - $\text{AgVO}_3$ . c) The long-term cycle stability at  $2000 \text{ mA g}^{-1}$  of the electrode. d) Schematic illustration of  $\text{Zn}^{2+}$  energy storage mechanism of the  $\beta$ - $\text{AgVO}_3$ . e) XRD patterns and crystal structures of  $\text{Ag}_2\text{V}_4\text{O}_{11}$ . f) The ex situ XRD patterns of different voltage states collected at  $50 \text{ mA g}^{-1}$ . g) CV curves of  $\text{Ag}_2\text{V}_4\text{O}_{11}$  at different scan rates. h) Rate performance of  $\text{Ag}_2\text{V}_4\text{O}_{11}$ . i) Long-term cycling performance of  $\text{Ag}_2\text{V}_4\text{O}_{11}$  at  $5 \text{ A g}^{-1}$ . a–d) Reproduced with permission.<sup>[299]</sup> Copyright 2019, Elsevier. e–i) Reproduced with permission.<sup>[303]</sup> Copyright 2019, Wiley-VCH.

important component of transition-metal vanadates with layered crystal structure.<sup>[309]</sup> Sambandam and colleagues<sup>[310]</sup> developed an AZIBs using 1D  $\text{Zn}_2\text{V}_2\text{O}_7$  nanowires, prepared by a simple one-step hydrothermal method, as the potential (de)intercalation host. As shown in Figure 19b, the prepared powders are crystallographically characterized by powder XRD. The electrochemical process of multi-step  $\text{Zn}^{2+}$  (de)intercalation caused by the reduction/oxidation of vanadium in the underlying  $\alpha$ - $\text{Zn}_2\text{V}_2\text{O}_7$  is also explained by CV curves (Figure 19c).<sup>[311–313]</sup> In addition, the  $\alpha$ - $\text{Zn}_2\text{V}_2\text{O}_7$  cathode shows a good cycling performance with a capacity retention rate of 85% after 1000 cycles at an ultra-high current drain of  $4 \text{ A g}^{-1}$  (Figure 19d).

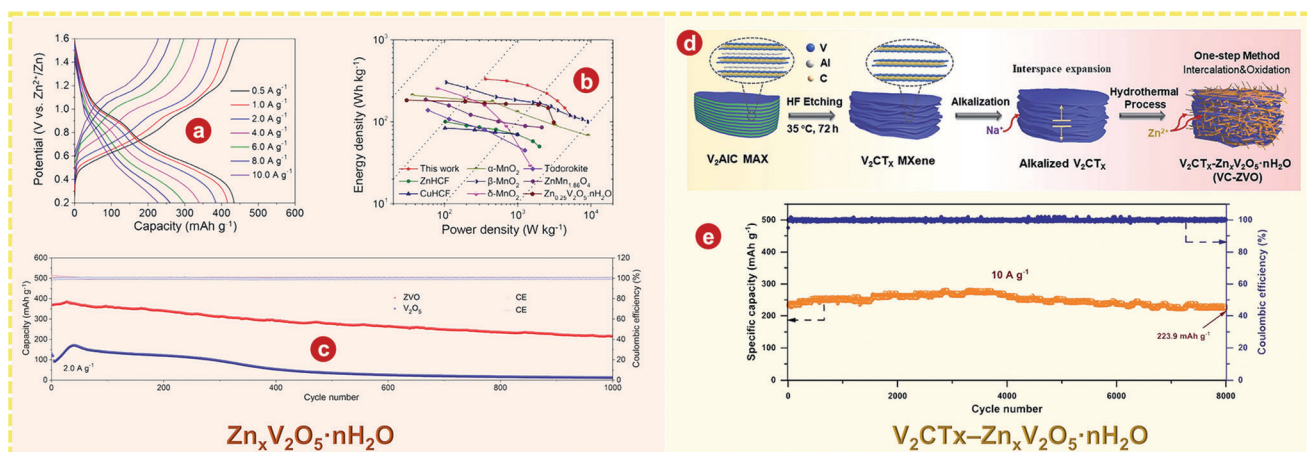
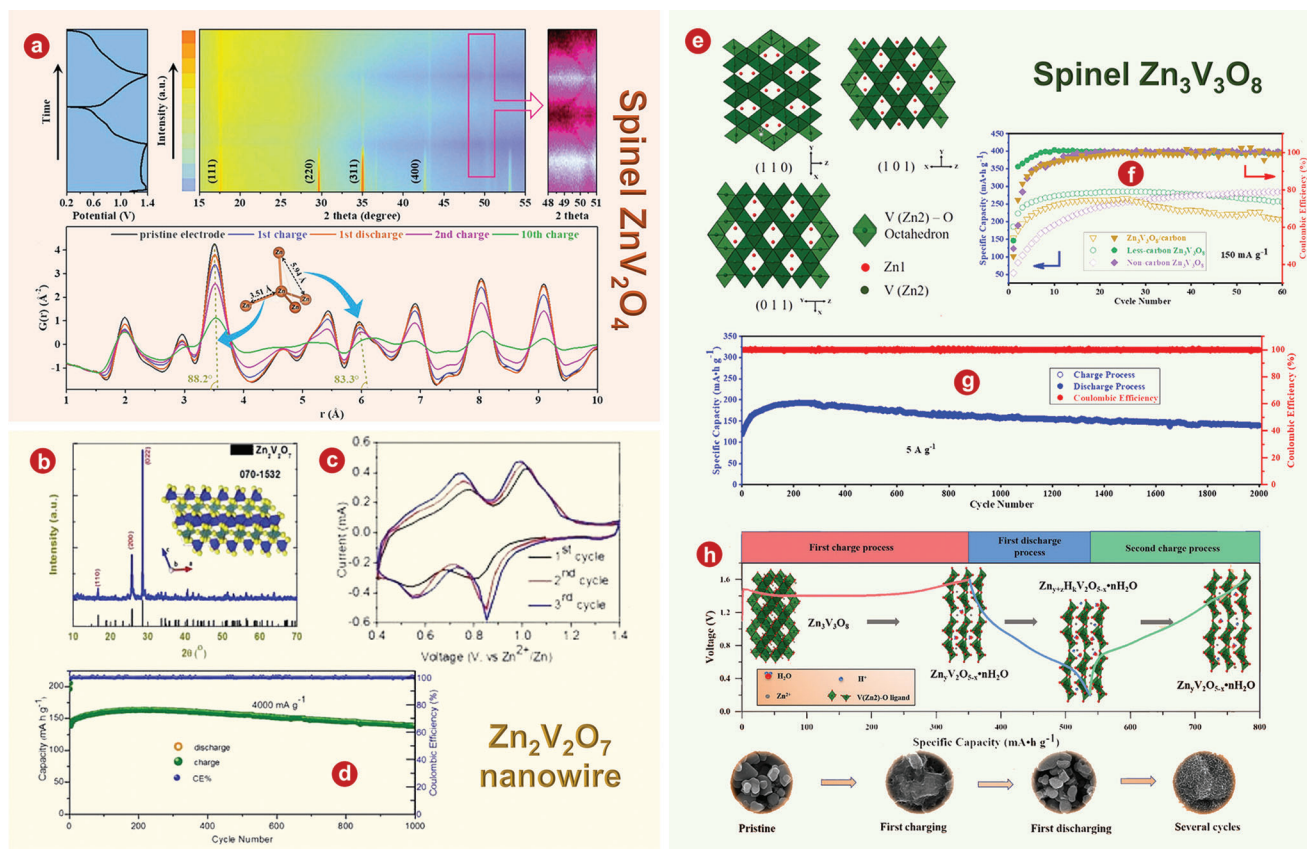
**$\text{Zn}_3\text{V}_3\text{O}_8$ :** According to the structural parameters obtained by Rietveld refinement, Figure 19e is the crystal structure diagram of  $\text{Zn}_3\text{V}_3\text{O}_8$ . Apparently, this structure has a 3D framework made of  $\text{V}(\text{Zn}_2)\text{O}_6$  octahedron, and  $\text{Zn}^{2+}$  ions are distributed in the tunnels along the directions [110], [101], and [011]. Therefore, spinel  $\text{Zn}_3\text{V}_3\text{O}_8$  is conducive to the transport of  $\text{Zn}^{2+}$  along the tunnels, but the improper deintercalation of  $\text{Zn}^{2+}$  during the charging process, especially the deintercalation of  $\text{Zn}^{2+}$  from the octahedral position, may lead to the collapse of spinel  $\text{Zn}_3\text{V}_3\text{O}_8$  structure. Spinel  $\text{Zn}_3\text{V}_3\text{O}_8$ , as the first vanadium-based compounds, was used as a high-capacity cathode for AZIBs by Wu et al.<sup>[314]</sup> All the three samples exhibit electroactivation in the incipient cycles, which is a common phenomenon related to the phase transition of cathode materials in AZIBs. Both less-carbon and non-carbon  $\text{Zn}_3\text{V}_3\text{O}_8$  show superior cycling performance, which delivers a maximal discharge capacity of  $285 \text{ mAh g}^{-1}$  (Figure 19f). In addition, the less-carbon  $\text{Zn}_3\text{V}_3\text{O}_8$  delivers a capacity retention rate of 72.6% after 2000 cycles at  $5 \text{ A g}^{-1}$  (Figure 19g).

Based on the above analysis and discussion of various representations, Wu et al.<sup>[314]</sup> also show the structure and morphology evolution of the  $\text{Zn}_3\text{V}_3\text{O}_8$  cathode in Figure 19h.

#### 4.3.3. The Co-Intercalation of $\text{Zn}^{2+}$ and $\text{H}_2\text{O}$

**$\text{Zn}_x\text{V}_2\text{O}_5 \cdot n\text{H}_2\text{O}$ :** The pre-intercalated  $\text{Zn}^{2+}$  and  $\text{H}_2\text{O}$  can also be used as “pillars” to stabilize the cathode and provide high  $\text{Zn}^{2+}$  storage, improving considerable battery performance. Hu and colleagues<sup>[161]</sup> developed a method for the synthesis of  $\text{Zn}_x\text{V}_2\text{O}_5 \cdot n\text{H}_2\text{O}$  from vanadium trioxide metal by electrochemical intercalation phase transition in aqueous solution. The  $\text{Zn}_x\text{V}_2\text{O}_5 \cdot n\text{H}_2\text{O}$  nanosheets cathode delivers a high reversible capacity of  $435 \text{ mAh g}^{-1}$  at  $0.5 \text{ A g}^{-1}$  (Figure 20a), high energy and power densities of  $331 \text{ Wh kg}^{-1}$  at  $361 \text{ W kg}^{-1}$  (Figure 20b), as well as superior cycle stability (Figure 20c). The addition of highly conductive substrates, such as carbon-based materials,<sup>[315]</sup> conductive polymers,<sup>[316]</sup> and MXenes,<sup>[230]</sup> can indeed enhance the  $\text{Zn}^{2+}$  storage capacity of vanadium-based cathodes at higher rates. However, such preparation of such complexes is complicated and uncertain, and cannot maintain structural stability during cycling. In order to solve these problems, Zhu and colleagues<sup>[317]</sup> used highly conductive  $\text{V}_2\text{CT}_x$  MXene to fabricate  $\text{Zn}_x\text{V}_2\text{O}_5 \cdot n\text{H}_2\text{O}$  nanoribbon ( $\text{V}_2\text{CT}_x\text{-Zn}_x\text{V}_2\text{O}_5 \cdot n\text{H}_2\text{O}$ ) with uniform size by the simultaneous action of ion intercalation and oxidation (Figure 20d), and used it as cathode material for AZIBs. Due to the pre-intercalation of  $\text{Zn}^{2+}$  and the ubiquitous interfaces between  $\text{Zn}_x\text{V}_2\text{O}_5 \cdot n\text{H}_2\text{O}$  and the conductive network including the remaining  $\text{V}_2\text{CT}_x$  and carbon, the charge redistribution in





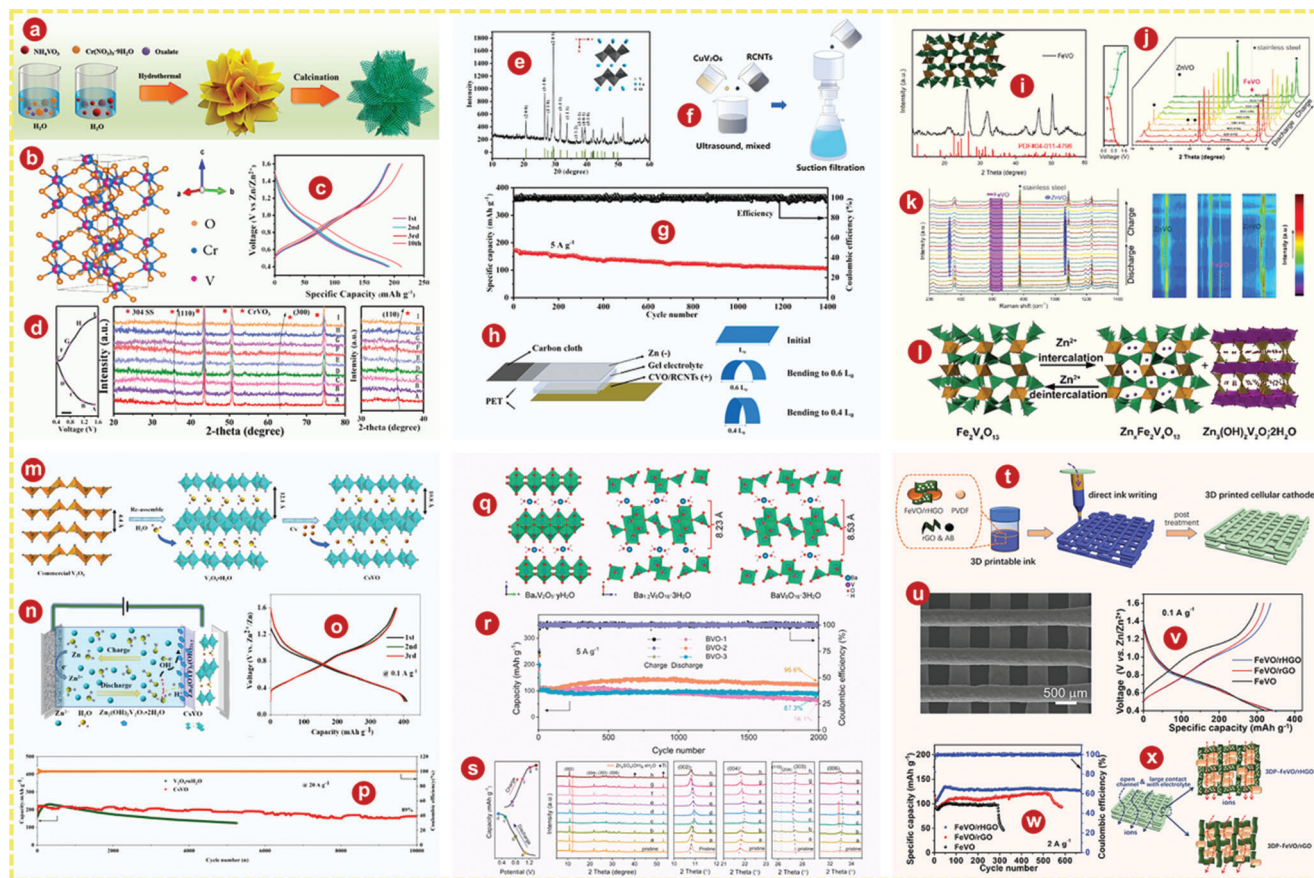


**Figure 21.** a) Schematic illustration of the fabrication urchin-like porous  $\text{CrVO}_3$ . b) Crystal structure of pr-CVO-1. c) Charge-discharge profiles of pr-CVO-1 at  $0.5 \text{ A g}^{-1}$ . d) The first charge-discharge of pr-CVO-1, XRD patterns of the pr-CVO-1 cathodes at various GCD cycles, and magnified XRD patterns. e) XRD pattern of  $\text{CuV}_2\text{O}_6$ -18. f) Schematic illustration of vacuum filtration. g) The long-term cycling performance of  $\text{CuV}_2\text{O}_6$ -18/RCNTs at the current densities of  $2 \text{ A g}^{-1}$ . h) Schematic diagram of flexible gel  $\text{Zn}/\text{CuV}_2\text{O}_6$ -18/RCNTs battery (reaction time 18 h). i) XRD pattern of  $\text{Fe}_2\text{V}_4\text{O}_{13}$ . j) Charge/discharge profiles for the initial cycle at  $0.2 \text{ A g}^{-1}$  and corresponding ex situ XRD patterns of  $\text{Fe}_2\text{V}_4\text{O}_{13}$  cathode during discharge-charge process. k) In situ Raman curves of  $\text{Fe}_2\text{V}_4\text{O}_{13}$  cathode during discharge-charge process. l) Schematic diagram of the (de)intercalation process of  $\text{Zn}^{2+}$  in  $\text{Fe}_2\text{V}_4\text{O}_{13}$  during cycling. m) Schematic diagram of fabrication process for  $\text{Cs}^+$  intercalated  $\text{V}_2\text{O}_5 \cdot n\text{H}_2\text{O}$ . n) Schematic diagram of  $\text{Zn}/\text{Cs}_{0.53}\text{V}_2\text{O}_5 \cdot 0.58\text{H}_2\text{O}$  battery. o) The discharge/charge profiles at  $0.1 \text{ A g}^{-1}$  of the first three cycles of  $\text{Cs}_{0.53}\text{V}_2\text{O}_5 \cdot 0.58\text{H}_2\text{O}$  cathode. p) The long cycle performance of two cells at  $20 \text{ A g}^{-1}$ . q) The crystal structure of  $\text{Ba}_{0.5}\text{V}_2\text{O}_5 \cdot n\text{H}_2\text{O}$ ,  $\text{Ba}_{1.2}\text{V}_6\text{O}_{16} \cdot 3\text{H}_2\text{O}$ , and  $\text{BaV}_6\text{O}_{16} \cdot 3\text{H}_2\text{O}$ . r) Cycling performance of three barium vanadates at  $5 \text{ A g}^{-1}$ . s) Charge/discharge curve at the selected states of the second cycle at  $200 \text{ mA g}^{-1}$  for the  $\text{Ba}_{1.2}\text{V}_6\text{O}_{16} \cdot 3\text{H}_2\text{O}$  cathode. Sampling points for XRD and FTIR characterization were marked with the corresponding colored dots and the corresponding magnified XRD patterns of different peaks for the  $\text{Ba}_{1.2}\text{V}_6\text{O}_{16} \cdot 3\text{H}_2\text{O}$  cathode. t) Schematic of direct ink writing-based fabrication of cellular  $\text{Fe}_5\text{V}_{15}\text{O}_{39}(\text{OH})_9 \cdot 9\text{H}_2\text{O}/\text{rHGO}$  cathodes for AZIBs. u) Top-view of cellular  $\text{Fe}_5\text{V}_{15}\text{O}_{39}(\text{OH})_9 \cdot 9\text{H}_2\text{O}/\text{rHGO}$  inks. v) GCD profiles of 3D Printed  $\text{Fe}_5\text{V}_{15}\text{O}_{39}(\text{OH})_9 \cdot 9\text{H}_2\text{O}/\text{rHGO}$  cathodes at different current densities. w) Long-term cycling performance at a current density of  $2 \text{ A g}^{-1}$ . x) Schematic of ionic transport for 3D printed  $\text{Fe}_5\text{V}_{15}\text{O}_{39}(\text{OH})_9 \cdot 9\text{H}_2\text{O}/\text{rHGO}$  and  $\text{Fe}_5\text{V}_{15}\text{O}_{39}(\text{OH})_9 \cdot 9\text{H}_2\text{O}/\text{rGO}$  electrodes. a–d) Reproduced with permission.<sup>[318]</sup> Copyright 2021, Elsevier. e–h) Reproduced with permission.<sup>[319]</sup> Copyright 2022, Elsevier. i–l) Reproduced with permission.<sup>[320]</sup> Copyright 2022, Elsevier. m–p) Reproduced with permission.<sup>[321]</sup> Copyright 2022, Elsevier. q–s) Reproduced with permission.<sup>[76]</sup> Copyright 2020, American Chemical Society. t–x) Reproduced with permission.<sup>[326]</sup> Copyright 2021, Wiley-VCH.

the active/conductive heterostructure leads to the weakening of electrostatic interactions, fast  $\text{Zn}^{2+}$  (de)intercalation, and structural stability, which makes the  $\text{V}_2\text{CT}_x\text{-Zn}_x\text{V}_2\text{O}_5 \cdot n\text{H}_2\text{O}$  cathode show an excellent cycling performance with a capacity retention of 96.4% more than 8000 cycles at  $10 \text{ A g}^{-1}$  (Figure 20e).

#### 4.3.4. The Intercalation of Other Transition Metal Cations

**$\text{CrVO}_3$ :**  $\text{CrVO}_3$  crystals have an open-channel structure and play a key role in the process of  $\text{Zn}^{2+}$  (de)intercalation. Bai et al.<sup>[318]</sup> prepared a novel  $\text{CrVO}_3$  with an urchin-like porous

structure via a simple hydrothermal followed by calcination (Figure 21a). The pr-CVO-1, pr-CVO-2, and pr-CVO-2 were synthesized according to different amounts of  $\text{Cr}(\text{NO}_3)_3 \cdot 9\text{H}_2\text{O}$  added. The crystal structure of pr-CVO-1 is shown in Figure 21b. The pr-CVO-1 shows the best electrochemical performance with a first discharge capacity of  $188.8 \text{ mAh g}^{-1}$  at  $0.5 \text{ A g}^{-1}$  (Figure 21c). At the same time, the formation mechanism and storage mechanism of  $\text{Zn}^{2+}$  were discussed by ex situ method (Figure 21d). The results show that porous  $\text{CrVO}_3$  is a promising cathode material for AZIBs, which provides a valuable design idea for significantly improving the electrochemical energy storage performance of porous vanadates.



**CuV<sub>2</sub>O<sub>6</sub>:** The crystal structure of CuV<sub>2</sub>O<sub>6</sub> consists of a double-layered, serrated VO<sub>6</sub> octahedral structure with split edges along the b axis. Song and colleagues<sup>[319]</sup> prepared CuV<sub>2</sub>O<sub>6</sub> nanobelts by hydrothermal method and free CuV<sub>2</sub>O<sub>6</sub>/reductively acidified CNTs (CuV<sub>2</sub>O<sub>6</sub>/RCNTs) composite films without binder by vacuum filtration method. The aqueous Zn//CuV<sub>2</sub>O<sub>6</sub>/RCNTs batteries have a good reversible capacity of 353 mA g<sup>-1</sup> at 0.1 A g<sup>-1</sup>, and a high reversible capacity of 174.7 mA g<sup>-1</sup> and a capacity retention of 61.5% after 1400 cycles of 5 A g<sup>-1</sup> (Figure 21g). Song et al.<sup>[319]</sup> also assemble flexible gel Zn//CuV<sub>2</sub>O<sub>6</sub>-18/RCNTs battery, as shown in Figure 21h.

**Fe<sub>2</sub>V<sub>4</sub>O<sub>13</sub>:** The tunnel structure of monoclinic Fe<sub>2</sub>V<sub>4</sub>O<sub>13</sub> consists of VO<sub>4</sub> tetrahedron and FeO<sub>6</sub> octahedron, which makes possible and favorable conditions for reversible (de)intercalation of Zn<sup>2+</sup>. Yang et al.<sup>[320]</sup> synthesized a Fe<sub>2</sub>V<sub>4</sub>O<sub>13</sub> with open structure as a cathode material for AZIBs. The structure of the prepared Fe<sub>2</sub>V<sub>4</sub>O<sub>13</sub> sample is confirmed by XRD characterization, and the diffraction peak has good directivity with the monoclinic Fe<sub>2</sub>V<sub>4</sub>O<sub>13</sub> phase (Figure 21i). Interestingly in this work, Yang et al.<sup>[320]</sup> demonstrated that two Zn<sup>2+</sup> storage mechanisms could be observed simultaneously with Fe<sub>2</sub>V<sub>4</sub>O<sub>13</sub> cathode through a combination of in situ and ex situ techniques (Figure 21j,k), namely, the classical (de)intercalated storage mechanism in the Fe<sub>2</sub>V<sub>4</sub>O<sub>13</sub> tunnel structure and the reversible phase transition from ferric vanadate to zinc vanadate (Figure 21l).

#### 4.3.5. The Intercalation of Other Transition Metal Cations and H<sub>2</sub>O

**Cs<sub>0.53</sub>V<sub>2</sub>O<sub>5</sub> 0.58H<sub>2</sub>O:** The pre-intercalated Cs<sup>+</sup> with large ionic radii preserves the appropriate interlayer distance for the diffusion of Zn<sup>2+</sup>, while the Cs<sup>+</sup> as the “pillar”, the strong Cs–O bond in the interlayer structure effectively maintains the stability of the structure, thus improving the rate capacity and cycling performance. Qi et al.<sup>[321]</sup> inserted Cs<sup>+</sup> into V<sub>2</sub>O<sub>5</sub> nH<sub>2</sub>O, resulting in enhanced layered structures that form strong CS–O bonds with native oxygen atoms to enhance interlayer interactions and avoid structural collapse (Figure 21m). The electrochemical performance of Cs<sub>0.53</sub>V<sub>2</sub>O<sub>5</sub> 0.58H<sub>2</sub>O for storing Zn<sup>2+</sup> was studied by assembling it with zinc foil anode and 3m Zn(CF<sub>3</sub>SO<sub>3</sub>)<sub>2</sub> electrolyte (Figure 21n). The Cs<sub>0.53</sub>V<sub>2</sub>O<sub>5</sub> 0.58H<sub>2</sub>O cathode delivers an improved specific capacity of 404.9 mAh<sup>-1</sup> at 0.1 A g<sup>-1</sup> (Figure 21o) and superior long-term cycle stability with a capacity retention of 89% after 10 000 cycles at 20 A g<sup>-1</sup> (Figure 21p).

**Ba<sub>1.2</sub>V<sub>6</sub>O<sub>16</sub> 3H<sub>2</sub>O:** Both BaV<sub>6</sub>O<sub>16</sub> 3H<sub>2</sub>O and Ba<sub>1.2</sub>V<sub>6</sub>O<sub>16</sub> 3H<sub>2</sub>O (typical V<sub>3</sub>O<sub>8</sub>-typed structure) are composed of V<sub>3</sub>O<sub>8</sub> polyhedral layers, which are stabilized by Barium hydrate ions, while the Ba<sub>1.2</sub>V<sub>6</sub>O<sub>16</sub> 3H<sub>2</sub>O is a typical V<sub>2</sub>O<sub>5</sub> structure due to the deviation of V–O band. The two layers of V<sub>2</sub>O<sub>5</sub> are bound by V–O bonds between layers, and the distributed barium hydrate ions are supported between layers (Figure 21q). Wang and colleagues<sup>[76]</sup> controlled the synthesis of three barium vanadate nanobelt cathodes by adjusting the amount of barium precursor. Thanks to the robust structure, the layered Ba<sub>1.2</sub>V<sub>6</sub>O<sub>16</sub> 3H<sub>2</sub>O nanobelt can effectively inhibit cathodic dissolution due to the rapid zinc ion kinetics, showing better rate capability and long-term cyclability than the other two (Figure 21r). In addition, these robust characteristics and water co-intercalation phenomena were revealed by electrochemical mechanism studies characterized by ex situ

XRD, FTIR (Figure 21s), and so on. Wang and colleagues<sup>[76]</sup> provides a feasible strategy for exploring or designing cathodic materials with robust structures to enhance the electrochemical performance of AZIBs.

**Fe<sub>5</sub>V<sub>15</sub>O<sub>39</sub>(OH)<sub>9</sub> 9H<sub>2</sub>O:** Recently, advanced 3D printing of cellular and hierarchical porous cathodes with high mass loading for AZIBs with excellent performance is explored,<sup>[322,323]</sup> which has unique manufacturing advantages of custom design, rapid prototyping, and structural optimization.<sup>[324,325]</sup> Ma et al.<sup>[326]</sup> composed a nanocomposite ink composed of Fe<sub>5</sub>V<sub>15</sub>O<sub>39</sub>(OH)<sub>9</sub> 9H<sub>2</sub>O nanosheet and reduced porous graphene oxide (rHGO) as the active material for the cell cathode, and extruded 3D printing inks with good rheological control properties onto various substrates to form independent nanocomposite cathodes (Figure 21t). The 3D printed-Fe<sub>5</sub>V<sub>15</sub>O<sub>39</sub>(OH)<sub>9</sub> 9H<sub>2</sub>O/rHGO and 3D printed-Fe<sub>5</sub>V<sub>15</sub>O<sub>39</sub>(OH)<sub>9</sub> 9H<sub>2</sub>O/rGO cathodes are composed of crisscrossing columns with a column diameter of about 390 μm from SEM image (Figure 21u). The 3D printed-Fe<sub>5</sub>V<sub>15</sub>O<sub>39</sub>(OH)<sub>9</sub> 9H<sub>2</sub>O/rHGO cathode with high mass loading over 10 mg cm<sup>-2</sup> shows a high specific capacity of 344.8 mAh g<sup>-1</sup> at 0.1 A g<sup>-1</sup> (Figure 21v) and delivers superior cycling stability over 650 cycles at 2 A g<sup>-1</sup> (Figure 21w). In addition, Figure 21x clearly illustrates that the 3D-printed cellular structure can provide open channels as well as large contacts with the electrolyte, leading to 3D migration of ions throughout the electrode structure.

#### 4.4. Ammonium Cations

##### 4.4.1. The Intercalation of NH<sub>4</sub><sup>+</sup>

**(NH<sub>4</sub>)<sub>0.38</sub>V<sub>2</sub>O<sub>5</sub>:** The monoclinic (NH<sub>4</sub>)<sub>0.38</sub>V<sub>2</sub>O<sub>5</sub> unit structure consists of distorted VO<sub>6</sub> octahedrons with shared edges, forming a stable bilayer structure (Figure 22a). The oxygen atoms in the octahedron have strong interactions with NH<sub>4</sub><sup>+</sup>. NH<sub>4</sub><sup>+</sup> tends to act as “pillar” cations to stabilize the structure and prevent volume changes in the interlayer spacing of guest ions during (de)intercalation.<sup>[327]</sup> In addition, compared with other vanadates such as sodium and potassium, ammonium cations exhibit relatively small molecular weight and density, and provide higher specific gravity and volumetric capacity.<sup>[328,329]</sup> Jiang et al.<sup>[330]</sup> revealed the spontaneous knitting behavior of 6.7 nm thin, flexible (NH<sub>4</sub>)<sub>0.38</sub>V<sub>2</sub>O<sub>5</sub> nanoribbons and the formation of binder-free paper ZIBs cathodes via hydrothermal pathways. Conductive CNTs have also been successfully embedded in paper to improve electronic conductivity and generate rich grids inside the paper. Due to the advantages of the binder-free design and porous structure, the (NH<sub>4</sub>)<sub>0.38</sub>V<sub>2</sub>O<sub>5</sub>/CNTs paper cathode has excellent long-term cycling performance, with an initial specific capacity of 465 mAh g<sup>-1</sup>, which still maintains an initial specific capacity of 89.3% after 500 cycles at A rate of 0.1 A g<sup>-1</sup> (Figure 22b). In addition, as shown in Figure 22c, the paper cathode has a specific energy of up to 343 Wh kg<sup>-1</sup>, which is significantly better than most powder cathodic ZIBs containing polymer binders.<sup>[331–335]</sup>

**(NH<sub>4</sub>)<sub>2</sub>V<sub>3</sub>O<sub>8</sub>:** (NH<sub>4</sub>)<sub>2</sub>V<sub>3</sub>O<sub>8</sub> is a typical layered structure consisting of V<sub>3</sub>O<sub>8</sub> layers and interstitial NH<sub>4</sub><sup>+</sup>. The VO layer consists of VO<sub>4</sub> tetrahedron (located in the plane of symmetry; The difference between the longest and shortest V–O bond is 0.08 Å) and VO<sub>5</sub> square pyramid, with NH<sub>4</sub><sup>+</sup> in the interlayer. The VO<sub>4</sub>



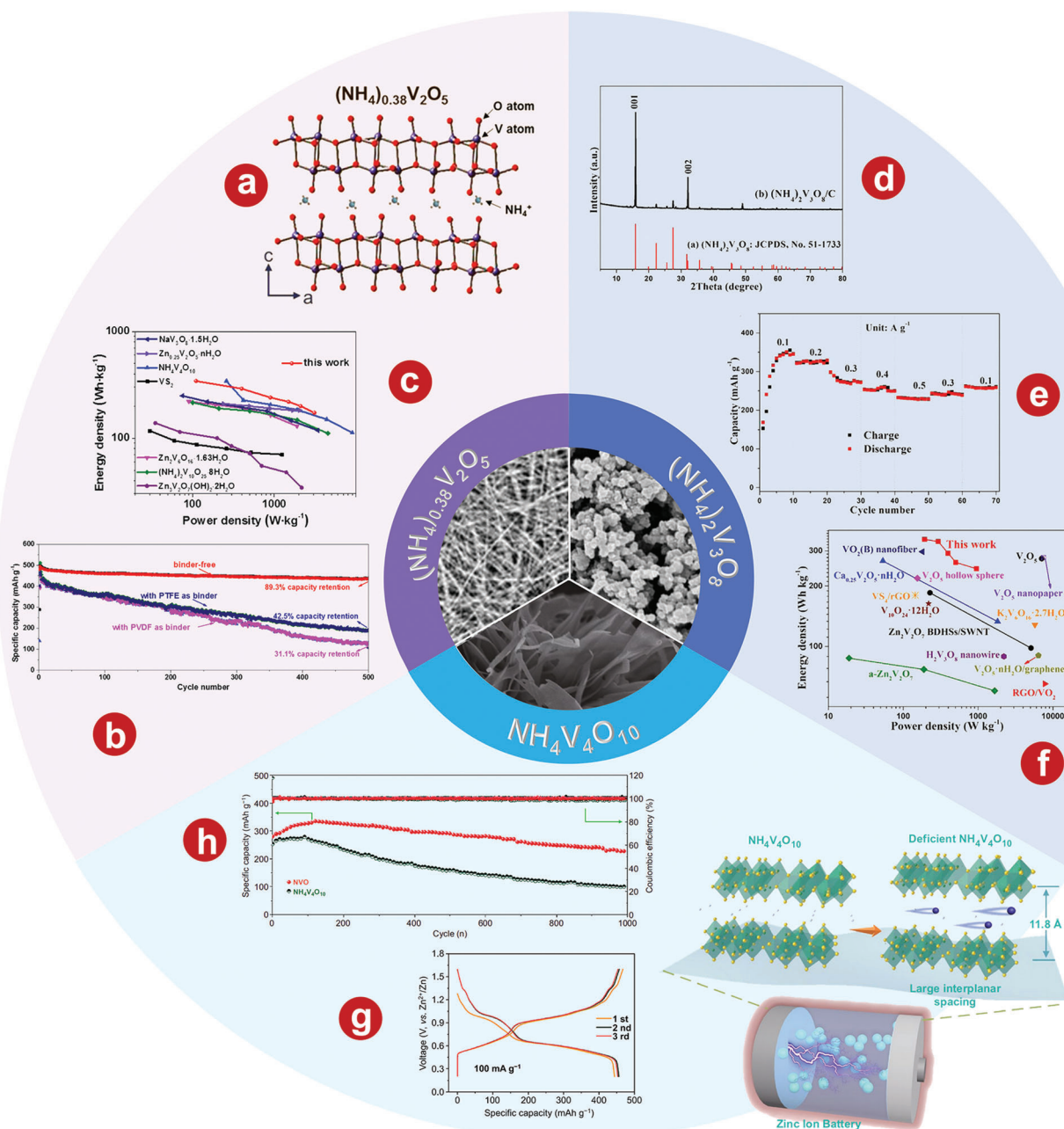


**Figure 22.** a) The atomic structure of layered  $(\text{NH}_4)_{0.38}\text{V}_2\text{O}_5$  crystal. b) The cycle performance comparison between the  $(\text{NH}_4)_{0.38}\text{V}_2\text{O}_5/\text{CNTs}$  paper electrode and the control electrode prepared through slurring with PVDF/PTFE as binder. c) Ragone plots of  $(\text{NH}_4)_{0.38}\text{V}_2\text{O}_5/\text{CNTs}$  paper electrode compared to other cathodes for AZIBs. d) XRD pattern of  $(\text{NH}_4)_2\text{V}_3\text{O}_8/\text{C}$ . e) Rate performance of  $\text{Zn}/(\text{NH}_4)_2\text{V}_3\text{O}_8/\text{C}$  battery. f) Comparison of Ragone plots of  $\text{Zn}/(\text{NH}_4)_2\text{V}_3\text{O}_8/\text{C}$  battery with those reported for vanadium-based electrodes applied to AZIBs (the value is based on the mass of the cathode material). g) GCD curves of  $\text{NH}_4\text{V}_4\text{O}_{10}$  in first three cycles. h) Cycling stability with the corresponding coulombic efficiencies at  $2 \text{ A g}^{-1}$ . a–c) Reproduced with permission.<sup>[330]</sup> Copyright 2021, Elsevier. d–f) Reproduced with permission.<sup>[339]</sup> Copyright 2020, Elsevier. g, h) Reproduced with permission.<sup>[340]</sup> Copyright 2021, Springer.

tetrahedron and the  $\text{VO}_5$  pyramid are linked by O atoms to form thin sheets parallel to  $(001)$ .<sup>[336]</sup> These structural features can be used in SIBs and LIBs to store  $\text{Na}^+$  and  $\text{Li}^+$ .  $\text{NH}_4^+$  in  $(\text{NH}_4)_2\text{V}_3\text{O}_8$  is located in the tetrahedral site between the V and O atomic layers and can be occupied by  $\text{Na}^+$  or  $\text{Li}^+$ .<sup>[337,338]</sup> The ionic radius of  $\text{Zn}^{2+}$  ( $0.76 \text{ \AA}$ ) is smaller than that of  $\text{NH}_4^+$  ( $1.43 \text{ \AA}$ ), so it is

allowed to reversibly (de)intercalate  $\text{Zn}^{2+}$  in  $(\text{NH}_4)_2\text{V}_3\text{O}_8$  cathode and adapt to volume expansion. Jiang and colleagues<sup>[339]</sup> reported for the first time that  $(\text{NH}_4)_2\text{V}_3\text{O}_8$  nanoparticles were encapsulated into an amorphous carbon matrix as AZIBs cathode with high capacity. However, carbon is not observed in the XRD pattern (Figure 22d), this is because most of the carbon phase

prepared by hydrothermal method is amorphous carbon, which cannot be detected by XRD.  $(\text{NH}_4)_2\text{V}_3\text{O}_8$  did not crystallize well in HRTEM because it was covered by a layer of amorphous carbon.  $\text{Zn}/[(\text{NH}_4)_2\text{V}_3\text{O}_8/\text{C}]$  battery has significantly enhanced electrochemical performance, with a specific capacity of  $356 \text{ mAh g}^{-1}$  at  $0.1 \text{ A g}^{-1}$  (Figure 22e), high-rate performance and cycle life of  $135 \text{ mA h}^{-1}$  after 2000 cycles at  $1 \text{ A g}^{-1}$ , as well as the energy density of  $334 \text{ Wh kg}^{-1}$  at  $294 \text{ W kg}^{-1}$  (Figure 22f).

**$\text{NH}_4\text{V}_4\text{O}_{10}$ :** Monoclinic  $\text{NH}_4\text{V}_4\text{O}_{10}$  consists of a distorted  $\text{VO}_6$  octahedron. The vanadium octahedron shares an edge, forming a stable bilayer structure that includes  $\text{V}_4\text{O}_{10}$  units stacked along the  $\alpha$ -axis.<sup>[332]</sup> Zong et al.<sup>[340]</sup> synthesized 2D  $\text{NH}_4\text{V}_4\text{O}_{10}$  nanosheets by heat-treating  $\text{NH}_4\text{V}_4\text{O}_{10}$  nanosheets grown on CC at low temperature in air. The increased interlayer spacing of  $\text{NH}_4\text{V}_4\text{O}_{10}$  is conducive to the rapid migration of  $\text{Zn}^{2+}$  and high storage capacity, which ensures the high reversibility of the electrochemical reaction and the good stability of the layered structure. The  $\text{NH}_4\text{V}_4\text{O}_{10}$  nanosheets have a high specific capacity of  $457 \text{ mAh g}^{-1}$  at  $0.1 \text{ A g}^{-1}$  (Figure 22g) and superior cycle stability with a capacity retention of 81% after 1000 cycles at  $2 \text{ A g}^{-1}$  (Figure 22h). Huang et al.<sup>[341]</sup> used the  $\text{NH}_4\text{V}_4\text{O}_{10}$  as an example to optimize engineering by selecting the electrolyte and adjusting the proportion of conductive carbon in the electrode. The  $\text{NH}_4\text{V}_4\text{O}_{10}$ -541 electrode ( $\text{NH}_4\text{V}_4\text{O}_{10}$  sample, acetylene black to poly(vinylidene difluoride) in a weight ratio of 50:40:10) can provide a high reversible capacity of  $430.0 \text{ mAh g}^{-1}$  at  $0.1 \text{ A g}^{-1}$ , good speed capacity of  $277.1 \text{ mAh g}^{-1}$  at  $10 \text{ A g}^{-1}$ , as well as superior cycle stability with a capacity retention of 72.2% over 3000 cycles at  $10 \text{ A g}^{-1}$ . Sun and colleagues<sup>[342]</sup> proposed a self-template method for the synthesis of  $\text{NH}_4\text{V}_4\text{O}_{10}$  with decussate structure and intercalation mechanism by a simple one-step hydrothermal method, which achieved a remarkable mass-energy density of  $332.25 \text{ Wh kg}^{-1}$ , excellent rate performance, and stable cycle stability. In order to improve the cycling stability and diffusion rate of vanadium-based compounds, doping other electrochemically active substances (e.g., Ti) into the compounds is an effective method.<sup>[343–346]</sup> He et al.<sup>[347]</sup> prepared Ti-doped  $\text{NH}_4\text{V}_4\text{O}_{10}$  using a robust bilayer structure, which not only ensured rapid and reversible  $\text{Zn}^{2+}$  intercalation, but also reduced the accumulation of  $\text{Zn}^{2+}$ . Compared with the pure  $\text{NH}_4\text{V}_4\text{O}_{10}$ , the Ti-doped  $\text{NH}_4\text{V}_4\text{O}_{10}$  has faster diffusion kinetics, higher electrochemical reversibility, and better structural stability. For example, at  $2 \text{ A g}^{-1}$ , the capacity retention rate of Ti-doped  $\text{NH}_4\text{V}_4\text{O}_{10}$  after 2000 cycles is 89.02%, which is much higher than that of  $\text{NH}_4\text{V}_4\text{O}_{10}$  (62.86%).

#### 4.4.2. The Co-Intercalation of $\text{NH}_4^+$ and $\text{H}_2\text{O}$

**$\text{NH}_4\text{V}_3\text{O}_8 \cdot 0.5\text{H}_2\text{O}$ :**  $\text{NH}_4\text{V}_3\text{O}_8 \cdot 0.5\text{H}_2\text{O}$  is made up of 2D  $\text{V}_3\text{O}_8$  layers, consisting of  $\text{VO}_6$  octahedrons and  $\text{VO}_5$  square pyramids by sharing corners, and are pinned together by the  $\text{NH}_4^+$ .<sup>[332]</sup> In addition, the electrochemical performance of  $\text{NH}_4\text{V}_3\text{O}_8 \cdot 0.5\text{H}_2\text{O}$  is significantly improved by the intercalation of  $\text{H}_2\text{O}$  molecules in the layered structure. Jiang et al.<sup>[348]</sup> prepared  $\text{NH}_4\text{V}_3\text{O}_8 \cdot 0.5\text{H}_2\text{O}$  nanobelts by low-temperature hydrothermal to prove that the intercalation of  $\text{H}_2\text{O}$  molecules in the layer structure had a strong enhancement effect on the electrochemical performance of  $\text{NH}_4\text{V}_3\text{O}_8$ .  $\text{NH}_4\text{V}_3\text{O}_8 \cdot 0.5\text{H}_2\text{O}$  nanobelts have an ultra-high ca-

capacity of  $423 \text{ mAh g}^{-1}$  at  $0.1 \text{ A g}^{-1}$  and maintain long-term stability of 50.1% after 1000 cycles at  $1 \text{ A g}^{-1}$ .

**The Intercalation of Polyaniline in  $\text{NH}_4\text{V}_3\text{O}_8 \cdot 0.5\text{H}_2\text{O}$ :** The structure of PANI contains reducing units, so PANI may undergo redox reactions with host substances in the reaction system.<sup>[349]</sup> Therefore, PANI can be in situ intercalated into host materials to form hybrid materials during redox reactions.<sup>[350,351]</sup> In addition, the redox reaction of PANI with the host material in the reaction system may generate oxygen vacancies, which is conducive to the improvement of electron mobility.<sup>[352–354]</sup> Li and colleagues<sup>[355]</sup> designed an organic-inorganic (ammonium vanadate) hybrid cathode with extended layer spacing by intercalating polyaniline into the interlayer of  $\text{NH}_4\text{V}_3\text{O}_8 \cdot 0.5\text{H}_2\text{O}$ . After polyaniline intercalation, as shown in Figure 23a, the interlayer distance of  $\text{NH}_4\text{V}_3\text{O}_8 \cdot 0.5\text{H}_2\text{O}$  significantly increased from 7.9 to  $10.8 \text{ \AA}$ , providing fast channel for the diffusion of  $\text{Zn}^{2+}$ . The organic-inorganic (ammonium vanadate) hybrid cathode has good electrochemical performance, with a high initial capacity of  $397.5 \text{ mAh g}^{-1}$  at  $1 \text{ A g}^{-1}$  (Figure 23b) and good cycle stability of  $300 \text{ mAh g}^{-1}$  at  $10 \text{ A g}^{-1}$  with a capacity retention rate of 95% after more than 1000 cycles (Figure 23c) due to the intercalation of PANI.

**$(\text{NH}_4)_2\text{V}_6\text{O}_{16} \cdot 1.5\text{H}_2\text{O}$ :** In the structure of  $(\text{NH}_4)_2\text{V}_6\text{O}_{16} \cdot 1.5\text{H}_2\text{O}$ ,  $\text{VO}_5$  square pyramid and  $\text{VO}_6$  octahedral chains form  $\text{V}_3\text{O}_8$  layers along the z-axis by sharing the corners, and hydrated  $\text{NH}_4^+$  in interstitial sites act as “pillars” to stabilize the layered structure. Because the valence state (+5) of V in the  $(\text{V}_6\text{O}_{16})^{2-}$  structure is higher than that of  $\text{M}(\text{M} = \text{metal})\text{V}_2\text{O}_5 \cdot n\text{H}_2\text{O}$ ,  $(\text{NH}_4)_2\text{V}_6\text{O}_{16} \cdot 1.5\text{H}_2\text{O}$  is able to accommodate more  $\text{Zn}^{2+}$ .<sup>[21]</sup> Wang et al.<sup>[356]</sup> presented a highly reversible AZIB system with  $(\text{NH}_4)_2\text{V}_6\text{O}_{16} \cdot 1.5\text{H}_2\text{O}$  nanobelts as cathode materials by one-step hydrothermal method and  $\text{ZnSO}_4$  aqueous solution as electrolyte. The  $(\text{NH}_4)_2\text{V}_6\text{O}_{16} \cdot 1.5\text{H}_2\text{O}$  nanobelts cathode has an excellent reversible specific capacity of  $479 \text{ mAh g}^{-1}$  with an ideal energy density of  $371.5 \text{ Wh kg}^{-1}$  at  $0.1 \text{ A g}^{-1}$ , and has satisfactory cycle stability, which is  $152 \text{ mAh g}^{-1}$  maintained more than 3000 cycles at  $5 \text{ A g}^{-1}$ . Chen and coworkers<sup>[357]</sup> fabricated the  $(\text{NH}_4)_2\text{V}_6\text{O}_{16} \cdot 1.5\text{H}_2\text{O}$  nanostructure by a simple microwave-assisted hydrothermal reaction and studied the structure information and zinc storage properties of  $(\text{NH}_4)_2\text{V}_6\text{O}_{16} \cdot 1.5\text{H}_2\text{O}$  in detail. The  $\text{Zn}(\text{H}_2\text{O})_6^{2+}$  captures during the initial discharge not only help stabilize the vanadium oxide layer, but also provide the sufficient interlayer distance for fast ionic dynamics during the previous (de)intercalation.

**The Intercalation of Poly(3,4-Ethylene Dioxathiophene) in  $(\text{NH}_4)_2\text{V}_6\text{O}_{16} \cdot 1.5\text{H}_2\text{O}$ :** The electrical conductivity can be improved by intercalating PEDOT into the vanadate nanofiber lattice. In addition, the intercalated conductive polymer serves as a more solid pillar for the vanadate layered structure, achieving stable (dis)charging compared to the cationic and water molecules. By extending the distance between vanadate crystal planes through the intercalation of PEDOT, the melting rate of electrolyte cations can also be increased, thus making vanadate with excellent rate capability. In addition, the lubricating effect of the intercalated PEDOT prevents the trapping of electrolyte ions.<sup>[358,359]</sup> Kim et al.<sup>[360]</sup> for the first time, enhanced the rate capability, electrochemical reversibility, and cyclic stability of ammonium vanadate nanofiber (AVNF) as AZIBs cathode material by using PEDOT to control the interlayer structure of

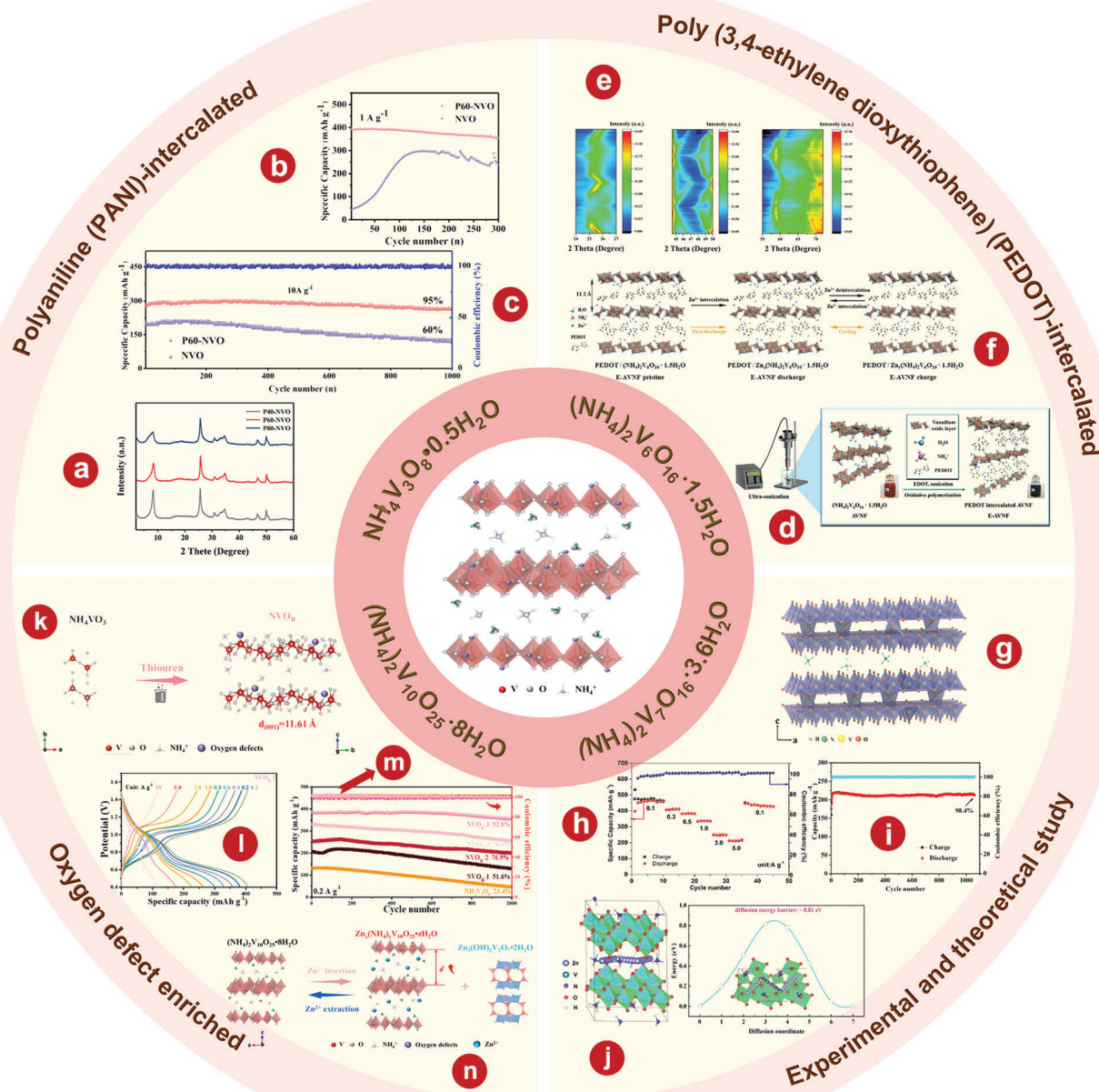


**Figure 23.** a) XRD patterns of  $\text{P}(x)\text{-NH}_4\text{V}_3\text{O}_8 \cdot 0.5\text{H}_2\text{O}$  ( $x = 40, 60, 80$ ) with different aniline concentration. Cycling performance of  $\text{NH}_4\text{V}_3\text{O}_8 \cdot 0.5\text{H}_2\text{O}$  and  $\text{P60-NH}_4\text{V}_3\text{O}_8 \cdot 0.5\text{H}_2\text{O}$  electrodes at b)  $1$  and c)  $10 \text{ A g}^{-1}$ . d) Schematic illustration of PEDOT and ammonium ion intercalation into the vanadate layer via sonication. e) In situ XRD contour plots of E-AVNf within selected scanning angle ( $2\theta$ ) domains of c)  $24^\circ\text{--}27^\circ$ ,  $44.5^\circ\text{--}50^\circ$ , and  $55^\circ\text{--}72^\circ$ . f) Schematic illustrations of  $\text{Zn}^{2+}$  intercalation/de-intercalation process into E-AVNf during cycling. g) Crystal structure of  $(\text{NH}_4)_2\text{V}_7\text{O}_{16}$  viewed along the  $b$ -axis. h) Rate performance of the  $(\text{NH}_4)_2\text{V}_7\text{O}_{16} \cdot 3.6\text{H}_2\text{O}$  cathode. i) Long-term stability of the  $(\text{NH}_4)_2\text{V}_7\text{O}_{16} \cdot 3.6\text{H}_2\text{O}$  cathode at  $5 \text{ A g}^{-1}$ . j) The simulated diffusion pathway of  $\text{Zn}^{2+}$  in  $(\text{NH}_4)_2\text{V}_7\text{O}_{16}$  (side view) and the corresponding diffusion energy barrier profiles (the inset is the diffusion pathway in top view). k) Schematic diagram of the preparation of oxygen defect enriched  $(\text{NH}_4)_2\text{V}_{10}\text{O}_{25} \cdot 8\text{H}_2\text{O}$ . l) GCD profiles of oxygen defect enriched  $(\text{NH}_4)_2\text{V}_{10}\text{O}_{25} \cdot 8\text{H}_2\text{O}$ . m) Cyclability of oxygen defect enriched  $(\text{NH}_4)_2\text{V}_{10}\text{O}_{25} \cdot 8\text{H}_2\text{O}$  and  $\text{NH}_4\text{V}_3\text{O}_8$  obtained at  $0.2 \text{ A g}^{-1}$ . n) Schematic diagram of the  $\text{Zn}^{2+}$  insertion mechanism on  $(\text{NH}_4)_2\text{V}_{10}\text{O}_{25} \cdot 8\text{H}_2\text{O}$  cathode. a–c) Reproduced with permission.<sup>[355]</sup> Copyright 2022, Elsevier. d–f) Reproduced with permission.<sup>[360]</sup> Copyright 2021, Wiley-VCH. g–j) Reproduced with permission.<sup>[365]</sup> Copyright 2021, Elsevier. k–n) Reproduced with permission.<sup>[367]</sup> Copyright 2021, Elsevier.



AVNF crystals via a sample sonochemical method (Figure 23d). In situ XRD contour plots of PEDOT-AVNF (E-AVNF) within selected scanning angle ( $2\theta$ ) domains of  $24^\circ$ – $27^\circ$ ,  $44.5^\circ$ – $50^\circ$ , and  $55^\circ$ – $72^\circ$  are shown in Figure 23e to further investigate the (dis)charging mechanism of the E-AVNF electrodes. The  $\text{Zn}^{2+}$  storage mechanism of E-AVNF is shown in Figure 23f. The results demonstrate that the control of the intermediate layer through the spacer ammonium vanadate of PEDOT results in rapid diffusion of  $\text{Zn}^{2+}$ , reversible electrochemical reactions, and high performance of AZIBs.

$(\text{NH}_4)_2\text{V}_7\text{O}_{16} \cdot 3.6\text{H}_2\text{O}$ : As a new type of ammonium vanadate,  $(\text{NH}_4)_2\text{V}_7\text{O}_{16} \cdot 3.6\text{H}_2\text{O}$  has been rarely studied. Despite the unprecedented stoichiometry and crystal structure, the layered structure is similar to the others. The structure consists of stacked layers of  $\text{V}_7\text{O}_{16}$  aligned along the  $c$ -axis and two  $\text{NH}_4^+$  per formulation unit occupying the interlayer space. Each  $\text{NH}_4^+$  is hydrogen bonded to four lattice oxygen atoms to form a stable structure with a large interlayer space, which enables the intercalation of various visiting ions. Unlike ethylene diamine vanadate, which was previously reported to be intercalated by neutral molecules, the interlayer space of  $(\text{NH}_4)_2\text{V}_7\text{O}_{16}$  is occupied by  $\text{NH}_4^+$ .<sup>[361]</sup> In addition, the average oxidation state of vanadium ions in the  $\text{V}_7\text{O}_{16}$  layer is 4.29+ and the formal charge is 2-, which is lower than that of other ammonium vanadates.<sup>[362–364]</sup> Wang et al.<sup>[365]</sup> successfully fabricated attractive  $(\text{NH}_4)_2\text{V}_7\text{O}_{16} \cdot 3.6\text{H}_2\text{O}$  nanoplates via a facile hydrothermal reaction and applied them in AZIBs. The crystal structure  $(\text{NH}_4)_2\text{V}_7\text{O}_{16}$  is shown in Figure 23g. The unique structure of  $\text{NH}_4^+$  intercalated in the  $\text{V}_7\text{O}_{16}$  layer expands the layer spacing to 9.1 Å, and the capacity reaches 465.0 mAh g<sup>-1</sup> at 0.1 A g<sup>-1</sup> (Figure 23h), as well as the capacity retention rate is 98.4% at 5 A g<sup>-1</sup> (Figure 23i). In addition, the reversible (dis)charging process and kinetic behavior of  $(\text{NH}_4)_2\text{V}_7\text{O}_{16} \cdot 3.6\text{H}_2\text{O}$  electrode are investigated by DFT calculations (Figure 23j) and ex situ XRD.

$(\text{NH}_4)_2\text{V}_{10}\text{O}_{25} \cdot 8\text{H}_2\text{O}$ :  $(\text{NH}_4)_2\text{V}_{10}\text{O}_{25} \cdot 8\text{H}_2\text{O}$  describes a characteristic layered structure consisting of the VO layer and interstitial  $\text{NH}_4^+$  and  $\text{H}_2\text{O}$ .  $\text{NH}_4^+$  and  $\text{H}_2\text{O}$  in  $(\text{NH}_4)_2\text{V}_{10}\text{O}_{25} \cdot 8\text{H}_2\text{O}$  are located at the tetrahedral sites between the layers of V and O atoms and among the VO layers, which are available for occupation by metal ions (e.g.,  $\text{Zn}^{2+}$ ).<sup>[365,366]</sup> Cao et al.<sup>[367]</sup> reasonably designed an advanced oxygen defect enriched  $(\text{NH}_4)_2\text{V}_{10}\text{O}_{25} \cdot 8\text{H}_2\text{O}$  nanosheet cathode (Figure 23k) with extended tunnel structure, excellent electrical conductivity, and structural stability, exhibiting rapid  $\text{Zn}^{2+}$  diffusion and superior performance. The AZIB with oxygen defect enriched  $(\text{NH}_4)_2\text{V}_{10}\text{O}_{25} \cdot 8\text{H}_2\text{O}$  nanosheets cathode has a very high capacity of 408 mA h g<sup>-1</sup> at 0.1 A g<sup>-1</sup> (Figure 23l), long-time stability of 94.1% retention over 4000 cycles (Figure 23m) and superior energy density of 287 Wh kg<sup>-1</sup>. As shown in Figure 23n, the electrochemical mechanism of oxygen defect enriched  $(\text{NH}_4)_2\text{V}_{10}\text{O}_{25} \cdot 8\text{H}_2\text{O}$  cathode based on reversible  $\text{Zn}^{2+}$  intercalation is demonstrated by a variety of characterization techniques (e.g., ex situ XRD pattern). Bai and colleagues<sup>[368]</sup> developed an advanced stainless steel (SS)-supported oxygen-rich vacancy  $(\text{NH}_4)_2\text{V}_{10}\text{O}_{25} \cdot 8\text{H}_2\text{O}$  cistern-like nanobelts cathode with widened layer spacing and ultrafast reaction kinetic. The SS-supported oxygen-rich vacancy  $(\text{NH}_4)_2\text{V}_{10}\text{O}_{25} \cdot 8\text{H}_2\text{O}$  cistern-like nanobelt cathode has a high capacity of 331.4 mAh g<sup>-1</sup> at 0.3 A g<sup>-1</sup>, superior rate performance, and excellent long-time stability of 78.3 mAh g<sup>-1</sup> more than 7500 cycles at 4.8 A g<sup>-1</sup>.

## 4.5. Mixture of Different Kinds of Cations

### 4.5.1. The Co-Intercalation of Different Kinds of Cations

$\text{K}_x(\text{NH}_4)_y\text{V}_4\text{O}_{10}$ : Compared with only  $\text{NH}_4^+$  intercalation, the addition of monovalent basic alkaline cations can be intercalated into the interlayer space to strengthen ionic bonds and thus stabilize the layered structure.<sup>[369]</sup> Zong et al.<sup>[370]</sup> synthesized potassium ammonium vanadate as the cathode for AZIB by substituting part of the  $\text{NH}_4^+$  between  $\text{NH}_4\text{V}_4\text{O}_{10}$  layers with  $\text{K}^+$ . The schematic illustration of the preparation process and the crystal structure of  $\text{NH}_4\text{V}_4\text{O}_{10}$  and  $\text{K}_x(\text{NH}_4)_y\text{V}_4\text{O}_{10}$  is shown in Figure 24a. The intercalation of  $\text{K}^+$  results in a subtle shrinkage of the ammonium vanadate lattice distance and an increase in oxygen vacancies. As expected,  $\text{K}_x(\text{NH}_4)_y\text{V}_4\text{O}_{10}$  has a better discharge capacity of 464 mAh g<sup>-1</sup> than  $\text{NH}_4\text{V}_4\text{O}_{10}$  (391 mAh g<sup>-1</sup>) at 0.1 A g<sup>-1</sup> (Figure 24b), and good cycle stability with a retention of 90% more than 3000 cycles at 5 A g<sup>-1</sup> (Figure 24c). As shown in Figure 24d,e, DFT calculation shows that  $\text{K}_x(\text{NH}_4)_y\text{V}_4\text{O}_{10}$  has modulated electronic structure and better diffusion path of  $\text{Zn}^{2+}$ , and the migration barrier is lower than  $\text{NH}_4\text{V}_4\text{O}_{10}$ . Based on electrochemical reaction kinetics analysis and ex situ characterizations, the possible charge storage mechanism is shown in Figure 24f.

### 4.5.2. The Co-Intercalation of Different Kinds of Cations and $\text{H}_2\text{O}$

$\text{K}_{0.09}\text{Mg}_{0.03}\text{V}_2\text{O}_5 \cdot n\text{H}_2\text{O}$ : The intercalation of two ions ( $\text{K}^+$  and  $\text{Mg}^{2+}$ ) in hydrated vanadium oxides was investigated in terms of the contraction of the structure by  $\text{K}^+$  and the expansion of the structure by  $\text{Mg}^{2+}$ .<sup>[274–276,371]</sup> Feng and colleagues<sup>[372]</sup> intercalated both the monovalent metal  $\text{K}^+$  and the divalent alkaline metal  $\text{Mg}^{2+}$  into the  $\text{V}_2\text{O}_5 \cdot n\text{H}_2\text{O}$  layers by a one-step hydrothermal method. In addition, single  $\text{K}^+$  and single  $\text{Mg}^{2+}$  intercalations were also prepared, as shown in Figure 24g.  $\text{Mg}^{2+}$  can increase the spacing between  $\text{V}_2\text{O}_5 \cdot n\text{H}_2\text{O}$  layers, expand ion transport channels, and improve the specific capacity of batteries. At the same time,  $\text{K}^+$  can make the connection between the V–O layers closer, so that the structure of the material is more stable. Because of the intercalation of these two ions, the  $\text{KMgVOH}$  cathode has an unprecedentedly high specific capacity of 423 mAh g<sup>-1</sup> at 0.1 A g<sup>-1</sup> (Figure 24h) and good cycle stability with a retention of 72% after 2000 cycles 4 A g<sup>-1</sup> (Figure 24i). The storage mechanism of this process is shown in Figure 24j, which is proved by SEM, ex situ XRD, and XPS.

$\text{Na}_{0.3}(\text{NH}_4)_{0.6}\text{V}_4\text{O}_{10} \cdot 0.4\text{H}_2\text{O}$ : The  $\text{Na}^+$  pre-intercalation strategy is promising to improve the cyclic life and electrochemical performance of  $\text{NH}_4\text{V}_4\text{O}_{10}$ . Wang et al.<sup>[373]</sup> prepared a non-stoichiometric  $\text{Na}_{0.3}(\text{NH}_4)_{0.6}\text{V}_4\text{O}_{10} \cdot 0.4\text{H}_2\text{O}$  nanorods as a cathode material for AZIBs. The combined effect of  $\text{Na}^+$  pre-intercalated in  $\text{NH}_4\text{V}_4\text{O}_{10}$  and structural water enhances the diffusion kinetics, reduces the electrostatic repulsion of  $\text{Zn}^{2+}$  (de)intercalation, and keeps the layer structure stable. As shown in Figure 24k, XRD pattern is obtained to determine the crystal structure and phase purity of  $\text{Na}_{0.3}(\text{NH}_4)_{0.6}\text{V}_4\text{O}_{10} \cdot 0.4\text{H}_2\text{O}$ . The pre-intercalated  $\text{Na}^+$  replaces part of  $\text{NH}_4^+$  located between VO layers and maintains the layer structure of  $\text{NH}_4\text{V}_4\text{O}_{10}$ . The results show that the  $\text{Na}_{0.3}(\text{NH}_4)_{0.6}\text{V}_4\text{O}_{10} \cdot 0.4\text{H}_2\text{O}$  cathode has an excellent specific capacity of 400.2 mAh g<sup>-1</sup> at 0.1 A g<sup>-1</sup>,

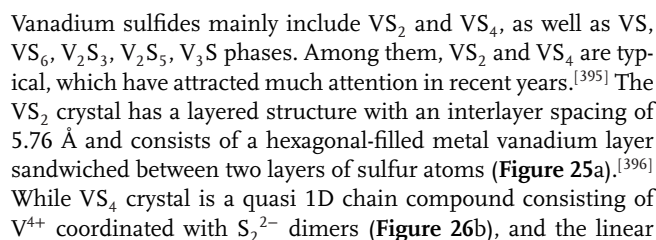


**Table 3.** Electrochemical performance of vanadates as cathodes in AZIBs.

Materials	Electrolyte	Specific capacity [mAh g <sup>-1</sup> ] (current density [A g <sup>-1</sup> ])	Capacity retention (cycles numbers)	Voltage range [V]	Ref.
LiV <sub>3</sub> O <sub>8</sub>	1 M ZnSO <sub>4</sub>	256 (0.016)	75.0% (65)	0.6–1.2	[241]
Li <sub>x</sub> V <sub>2</sub> O <sub>5</sub> · nH <sub>2</sub> O	2 M ZnSO <sub>4</sub>	407.6 (1)	76.3% (500)	0.4–1.4	[279]
Na <sub>0.33</sub> V <sub>2</sub> O <sub>5</sub>	3 M Zn(CF <sub>3</sub> SO <sub>3</sub> ) <sub>2</sub>	367 (0.1)	93.0% (1000)	0.2–1.6	[262]
Na <sub>0.56</sub> V <sub>2</sub> O <sub>5</sub>	3 M ZnSO <sub>4</sub> + 0.5 M Na <sub>2</sub> SO <sub>4</sub>	317 (0.1)	84.0% (1000)	0.4–1.5	[376]
Na <sub>1.25</sub> V <sub>3</sub> O <sub>8</sub>	3 M Zn(CF <sub>3</sub> SO <sub>3</sub> ) <sub>2</sub>	390 (0.1)	88.2% (2000)	0.2–1.9	[377]
Na <sub>2</sub> V <sub>6</sub> O <sub>16</sub> · 3H <sub>2</sub> O	1 M ZnSO <sub>4</sub>	361 (0.1)	80.0% (1000)	0.4–1.4	[333]
Na <sub>2</sub> V <sub>6</sub> O <sub>16</sub> · 2.14H <sub>2</sub> O	1 M ZnSO <sub>4</sub> · 7H <sub>2</sub> O	466 (0.1)	90.0% (2000)	0.2–1.6	[378]
K <sub>0.23</sub> V <sub>2</sub> O <sub>5</sub>	2 M Zn(CF <sub>3</sub> SO <sub>3</sub> ) <sub>2</sub>	284 (0.1)	92.8% (500)	0.1–1.7	[266]
K <sub>0.25</sub> V <sub>2</sub> O <sub>5</sub>	2 M ZnSO <sub>4</sub>	306 (0.1)	99.0% (500)	0.4–1.4	[379]
KV <sub>2</sub> O <sub>5</sub>	1 M ZnSO <sub>4</sub>	439 (0.05)	96.0% (1500)	0.4–1.4	[380]
Na <sub>1.2</sub> V <sub>3</sub> O <sub>8</sub> /K <sub>2</sub> V <sub>6</sub> O <sub>16</sub> · 1.5H <sub>2</sub> O	3 M ZnSO <sub>4</sub>	393 (0.1)	85.0% (800)	0.4–1.4	[381]
MgV <sub>2</sub> O <sub>4</sub>	2 M Zn(TFSI) <sub>2</sub>	272 (0.2)	60.6% (500)	0.2–1.4	[382]
Mg <sub>x</sub> V <sub>2</sub> O <sub>5</sub> · nH <sub>2</sub> O	3 M Zn(CF <sub>3</sub> SO <sub>3</sub> ) <sub>2</sub>	353 (0.1)	97.0% (2000)	0.1–1.8	[276]
Ca <sub>0.67</sub> V <sub>8</sub> O <sub>20</sub> · 3.5H <sub>2</sub> O	3 M Zn(CF <sub>3</sub> SO <sub>3</sub> ) <sub>2</sub>	466 (0.1)	74.0% (2000)	0.4–1.5	[383]
Ag <sub>0.4</sub> V <sub>2</sub> O <sub>5</sub>	3 M ZnSO <sub>4</sub>	237 (0.5)	93.0% (4000)	0.4–1.4	[384]
Co <sub>0.247</sub> V <sub>2</sub> O <sub>5</sub> · 0.944H <sub>2</sub> O	3 M Zn(CF <sub>3</sub> SO <sub>3</sub> ) <sub>2</sub>	432 (0.1)	90.3% (7500)	0.3–2.2	[385]
δ-Ni <sub>0.25</sub> V <sub>2</sub> O <sub>5</sub> · nH <sub>2</sub> O	3 M ZnSO <sub>4</sub>	402 (0.2)	98.0% (1200)	0.3–1.7	[386]
CuV <sub>2</sub> O <sub>6</sub>	3 M Zn(CF <sub>3</sub> SO <sub>3</sub> ) <sub>2</sub>	427 (0.1)	99.3% (3000)	0.2–1.6	[387]
CuV <sub>2</sub> O <sub>6</sub>	3 M Zn(CF <sub>3</sub> SO <sub>3</sub> ) <sub>2</sub>	338 (0.1)	100.0% (1200)	0.2–1.4	[388]
Cu <sub>3</sub> (OH) <sub>2</sub> V <sub>2</sub> O <sub>7</sub> · 2H <sub>2</sub> O	3 M Zn(CF <sub>3</sub> SO <sub>3</sub> ) <sub>2</sub>	336 (0.1)	80.0% (3000)	0.4–1.4	[389]
Cu <sub>3</sub> V <sub>2</sub> O <sub>7</sub> (OH) <sub>2</sub> · 2H <sub>2</sub> O	2.5 M Zn(CF <sub>3</sub> SO <sub>3</sub> ) <sub>2</sub>	216 (0.1)	89.3% (500)	0.2–1.6	[390]
PEDOT-NH <sub>4</sub> V <sub>3</sub> O <sub>8</sub>	3 M Zn(CF <sub>3</sub> SO <sub>3</sub> ) <sub>2</sub>	357 (0.05)	94.1% (5000)	0.4–1.6	[391]
(NH <sub>4</sub> ) <sub>2</sub> V <sub>3</sub> O <sub>8</sub>	3 M Zn(CF <sub>3</sub> SO <sub>3</sub> ) <sub>2</sub>	356 (0.1)	50.7% (2000)	0.4–1.6	[339]
(NH <sub>4</sub> ) <sub>2</sub> V <sub>4</sub> O <sub>9</sub>	3 M Zn(CF <sub>3</sub> SO <sub>3</sub> ) <sub>2</sub>	376 (0.1)	87.6% (2000)	0.3–1.3	[392]
NH <sub>4</sub> V <sub>4</sub> O <sub>10</sub>	3 M Zn(CF <sub>3</sub> SO <sub>3</sub> ) <sub>2</sub>	147 (0.2)	70.3% (5000)	0.8–1.7	[362]
(NH <sub>4</sub> ) <sub>2</sub> V <sub>6</sub> O <sub>16</sub>	3 M Zn(CF <sub>3</sub> SO <sub>3</sub> ) <sub>2</sub>	324 (0.1)	78.3% (2000)	0.3–1.7	[393]
(NH <sub>4</sub> ) <sub>2</sub> V <sub>6</sub> O <sub>16</sub> · 1.5H <sub>2</sub> O	2 M ZnSO <sub>4</sub>	479 (0.1)	76.0% (3000)	0.2–1.6	[356]
(NH <sub>4</sub> ) <sub>2</sub> V <sub>6</sub> O <sub>16</sub> · 1.5H <sub>2</sub> O	3 M Zn(CF <sub>3</sub> SO <sub>3</sub> ) <sub>2</sub>	120 (0.1)	75.0% (10 000)	0.4–1.6	[357]
(NH <sub>4</sub> ) <sub>2</sub> V <sub>10</sub> O <sub>25</sub> · 8H <sub>2</sub> O	3 M Zn(CF <sub>3</sub> SO <sub>3</sub> ) <sub>2</sub>	417 (0.1)	63.6% (500)	0.3–1.3	[364]
(NH <sub>4</sub> ) <sub>2</sub> V <sub>10</sub> O <sub>25</sub> · 8H <sub>2</sub> O	3 M Zn(CF <sub>3</sub> SO <sub>3</sub> ) <sub>2</sub>	229 (0.1)	90.1% (5000)	0.7–1.7	[334]
NaCa <sub>0.6</sub> V <sub>6</sub> O <sub>16</sub> · 3H <sub>2</sub> O	3 M Zn(CF <sub>3</sub> SO <sub>3</sub> ) <sub>2</sub>	347 (0.1)	94.0% (2000)	0.4–1.5	[394]

structural units are stacked together by weak van der Waals interactions with an interchain distance of 5.83 Å.<sup>[397]</sup> The oxidation states of vanadium in VS<sub>2</sub> and VS<sub>4</sub> are the same, but the oxidation states of sulfide are different (There is an S<sub>2</sub><sup>2-</sup> monomer in VS<sub>2</sub> and an S<sub>2</sub><sup>2-</sup> dimers in VS<sub>4</sub>).<sup>[398]</sup>

#### 5.1.1. VS<sub>2</sub>

In the crystal structure of VS<sub>2</sub>, each V atom is arranged around six S atoms and is covalently linked to the S atoms. The widely spaced layers of VS<sub>2</sub> allow easy (de)intercalation of Li<sup>+</sup>, Na<sup>+</sup>, Zn<sup>2+</sup>, or their solvation sheath in electrolyte.<sup>[399,400]</sup> The VS<sub>2</sub> nanosheets were synthesized by He et al.<sup>[149]</sup> though a simple hydrothermal reaction, and had a high capacity of 190.3 mA h g<sup>-1</sup> at 0.05 A g<sup>-1</sup>, as well as stable cycling stability as cathode materials of AZIBs. Ex situ TEM, ex situ XRD, and selected area electron diffraction (SAED) pattern results (Figure 25c,d) show that the interlayer space of VS<sub>2</sub> self-adapting the Zn<sup>2+</sup> intercalation expands along *c*-axis only 1.73% and slightly shrinking on the *a*- and *b*-

axes, which plays an important role in the realization of AZIBs with long life. Jiao and coworkers<sup>[401]</sup> developed an independent, free-binding cathode for AZIBs, consisting of hierarchical VS<sub>2</sub> in the 1T phase grown directly on a SS mesh (Figure 25e). The design of the open-structure electrode is beneficial to increase the contact area with the electrolyte, minimize the transmission path of zinc ions and electrons, reduce volume expansion, and achieve stable circulation. Therefore, the battery has a great zinc ion storage capacity of 198 mAh g<sup>-1</sup> and long-time cycle performance with a capacity retention rate of more than 80% at 2 A g<sup>-1</sup> after 2000 cycles (Figure 25f).

#### 5.1.2. VS<sub>4</sub>

As an analog of VS<sub>2</sub>, the VS<sub>4</sub> has a unique chain structure and a S<sub>2</sub><sup>2-</sup> group component, and is used for the research of energy storage materials.<sup>[402–406]</sup> Qian et al.<sup>[407]</sup> developed a patronite form of vanadium sulfide anchored on rGO prepared by a simple hydrothermal method and can be used as a cathode with



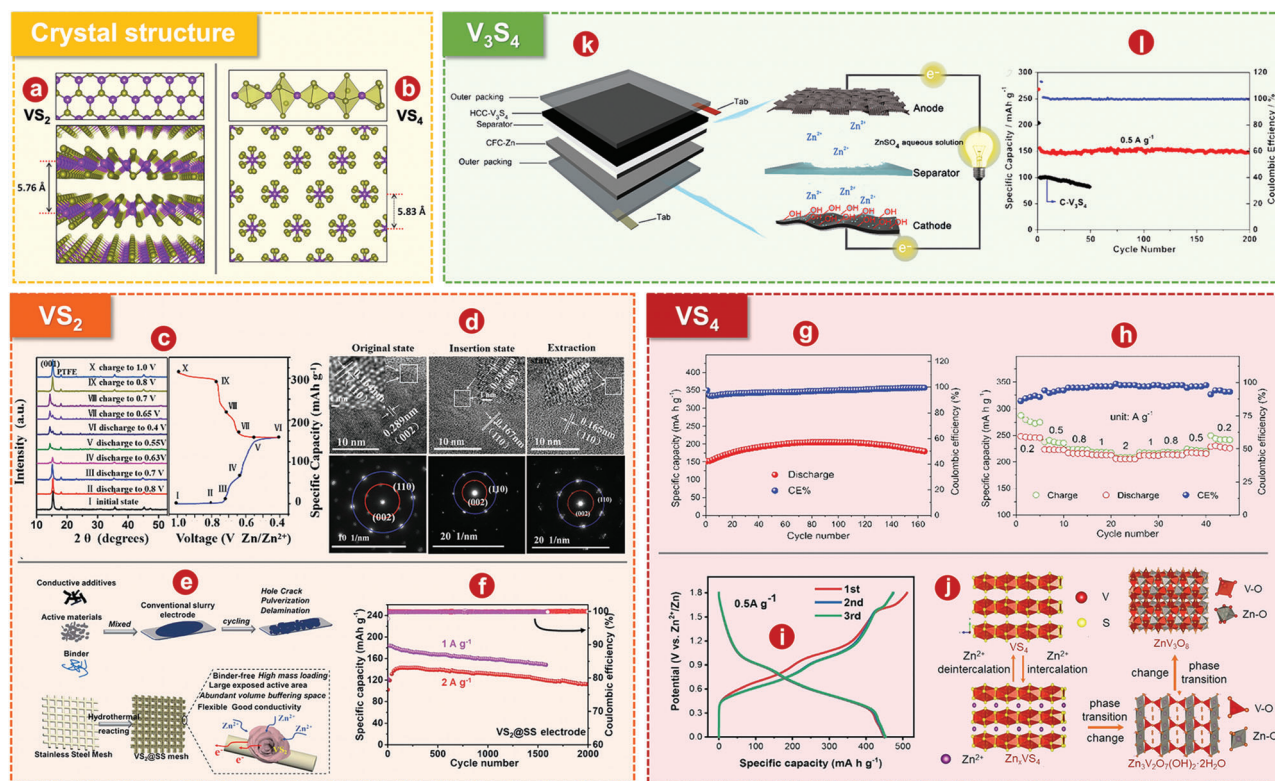


**Figure 25.** Schematic showing the geometries of a)  $\text{VS}_2$  and b)  $\text{VS}_4$ . (a) Top-view image (top) and side-view image (bottom) showing 2D sheets of  $\text{VS}_2$ . (b) Repeating unit of the 1D chain structure of  $\text{VS}_4$  (top) and side-view image of monoclinic  $\text{VS}_4$  optimized using DFT. The purple balls are V atoms, and the yellow-green balls are S atoms. (c) Ex situ XRD patterns of  $\text{VS}_2$  collected at various states. (d) HR-TEM images and SAED patterns. (e) Schematic illustration of the preparation processes for (top) the conventional slurry-coated electrode, and (bottom) the binder-free hierarchical  $\text{VS}_2$ @SS electrode. (f) Long-term cycling performance of the  $\text{VS}_2$ @SS electrode at 1 and 2  $\text{A g}^{-1}$ . (g) Cycle performance of  $\text{VS}_4$ @rGO at 1  $\text{A g}^{-1}$ . (h) Rate performance of  $\text{VS}_4$ @rGO. (i) Discharge-charge curves of  $\text{VS}_4$ @rGO composite electrode at 0.5  $\text{A g}^{-1}$ . (j) Schematic illustration showing the structural evolution of  $\text{VS}_4$  during discharging/charging processes. (k) Schematic of the HCC- $\text{V}_3\text{S}_4$ //CFC-Zn flexible device construction and microscopic components. (l) Comparison of the cycling stability of HCC- $\text{V}_3\text{S}_4$ //CFC-Zn and C- $\text{V}_3\text{S}_4$ //CFC-Zn at 0.5  $\text{A g}^{-1}$ . a, b) Reproduced with permission.<sup>[398]</sup> Copyright 2013, American Chemical Society. c, d) Reproduced with permission.<sup>[149]</sup> Copyright 2017, WILEY-VCH. e, f) Reproduced with permission.<sup>[401]</sup> Copyright 2019, The Royal Society of Chemistry. g, h) Reproduced with permission.<sup>[407]</sup> Copyright 2018, The Royal Society of Chemistry. i) Reproduced with permission.<sup>[408]</sup> Copyright 2021, The Royal Society of Chemistry. k, l) Reproduced with permission.<sup>[411]</sup> Copyright 2019, American Chemical Society.

high performance for AZIBs. As shown in Figure 25g,  $\text{VS}_4$ @rGO cathode exhibits an excellent capacity of  $180 \text{ mAh g}^{-1}$  with a capacity retention of 93.3% after 165 cycles at 1  $\text{A g}^{-1}$  thanks to  $\text{VS}_4$  unique crystal structure and rGO superior electrical conductivity. At the same time, when the current density increased from 0.2 to 2  $\text{A g}^{-1}$ , the capacity retention rate can reach 83.7% (Figure 25h). On the basis of this work, Chen et al.<sup>[408]</sup> designed morphologically optimized  $\text{VS}_4$ @rGO composites with ultra-high specific capacity of  $450 \text{ mA h g}^{-1}$  at 0.5  $\text{A g}^{-1}$  (Figure 25i) and high rate capacity of  $313.8 \text{ mA h g}^{-1}$  at 10  $\text{A g}^{-1}$ , when used as AZIBs cathode materials. In addition, as shown in Figure 25j, an irreversible phase transition of  $\text{VS}_4$  to  $\text{Zn}_3(\text{OH})_2\text{V}_2\text{O}_7 \cdot 2\text{H}_2\text{O}$  during charging and further from  $\text{Zn}_3(\text{OH})_2\text{V}_2\text{O}_7 \cdot 2\text{H}_2\text{O}$  to  $\text{ZnV}_2\text{O}_8$  was found during long-term cycling, which may be the main reason for the  $\text{VS}_4$ @rGO capacity decline.

### 5.1.3. $\text{V}_3\text{S}_4$

The crystal structure of  $\text{V}_3\text{S}_4$  has ordered V vacancies, which constitute the superstructure of the NiAs-type structure. This

structure can also be described as  $\text{VS}_2$  monolayer building blocks alternating between additional V atoms. Thus, an increase in electronic/ionic conductivity is expected.<sup>[409,410]</sup> Liu and colleagues<sup>[411]</sup> first proposed a new hydrophilic carbon substrate with acidic treated natural halloysite and CNTs as structural and interface modifiers, loading  $\text{V}_3\text{S}_4$  as a composite cathode (HCC- $\text{V}_3\text{S}_4$ ) into a flexible AZIB (Figure 25k). This flexible AZIB has a high specific capacity of  $148 \text{ mAh g}^{-1}$  with a capacity retention of 95% after 200 cycles at 0.5  $\text{A g}^{-1}$  (Figure 25l), an excellent rate performance, a high energy density of  $155.7 \text{ Wh kg}^{-1}$ , as well as a high power density of  $5000 \text{ W kg}^{-1}$ .

## 5.2. Vanadium Nitrides

The capacity degradation and kinetics retardation of  $\text{Zn}^{2+}$  exist in the cycling process.<sup>[316,412]</sup> Recently, VNs with cubic structures have become new cathode materials for AZIB to solve these problems.<sup>[413,414]</sup> It has been reported that VN-based materials undergo high-potential inverse reactions during initial charging and exhibit high capacity from the second cycle

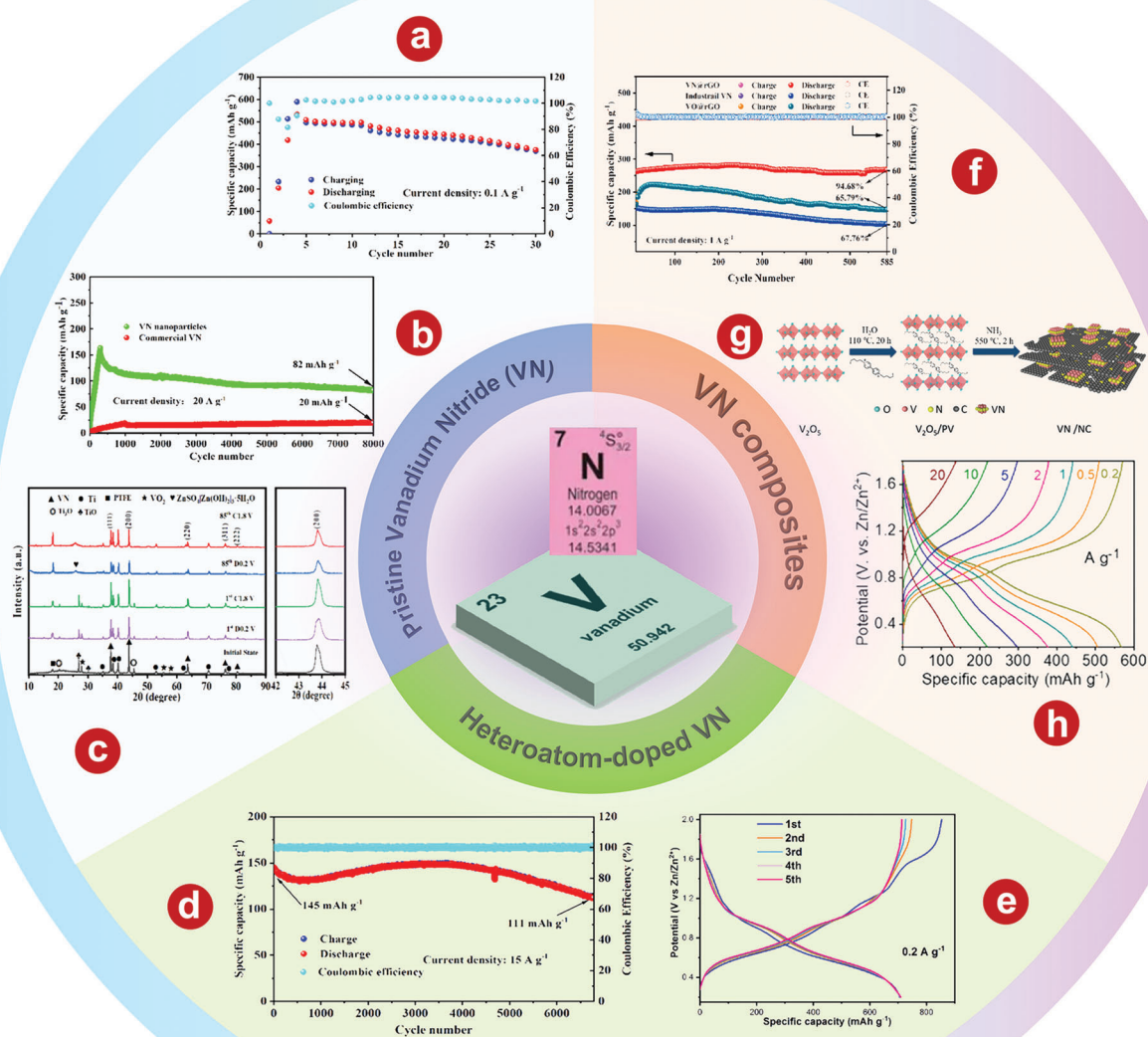


**Figure 26.** a) Cyclic curve of VN particles at a  $0.1 \text{ A g}^{-1}$ . b) Cycle stability of VN particles and commercial VN under  $20 \text{ A g}^{-1}$ . c) Ex situ XRD patterns of VN nanoparticles at a discharge voltage of  $0.2 \text{ V}$  and a charge voltage of  $1.8 \text{ V}$  for the first and 85th cycles. d) Cyclic stability of coral VN/C under  $15 \text{ A g}^{-1}$ . e) Charge-discharge profiles of O-VN-based AZIBs. f) Cycle performance of VN@rGO, industrial VN, and VO@rGO at  $1 \text{ A g}^{-1}$ . g) Schematic of the synthetic procedure for the VN/VN hybrid nanosheets. h) Galvanostatic charge-discharge plots of Zn//VN/NC cells at different current densities. a–c) Reproduced with permission.<sup>[417]</sup> Copyright 2021, American Chemical Society. d) Reproduced with permission.<sup>[418]</sup> Copyright 2021, American Chemical Society. e) Reproduced with permission.<sup>[77]</sup> Copyright 2021, Elsevier. f) Reproduced with permission.<sup>[420]</sup> Copyright 2021, Elsevier. g, h) Reproduced with permission.<sup>[421]</sup> Copyright 2022, The Royal Society of Chemistry.

onwards.<sup>[415,416]</sup> VNs generally come in three forms: VN,  $\text{V}_2\text{N}$ , and  $\text{V}_3\text{N}$ . Among them, VN is an isomer of VC and VO and belongs to the face-centered cubic structure, which is most widely used in AZIBs due to its good conductivity and spatial structure.

### 5.2.1. VN

Rong and coworkers<sup>[417]</sup> synthesized highly stable VN particles by reduction and nitrification of  $\text{V}_2\text{O}_5$  in an  $\text{NH}_3$  atmosphere. Thanks to their tiny particle size and porous stacking structure,

after 10 cycles of activation at a voltage range of 0.2–1.7 V, VN particles have a specific capacity of 496 mAh g<sup>-1</sup> at 1 A g<sup>-1</sup> (Figure 26a). Even at 20 A g<sup>-1</sup>, the capacity of VN particles is 153 mA h g<sup>-1</sup>, and after activation remains 82 mA h g<sup>-1</sup> after 8000 cycles (Figure 26b). In order to reveal the activation mechanism of VN particles, the XRD patterns of the 1st and 85th cycles are studied at a discharge voltage of 0.2 V and a charge voltage of 1.8 V (Figure 26c). Heteroatom doping can significantly improve the low conductivity of vanadium-based compounds and increase the transport rate of Zn<sup>2+</sup> in electrolytes. Su et al.<sup>[418]</sup> prepared coral carbon-doped VN by one-step solvothermal method and ammonia nitration roasting. Thanks to the nanoscale size and porous stacked structure, the coral carbon-doped VN cathode material has a specific capacity of 322 mAh g<sup>-1</sup> at 0.5 A g<sup>-1</sup>. When assembling the coral carbon-doped VN cathode in AZIB, this AZIB delivers a specific capacity of 111 mAh g<sup>-1</sup> with 6780 cycles and 95% capacity retention at 15 A g<sup>-1</sup> (Figure 26d). In addition, Chen et al.<sup>[77]</sup> developed an oxygen-doped VN (O-VN) cathode and for the first time confirmed the highly reversible cation conversion reaction of O-VN cathode in AZIBs. As shown in Figure 26e, the O-doped VN cathode shows an ultra-high discharge capacity of 705 mAh g<sup>-1</sup> at 0.2 A g<sup>-1</sup> due to cation conversion reactions and Zn<sup>2+</sup> deintercalation. The electrical conductivity of VN can be significantly improved by combining VN with conductive carbon composites.<sup>[419]</sup> Chen and colleagues<sup>[420]</sup> modified VN for industrial use with the high conductivity of rGO, giving the VN@rGO electrode high-rate capability and long period stability. The specific capacity of VN@rGO is 267.0 mA h g<sup>-1</sup>, and the specific capacity retention rate is 94.68% at 1 A g<sup>-1</sup> after 585 cycles, better than that of VN and VO@rGO (Figure 26f). Chen et al.<sup>[419]</sup> also demonstrated through kinetic studies that rGO can accelerate the redox reactions on the electrode surface to improve the pseudo-capacitance of the electrode by accelerating electron transport. In addition, as shown in Figure 26g, Niu et al.<sup>[421]</sup> developed new layer-by-layer VN/N-doped carbon hybrid nanosheets (VN/NC) as cathode materials through in situ thermal conversion of pyrolyzing pentyl viologen intercalated V<sub>2</sub>O<sub>5</sub>. At 0.2 A g<sup>-1</sup>, the VN/NC cathode shows a high discharge specific capacity of 566 mAh g<sup>-1</sup> (Figure 26h) and superior rate capability. Moreover, after 1000 cycles at 10 A g<sup>-1</sup>, VN/NC cathode has a good cycle stability of 131 mAh g<sup>-1</sup> with a capacity retention rate of 85% after more than 1000 cycles.

## 6. Summary and Outlook

To date, vanadium-based compounds reported for use as AZIBs cathodes exhibit a variety of crystal structures and properties, including typical layered vanadium-based compounds with high Zn<sup>2+</sup> storage capacity, tunnel-typed vanadium-based compounds with high power density, and NASICON-typed materials with stable frames and ideal thermal stability. In this review, the preparation methods, structural characteristics, electrochemical performance, energy storage mechanism, and various effective ways to improve the electrochemical performance of vanadium-based compounds are reviewed, including vanadium phosphates, vanadium oxides, vanadates, vanadium sulfides, VNs. The main challenges can be summarized as follows:

- 1) Although Li<sup>+</sup> (0.74 Å) and Zn<sup>2+</sup> (0.76 Å) have similar ionic radii, however, the electrostatic interaction between divalent Zn<sup>2+</sup> and cathode material framework is much stronger than that of Li<sup>+</sup>, and the larger zinc hydrate compounds is difficult to co-intercalation. Therefore, Zn<sup>2+</sup> diffuses slowly into the solid state of the cathode lattice.
- 2) Most layered vanadium-based compounds are composed of VO<sub>x</sub> layers with weak van der Waals interactions, which are prone to irreversible phase transitions and structural collapse during repeated Zn<sup>2+</sup> (de)intercalation, thus limiting cyclic stability.
- 3) Most vanadium-based compounds are soluble in acidic electrolyte solutions. Therefore, the dissociation and intercalation of H<sup>+</sup> are likely to lead to framework collapse and capacity decay during repeated cycles. Therefore, vanadium-based compounds have considerable structural instability, resulting in loss of active materials due to vanadium dissolution.

In order to overcome the above problems and realize the practical and large-scale applications of vanadium-based compounds in AZIBs, the following future research directions can be proposed:

- 1) The exploration of zinc storage mechanism is of great significance for the basic understanding of advanced AZIBs systems and their large-scale applications in the future. There are three kinds of conventional Zn<sup>2+</sup> (de)intercalation mechanisms based on vanadium-based compounds (Zn<sup>2+</sup> intercalation mechanism, H<sup>+</sup>/Zn<sup>2+</sup> co-intercalation mechanism, dual metal ion co-intercalation mechanism). However, it is still difficult to explain the zinc storage mechanism of vanadium-based compounds because of the lack of a reliable theoretical basis and advanced characterization techniques. Therefore, the development of more accurate characterization techniques combined with ab initio calculations will contribute to a better understanding of zinc storage mechanisms and the relationship between structure and properties, providing a good guide for understanding and designing more efficient AZIBs cathode materials.
- 2) The importance of electrolytes cannot be ignored. The solution of vanadium can be solved with a suitable electrolyte such as “water in salt” or Zn(CF<sub>3</sub>SO<sub>3</sub>)<sub>2</sub>. It is proved that the appropriate composition ratio in the multicomponent salt electrolyte can promote the (de)intercalation of Zn<sup>2+</sup> at the cathode-electrolyte interface by inhibiting water activity. The flexible choice of electrolyte types (e.g., gel, solid) offers the possibility for functionalized applications. However, how to balance interface stability, inhibition of side reactions with appropriate mobility, and energy storage media activity is the primary consideration in electrolyte design.
- 3) Hundreds of vanadium-based compounds with various tunnel or layer spacing structures have been discovered, and they are highly likely to be the preferred candidates for AZIBs. Therefore, it is an important research direction to study the synthesis route and zinc storage mechanism of suitable vanadium-based compounds. In addition, the pre-intercalation of cation, H<sub>2</sub>O molecules, and conductive organic polymers can reduce the strong electrostatic interaction between the V–O layer and the highly polarized Zn<sup>2+</sup>,



and then reduce the migration energy barrier of  $\text{Zn}^{2+}$ . Pre-intercalation is also an effective strategy to strengthen the layered structure of vanadium-based oxides, expand the interlayer spacing and avoid structural collapse. The cations (or/and  $\text{H}_2\text{O}$  molecules) pre-intercalate between the V–O layers and act as pillars to chemically strengthen the layers, improve structural stability and inhibit destructive structural changes. In addition to having the above functions, the pre-intercalation of conductive organic polymers can also be used as guest storage for  $\text{Zn}^{2+}$ . In order to enrich the members of the vanadium-based material family, more types of vanadium-based compounds containing the pre-intercalation of cations or/and conducting organic polymers should be developed.

- 4) In addition to the pre-intercalation strategy, there are also two attractive ways to stabilize the host structure and enhance the electrical conductivity, which is called surface composite and heteroatoms doping. In addition, defect engineering, such as the creation of oxygen vacancies, can further enhance the  $\text{Zn}^{2+}$  storage behavior of vanadium-based compounds for AZIBs by modulating the diffusion properties of electronic and ion diffusion by adsorbing  $\text{Zn}^{2+}$  on the surface of materials. Therefore, further development of surface engineering, heteroatom doping, and defect engineering are effective strategies to enhance the electronic conductivity of vanadium-based compounds and promote the migration of ions and electrons in cathode.
- 5) It is also an important approach to develop vanadium-based compounds with different morphology, including 1D, 2D nanostructures, and 3D nano/micro-structures, hollow/porous structures. The nanostructures with 1D micron dimensions can facilitate current collection. 2D nanostructures not only have the advantages of 1D nanostructures, but also are more conducive to ions or electrons transport due to their ultra-thin thickness. In addition, the highly exposed surface of 2D nanostructures can shorten the migration path of ions and provide more active sites for redox reactions. In summary, the nanostructure can inhibit volume change through local blank, thus achieving high structural stability and improving reversible capacity. However, reducing side reactions between cathode and electrolyte to achieve high cyclic stability remains a major challenge. 3D nano/micro-structures composed of nanostructures not only have the advantages of nanomaterials, but also have higher bulk density. In addition, hollow/porous structures generally offer more possibilities for improving electrochemical performance by buffering volume expansion, providing more active sites, and facilitating electrolyte penetration. Therefore, the construction of 3D hollow/porous nano/micro-structures may be an effective strategy to improve electrochemical performance, as this unique morphology can inhibit the agglomeration of nanostructures and regulate the volume changes during cycling. Therefore, precise structural designs with high surface area and abundant porosity can enhance electrochemical performance.

In addition to the above-existing problems and future prospects, the authors are suggested to pay more attention to the following problems in the process of experimental exploration:

- 1) A stable frame during cycling is a priority in selecting suitable vanadium-based compounds. Reversible changes in layer spacing have been observed in most studies, with water molecules or trapped cations playing a key role in stabilizing the crystal structure. The relationship between the electrolyte type and concentration, the solvation effect of  $\text{Zn}^{2+}$ , and the crystal structure of the vanadium-based compounds is inter-related and therefore requires further investigation. Changing any one of these three factors can lead to a different reaction process, which in turn affects the performance of AZIBs.
- 2) At high current densities, the GCD curves and CV responses in the first period sometimes differ from those in later periods. This may be related to the good self-regulation of the crystal structure in the first cycle to serve the rapid insertion/removal of zinc ions. This autoregulatory process may be related to the changes in V–O polyhedra and their connection types. A deeper understanding of this process is important to improve productivity and cycle performance.

In general, AZIBs have the advantages of safety, environmental protection, low toxicity, simple manufacturing, and so on. Compared with other battery systems, AZIBs have become one of the most promising battery systems in recent years. Although it may be too early to commercialize, the development of high-performance cathode materials could accelerate their commercialization process. Various vanadium-based compounds with low cost, high theoretical capacity, and high power density have been widely used as cathodes for AZIBs. In this review, the advantages and disadvantages of vanadium-based compounds are analyzed systematically as cathode materials, and the prospects of further development of vanadium-based compounds and AZIBs are put forward. With the continuous innovation of advanced characterization techniques and the discovery of new materials, the future commercialization challenges of low-cost AZIBs will be overcome one by one.

## Acknowledgements

This work was supported by the National Natural Science Foundation of China (No. NSFC-U1904215), Natural Science Foundation of Jiangsu Province (No. BK20200044), and Program for Young Changjiang Scholars of the Ministry of Education, China (No. Q2018270). The authors also acknowledge the Priority Academic Program Development of Jiangsu Higher Education Institutions and the technical support the authors received at the Testing Center of Yangzhou University.

## Conflict of Interest

The authors declare no conflict of interest.

## Keywords

aqueous zinc-ion batteries, cathode materials, vanadium-based compounds

Received: November 23, 2022  
Revised: December 29, 2022  
Published online: January 22, 2023

- [1] S. Chu, Y. Cui, N. Liu, *Nat. Mater.* **2017**, 16, 10.
- [2] B. Dunn, H. Kamath, J.-M. Tarascon, *Science* **2011**, 334, 928.
- [3] H. Wang, L. Chen, H. Pang, S. Kaskel, Q. Xu, *Chem. Soc. Rev.* **2020**, 49, 1414.
- [4] X. Xiao, L. Zou, H. Pang, Q. Xu, *Chem. Soc. Rev.* **2020**, 49, 301.
- [5] L. Hu, P. Xiao, L. Xue, H. Li, T. Zhai, *EnergyChem* **2021**, 3, 100052.
- [6] Y. Peng, Y. Bai, C. Liu, S. Cao, Q. Kong, H. Pang, *Coord. Chem. Rev.* **2022**, 466, 214602.
- [7] Y. Tang, S. Zheng, S. Cao, F. Yang, X. Guo, S. Zhang, H. Xue, H. Pang, *J. Colloid Interface Sci.* **2022**, 626, 1062.
- [8] H. B. Gray, *Nat. Chem.* **2009**, 1, 7.
- [9] H. Jin, C. Guo, X. Liu, J. Liu, A. Vasileff, Y. Jiao, Y. Zheng, S.-Z. Qiao, *Chem. Rev.* **2018**, 118, 6337.
- [10] Y. Cheng, H. Wang, T. Qian, C. Yan, *EnergyChem* **2022**, 4, 100074.
- [11] X. Wu, Y. Ru, Y. Bai, G. Zhang, Y. Shi, H. Pang, *Coord. Chem. Rev.* **2022**, 451, 214260.
- [12] S. Lei, Z. Liu, C. Liu, J. Li, B. Lu, S. Liang, J. Zhou, *Energy Environ. Sci.* **2022**, 15, 4911.
- [13] Y. Xu, Q. Li, H. Xue, H. Pang, *Coord. Chem. Rev.* **2018**, 376, 292.
- [14] Y. Yang, S. Bremner, C. Menictas, M. Kay, *Renewable Sustainable Energy Rev.* **2018**, 97, 109.
- [15] X. Li, X. Yang, H. Xue, H. Pang, Q. Xu, *EnergyChem* **2020**, 2, 100027.
- [16] J. Gu, Y. Peng, T. Zhou, J. Ma, H. Pang, Y. Yamauchi, *Nano Res. Energy* **2022**, 1, e9120009.
- [17] M. Li, T. Liu, X. Bi, Z. Chen, K. Amine, C. Zhong, J. Lu, *Chem. Soc. Rev.* **2020**, 49, 1688.
- [18] X. Ji, *Energy Environ. Sci.* **2019**, 12, 3203.
- [19] M. Du, Q. Li, Y. Zhao, C.-S. Liu, H. Pang, *Coord. Chem. Rev.* **2020**, 416, 213341.
- [20] S. Yang, F. Zhang, H. Ding, P. He, H. Zhou, *Joule* **2018**, 2, 1648.
- [21] F. Wan, Z. Niu, *Angew. Chem., Int. Ed.* **2019**, 58, 16358.
- [22] W. Wang, X. Zhu, L. Fu, *CCS Chem.* **2021**, 3, 686.
- [23] W. Song, S. Lee, G. Song, S. Park, *ACS Energy Lett.* **2019**, 4, 177.
- [24] Z. Liu, Y. Huang, Y. Huang, Q. Yang, X. Li, Z. Huang, C. Zhi, *Chem. Soc. Rev.* **2020**, 49, 180.
- [25] T. Chen, F. Wang, S. Cao, Y. Bai, S. Zheng, W. Li, S. Zhang, S. Hu, H. Pang, *Adv. Mater.* **2022**, 34, 2201779.
- [26] Y. Peng, J. Xu, J. Xu, J. Ma, Y. Bai, S. Cao, S. Zhang, H. Pang, *Adv. Colloid Interface Sci.* **2022**, 307, 102732.
- [27] K. Wu, J. Huang, J. Yi, X. Liu, Y. Liu, Y. Wang, J. Zhang, Y. Xia, *Adv. Energy Mater.* **2020**, 10, 1903977.
- [28] J. Ding, H. Gao, D. Ji, K. Zhao, S. Wang, F. Cheng, *J. Mater. Chem. A* **2021**, 9, 5258.
- [29] J. Tan, W. Zhu, Q. Gui, Y. Li, J. Liu, *Adv. Funct. Mater.* **2021**, 31, 2101027.
- [30] J. Yang, J. Cao, X. Zhao, K. Zhang, S. Zheng, Z. Gu, X. Wu, *Energy-Chem* **2022**, 4, 100092.
- [31] Y. Geng, L. Pan, Z. Peng, Z. Sun, H. Lin, C. Mao, L. Wang, L. Dai, H. Liu, K. Pan, X. Wu, Q. Zhang, Z. He, *Energy Storage Mater.* **2022**, 51, 733.
- [32] W. Li, J. R. Dahn, D. S. Wainwright, *Science* **1994**, 264, 1115.
- [33] Y. Liang, H. Dong, D. Aurbach, Y. Yao, *Nat. Energy* **2020**, 5, 646.
- [34] L. Ma, M. A. Schroeder, O. Borodin, T. P. Pollard, M. S. Ding, C. Wang, K. Xu, *Nat. Energy* **2020**, 5, 743.
- [35] X. Yuan, F. Ma, L. Zuo, J. Wang, N. Yu, Y. Chen, Y. Zhu, Q. Huang, R. Holze, Y. Wu, T. van Ree, *Electrochem. Energy Rev.* **2021**, 4, 1.
- [36] Y. Song, P. Ruan, C. Mao, Y. Chang, L. Wang, L. Dai, P. Zhou, B. Lu, J. Zhou, Z. He, *Nano-Micro Lett.* **2022**, 14, 218.
- [37] B. Tang, L. Shan, S. Liang, J. Zhou, *Energy Environ. Sci.* **2019**, 12, 3288.
- [38] G. Fang, J. Zhou, A. Pan, S. Liang, *ACS Energy Lett.* **2018**, 3, 2480.
- [39] H. Li, L. Ma, C. Han, Z. Wang, Z. Liu, Z. Tang, C. Zhi, *Nano Energy* **2019**, 62, 550.
- [40] X. Jia, C. Liu, Z. G. Neale, J. Yang, G. Cao, *Chem. Rev.* **2020**, 120, 7795.
- [41] C. Mao, Y. Chang, X. Zhao, X. Dong, Y. Geng, N. Zhang, L. Dai, X. Wu, L. Wang, Z. He, *J. Energy Chem.* **2022**, 75, 135.
- [42] M. Winter, R. J. Brodd, *Chem. Rev.* **2004**, 104, 4245.
- [43] T. Yamamoto, T. Shoji, *Inorg. Chim. Acta* **1986**, 117, L27.
- [44] J. F. Parker, J. S. Ko, D. R. Rolison, J. W. Long, *Joule* **2018**, 2, 2519.
- [45] C. Xu, B. Li, H. Du, F. Kang, *Angew. Chem., Int. Ed.* **2012**, 51, 933.
- [46] H. Pan, Y. Shao, P. Yan, Y. Cheng, K. S. Han, Z. Nie, C. Wang, J. Yang, X. Li, P. Bhattacharya, K. T. Mueller, J. Liu, *Nat. Energy* **2016**, 1, 16039.
- [47] T. Wei, Y. Liu, G. Yang, C. Wang, *Energy Storage Mater.* **2020**, 30, 130.
- [48] W. Deng, Z. Li, Y. Ye, Z. Zhou, Y. Li, M. Zhang, X. Yuan, J. Hu, W. Zhao, Z. Huang, C. Li, H. Chen, J. Zheng, R. Li, *Adv. Energy Mater.* **2021**, 11, 2003639.
- [49] T. Wu, Y. Lin, Z. Althouse, N. Liu, *ACS Appl. Energy Mater.* **2021**, 4, 12267.
- [50] M. Du, P. B. Geng, C. X. Pei, X. Y. Jiang, Y. Y. Shan, W. H. Hu, L. B. Ni, H. Pang, *Angew. Chem., Int. Ed.* **2022**, 61, e202209350.
- [51] P. Ruan, X. Xu, D. Zheng, X. Chen, X. Yin, S. Liang, X. Wu, W. Shi, X. Cao, J. Zhou, *ChemSusChem* **2022**, 15, 202201118.
- [52] Y. Zhao, Y. Zhu, X. Zhang, *InfoMat* **2020**, 2, 237.
- [53] Y. Li, D. Zhang, S. Huang, H. Y. Yang, *Nano Energy* **2021**, 85, 105969.
- [54] K. Hurlbutt, S. Wheeler, I. Capone, M. Pasta, *Joule* **2018**, 2, 1950.
- [55] C. Xu, Z. Yang, X. Zhang, M. Xia, H. Yan, J. Li, H. Yu, L. Zhang, J. Shu, *Nano-Micro Lett.* **2021**, 13, 187.
- [56] B. Yong, D. Ma, Y. Wang, H. Mi, C. He, P. Zhang, *Adv. Energy Mater.* **2020**, 10, 2002354.
- [57] L. Wu, Y. Dong, *Energy Storage Mater.* **2021**, 41, 715.
- [58] T. Zhou, L. Zhu, L. Xie, Q. Han, X. Yang, L. Chen, G. Wang, X. Cao, *J. Colloid Interface Sci.* **2022**, 605, 828.
- [59] D. Kundu, B. D. Adams, V. Duffort, S. H. Vajargah, L. F. Nazar, *Nat. Energy* **2016**, 1, 16119.
- [60] J. Ding, Z. Du, L. Gu, B. Li, L. Wang, S. Wang, Y. Gong, S. Yang, *Adv. Mater.* **2018**, 30, 1800762.
- [61] M. Yan, P. He, Y. Chen, S. Wang, Q. Wei, K. Zhao, X. Xu, Q. An, Y. Shuang, Y. Shao, K. T. Mueller, L. Mai, J. Liu, J. Yang, *Adv. Mater.* **2018**, 30, 1703725.
- [62] F. Wan, L. Zhang, X. Dai, X. Wang, Z. Niu, J. Chen, *Nat. Commun.* **2018**, 9, 1656.
- [63] X. Chen, H. Zhang, J.-H. Liu, Y. Gao, X. Cao, C. Zhan, Y. Wang, S. Wang, S.-L. Chou, S.-X. Dou, D. Cao, *Energy Storage Mater.* **2022**, 50, 21.
- [64] T. Yi, L. Qiu, J.-P. Qu, H. Liu, J. Zhang, Y. Zhu, *Coord. Chem. Rev.* **2021**, 446, 214124.
- [65] T. Lv, G. Zhu, S. Dong, Q. Kong, Y. Peng, S. Jiang, G. Zhang, Z. Yang, S. Yang, X. Dong, H. Pang, Y. Zhang, *Angew. Chem., Int. Ed.* **2022**, 202216089.
- [66] H. Tang, Z. Peng, L. Wu, F. Xiong, C. Pei, Q. An, L. Mai, *Electrochem. Energy Rev.* **2018**, 1, 169.
- [67] S. Liu, L. Kang, J. M. Kim, Y. T. Chun, J. Zhang, S. C. Jun, *Adv. Energy Mater.* **2020**, 10, 2000477.
- [68] Y. Zhang, A. Chen, J. Sun, *J. Energy Chem.* **2021**, 54, 655.
- [69] T. Lv, X. Luo, G. Yuan, S. Yang, H. Pang, *Chem. Eng. J.* **2022**, 428, 131211.
- [70] M. Tamilselvan, T. V. M. Sreekanth, K. Yoo, J. Kim, *Appl. Surf. Sci.* **2020**, 529, 147077.
- [71] S. Zhang, H. Tan, X. Rui, Y. Yu, *Acc. Chem. Res.* **2020**, 53, 1660.
- [72] X. Wang, Z. Zhang, B. Xi, W. Chen, Y. Jia, J. Feng, S. Xiong, *ACS Nano* **2021**, 15, 9244.
- [73] M. Li, Z. Li, X. Wang, J. Meng, X. Liu, B. Wu, C. Han, L. Mai, *Energy Environ. Sci.* **2021**, 14, 3796.
- [74] A. Liu, F. Wu, Y. Zhang, J. Zhou, Y. Zhou, M. Xie, *Small* **2022**, 18, 2201011.

- [75] D. Wang, Q. Li, Y. Zhao, H. Hong, H. Li, Z. Huang, G. Liang, Q. Yang, C. Zhi, *Adv. Energy Mater.* **2022**, 12, 2102707.
- [76] X. Wang, B. Xi, X. Ma, Z. Feng, Y. Jia, J. Feng, Y. Qian, S. Xiong, *Nano Lett.* **2020**, 20, 2899.
- [77] D. Chen, M. Lu, B. Wang, R. Chai, L. Li, D. Cai, H. Yang, B. Liu, Y. Zhang, W. Han, *Energy Storage Mater.* **2021**, 35, 679.
- [78] C. Li, W. Wu, H.-Y. Shi, Z. Qin, D. Yang, X. Yang, Y. Song, D. Guo, X.-X. Liu, X. Sun, *Chem. Commun.* **2021**, 57, 6253.
- [79] X. Li, Z. Chen, Y. Yang, S. Liang, B. Lu, J. Zhou, *Inorg. Chem. Front.* **2022**, 9, 3986.
- [80] Y. Zhu, L. Peng, D. Chen, G. Yu, *Nano Lett.* **2016**, 16, 742.
- [81] Y. Jiang, Q. Zou, S. Liu, H. Zeng, L. Chen, Y. Xiang, J. Li, X. Wu, J. Wu, L. Xiong, *J. Electroanal. Chem.* **2021**, 900, 115685.
- [82] F. Wan, Y. Zhang, L. Zhang, D. Liu, C. Wang, L. Song, Z. Niu, J. Chen, *Angew. Chem., Int. Ed.* **2019**, 58, 7062.
- [83] H. Li, L. Peng, Y. Zhu, D. Chen, X. Zhang, G. Yu, *Energy Environ. Sci.* **2016**, 9, 3399.
- [84] H. Tietze, *Aust. J. Chem.* **1981**, 34, 2035.
- [85] F. Wang, W. Sun, Z. Shadik, E. Hu, X. Ji, T. Gao, X.-Q. Yang, K. Xu, C. Wang, *Angew. Chem., Int. Ed.* **2018**, 57, 11978.
- [86] Z. Wu, C. Lu, F. Ye, L. Zhang, L. Jiang, Q. Liu, H. Dong, Z. Sun, L. Hu, *Adv. Funct. Mater.* **2021**, 31, 2106816.
- [87] H. Shi, Y. Song, Z. Qin, C. Li, D. Guo, X. Liu, X. Sun, *Angew. Chem., Int. Ed.* **2019**, 58, 16057.
- [88] J. Huang, Z. Wang, M. Hou, X. Dong, Y. Liu, Y. Wang, Y. Xia, *Nat. Commun.* **2018**, 9, 2906.
- [89] M. J. Park, H. Yaghoobnejad Asl, S. Therese, A. Manthiram, *J. Mater. Chem. A* **2019**, 7, 7159.
- [90] K. Zhu, Z. Sun, P. Liu, H. Li, Y. Wang, K. Cao, L. Jiao, *J. Energy Chem.* **2021**, 63, 239.
- [91] Z. Wu, Y. Wang, L. Zhang, L. Jiang, W. Tian, C. Cai, J. Price, Q. Gu, L. Hu, *ACS Appl. Energy Mater.* **2020**, 3, 3919.
- [92] L. Hu, Z. Wu, C. Lu, F. Ye, Q. Liu, Z. Sun, *Energy Environ. Sci.* **2021**, 14, 4095.
- [93] V. Verma, S. Kumar, W. Manalastas, J. Zhao, R. Chua, S. Meng, P. Kidkhunthod, M. Srinivasan, *ACS Appl. Energy Mater.* **2019**, 2, 8667.
- [94] Z. Jian, W. Han, X. Lu, H. Yang, Y.-S. Hu, J. Zhou, Z. Zhou, J. Li, W. Chen, D. Chen, L. Chen, *Adv. Energy Mater.* **2013**, 3, 156.
- [95] J. Zhang, Y. Fang, L. Xiao, J. Qian, Y. Cao, X. Ai, H. Yang, *ACS Appl. Mater. Interfaces* **2017**, 9, 7177.
- [96] Q. Zheng, H. Yi, X. Li, H. Zhang, *J. Energy Chem.* **2018**, 27, 1597.
- [97] H. Tan, L. Xu, H. Geng, X. Rui, C. Li, S. Huang, *Small* **2018**, 14, 1800567.
- [98] J. Liao, Y. Han, Z. Zhang, J. Xu, J. Li, X. Zhou, *Energy Environ. Mater.* **2021**, 4, 178.
- [99] M. Liang, L. Li, X. Cui, S. Qi, L. Wang, H. Dong, X. Chen, Y. Wang, S. Chen, G. Wang, *Small* **2022**, 18, 2202151.
- [100] Q. Zhou, L. Wang, W. Li, S. Zeng, K. Zhao, Y. Yang, Q. Wu, M. Liu, Q. Huang, J. Zhang, X. Sun, *ACS Appl. Mater. Interfaces* **2021**, 13, 25036.
- [101] T. Jenkins, J. A. Alarco, B. Cowie, I. D. R. Mackinnon, *ACS Appl. Mater. Interfaces* **2021**, 13, 45505.
- [102] G. Li, Z. Yang, Y. Jiang, C. Jin, W. Huang, X. Ding, Y. Huang, *Nano Energy* **2016**, 25, 211.
- [103] J. Gaubicher, C. Wurm, G. Goward, C. Masquelier, L. Nazar, *Chem. Mater.* **2000**, 12, 3240.
- [104] D. Morgan, G. Ceder, Saïdi, J. Barker, J. Swoyer, H. Huang, G. Adamson, *Chem. Mater.* **2002**, 14, 4684.
- [105] S.-C. Yin, H. Grondy, P. Strobel, M. Anne, L. F. Nazar, *J. Am. Chem. Soc.* **2003**, 125, 10402.
- [106] X. Rui, Q. Yan, M. Skyllas-Kazacos, T. M. Lim, *J. Power Sources* **2014**, 258, 19.
- [107] H. Zhao, C. J. Hu, H. Cheng, J. Fang, Y. Xie, W. Fang, T. N. L. Doan, T. K. A. Hoang, J. Xu, P. Chen, *Sci. Rep.* **2016**, 6, 25809.
- [108] C. Li, W. Yuan, C. Li, H. Wang, L. Wang, Y. Liu, N. Zhang, *Chem. Commun.* **2021**, 57, 4319.
- [109] C. Li, R. Kingsbury, L. Zhou, A. Shyamsunder, K. A. Persson, L. F. Nazar, *ACS Energy Lett.* **2022**, 7, 533.
- [110] N. Anantharamulu, K. Koteswara Rao, G. Rambabu, B. Vijaya Kumar, V. Radha, M. Vithal, *J. Mater. Sci.* **2011**, 46, 2821.
- [111] S. Y. Lim, H. Kim, R. A. Shakoore, Y. Jung, J. W. Choi, *J. Electrochem. Soc.* **2012**, 159, A1393.
- [112] G. Li, Z. Yang, Y. Jiang, W. Zhang, Y. Huang, *J. Power Sources* **2016**, 308, 52.
- [113] Q. Li, K. Ma, C. Hong, G. Yang, C. Wang, *Sci. China Mater.* **2021**, 64, 1386.
- [114] P. Hu, T. Zhu, X. Wang, X. Zhou, X. Wei, X. Yao, W. Luo, C. Shi, K. A. Owusu, L. Zhou, L. Mai, *Nano Energy* **2019**, 58, 492.
- [115] X. Lin, G. Zhou, J. Liu, M. J. Robson, J. Yu, Y. Wang, Z. Zhang, S. C. T. Kwok, F. Ciucci, *Adv. Funct. Mater.* **2021**, 31, 2105717.
- [116] X. Rui, D. Sim, K. Wong, J. Zhu, W. Liu, C. Xu, H. Tan, N. Xiao, H. Hng, T. M. Lim, Q. Yan, *J. Power Sources* **2012**, 214, 171.
- [117] X. Rui, W. Sun, C. Wu, Y. Yu, Q. Yan, *Adv. Mater.* **2015**, 27, 6670.
- [118] R. Rajagopalan, Y. Tang, X. Ji, C. Jia, H. Wang, *Adv. Funct. Mater.* **2020**, 30, 1909486.
- [119] W. Song, Z. Wu, J. Chen, Q. Lan, Y. Zhu, Y. Yang, C. Pan, H. Hou, M. Jing, X. Ji, *Electrochim. Acta* **2014**, 146, 142.
- [120] Y. Niu, Y. Zhang, M. Xu, *J. Mater. Chem. A* **2019**, 7, 15006.
- [121] R. A. Shakoore, D.-H. Seo, H. Kim, Y.-U. Park, J. Kim, S.-W. Kim, H. Gwon, S. Lee, K. Kang, *J. Mater. Chem.* **2012**, 22, 20535.
- [122] L. Zhu, H. Wang, D. Sun, Y. Tang, H. Wang, *J. Mater. Chem. A* **2020**, 8, 21387.
- [123] M. Bianchini, N. Brisset, F. Fauth, F. Weill, E. Elkaim, E. Suard, C. Masquelier, L. Croguennec, *Chem. Mater.* **2014**, 26, 4238.
- [124] W. Li, K. Wang, S. Cheng, K. Jiang, *Energy Storage Mater.* **2018**, 15, 14.
- [125] M. J. Park, A. Manthiram, *ACS Appl. Energy Mater.* **2020**, 3, 5015.
- [126] B. Wang, J. Yan, Y. Zhang, M. Ye, Y. Yang, C. C. Li, *Adv. Funct. Mater.* **2021**, 31, 2102827.
- [127] Y.-U. Park, D.-H. Seo, H.-S. Kwon, B. Kim, J. Kim, H. Kim, I. Kim, H.-I. Yoo, K. Kang, *J. Am. Chem. Soc.* **2013**, 135, 13870.
- [128] Q. Ni, H. Jiang, S. Sandstrom, Y. Bai, H. Ren, X. Wu, Q. Guo, D. Yu, C. Wu, X. Ji, *Adv. Funct. Mater.* **2020**, 30, 2003511.
- [129] H. Gao, J. B. Goodenough, *Angew. Chem., Int. Ed.* **2016**, 55, 12768.
- [130] T. Zhu, P. Hu, X. Wang, Z. Liu, W. Luo, K. A. Owusu, W. Cao, C. Shi, J. Li, L. Zhou, L. Mai, *Adv. Energy Mater.* **2019**, 9, 1803436.
- [131] T. Zhu, P. Hu, C. Cai, Z. Liu, G. Hu, Q. Kuang, L. Mai, L. Zhou, *Nano Energy* **2020**, 70, 104548.
- [132] H. Li, M. Xu, C. Gao, W. Zhang, Z. Zhang, Y. Lai, L. Jiao, *Energy Storage Mater.* **2020**, 26, 325.
- [133] Y. Zhou, Z. Zhang, Y. Zhao, J. Liu, K. Lam, X. Zheng, H. Lou, X. Hou, *Chem. Eng. J.* **2021**, 425, 130459.
- [134] X. Li, F. Ning, L. Luo, J. Wu, Y. Xiang, X. Wu, L. Xiong, X. Peng, *RSC Adv.* **2022**, 12, 8394.
- [135] J. S. Ko, P. P. Paul, G. Wan, N. Seitzman, R. H. DeBlock, B. S. Dunn, M. F. Toney, J. Nelson Weker, *Chem. Mater.* **2020**, 32, 3028.
- [136] G. Guo, X. Tan, K. Wang, H. Zhang, *ChemSusChem* **2022**, 15, 202200313.
- [137] Y. Yan, B. Li, W. Guo, H. Pang, H. Xue, *J. Power Sources* **2016**, 329, 148.
- [138] H. Huang, T. Tian, L. Pan, X. Chen, E. Tervoort, C.-J. Shih, M. Niederberger, *J. Mater. Chem. A* **2019**, 7, 16109.
- [139] Y. Liu, X. Wu, *J. Energy Chem.* **2021**, 56, 223.
- [140] X. Xu, F. Xiong, J. Meng, X. Wang, C. Niu, Q. An, L. Mai, *Adv. Funct. Mater.* **2020**, 30, 1904398.
- [141] Y. Ding, Y. Wen, C. Wu, P. A. van Aken, J. Maier, Y. Yu, *Nano Lett.* **2015**, 15, 1388.



- [142] S. Lee, K. Hippalgaonkar, F. Yang, J. Hong, C. Ko, J. Suh, K. Liu, K. Wang, J. J. Urban, X. Zhang, C. Dames, S. A. Hartnoll, O. Delaire, J. Wu, *Science* **2017**, 355, 371.
- [143] S. Lee, I. N. Ivanov, J. K. Keum, H. N. Lee, *Sci. Rep.* **2016**, 6, 19621.
- [144] J.-S. Park, J. H. Jo, Y. Aniskevich, A. Bakavets, G. Ragoisha, E. Streltsov, J. Kim, S.-T. Myung, *Chem. Mater.* **2018**, 30, 6777.
- [145] L. Chen, Y. Ruan, G. Zhang, Q. Wei, Y. Jiang, T. Xiong, P. He, W. Yang, M. Yan, Q. An, L. Mai, *Chem. Mater.* **2019**, 31, 699.
- [146] Z. Li, Y. Ren, L. Mo, C. Liu, K. Hsu, Y. Ding, X. Zhang, X. Li, L. Hu, D. Ji, G. Cao, *ACS Nano* **2020**, 14, 5581.
- [147] T. Wei, Q. Li, G. Yang, C. Wang, *J. Mater. Chem. A* **2018**, 6, 8006.
- [148] L. Zhang, L. Chen, X. Zhou, Z. Liu, *Adv. Energy Mater.* **2015**, 5, 1400930.
- [149] P. He, M. Yan, G. Zhang, R. Sun, L. Chen, Q. An, L. Mai, *Adv. Energy Mater.* **2017**, 7, 1601920.
- [150] L. Chen, Z. Yang, Y. Huang, *Nanoscale* **2019**, 11, 13032.
- [151] R. M. Wentzcovitch, W. W. Schulz, P. B. Allen, *Phys. Rev. Lett.* **1994**, 72, 3389.
- [152] J. Ni, W. Jiang, K. Yu, F. Sun, Z. Zhu, *Cryst. Res. Technol.* **2011**, 46, 507.
- [153] L. Zhang, L. Miao, B. Zhang, J. Wang, J. Liu, Q. Tan, H. Wan, J. Jiang, *J. Mater. Chem. A* **2020**, 8, 1731.
- [154] L. Jiang, Y. Qu, Z. Ren, P. Yu, D. Zhao, W. Zhou, L. Wang, H. Fu, *ACS Appl. Mater. Interfaces* **2015**, 7, 1595.
- [155] T. Jin, H. Li, Y. Li, L. Jiao, J. Chen, *Nano Energy* **2018**, 50, 462.
- [156] Y. Ding, Y. Peng, S. Chen, X. Zhang, Z. Li, L. Zhu, L.-E. Mo, L. Hu, *ACS Appl. Mater. Interfaces* **2019**, 11, 44109.
- [157] H. Luo, B. Wang, F. Wang, J. Yang, F. Wu, Y. Ning, Y. Zhou, D. Wang, H. Liu, S. Dou, *ACS Nano* **2020**, 14, 7328.
- [158] S. Deng, Z. Yuan, Z. Tie, C. Wang, L. Song, Z. Niu, *Angew. Chem., Int. Ed.* **2020**, 59, 22002.
- [159] J. Ding, H. Zheng, H. Gao, Q. Liu, Z. Hu, L. Han, S. Wang, S. Wu, S. Fang, S. Chou, *Adv. Energy Mater.* **2021**, 11, 2100973.
- [160] N. Zhang, F. Cheng, Y. Liu, Q. Zhao, K. Lei, C. Chen, X. Liu, J. Chen, *J. Am. Chem. Soc.* **2016**, 138, 12894.
- [161] K. Hu, D. Jin, Y. Zhang, L. Ke, H. Shang, Y. Yan, H. Lin, K. Rui, J. Zhu, *J. Energy Chem.* **2021**, 61, 594.
- [162] R. Chen, R. Luo, Y. Huang, F. Wu, L. Li, *Adv. Sci.* **2016**, 3, 1600051.
- [163] M. S. Javed, S. S. A. Shah, T. Najam, S. H. Siyal, S. Hussain, M. Saleem, Z. Zhao, W. Mai, *Nano Energy* **2020**, 77, 105276.
- [164] D. Chen, X. Rui, Q. Zhang, H. Geng, L. Gan, W. Zhang, C. Li, S. Huang, Y. Yu, *Nano Energy* **2019**, 60, 171.
- [165] N. Zhang, Y. Dong, M. Jia, X. Bian, Y. Wang, M. Qiu, J. Xu, Y. Liu, L. Jiao, F. Cheng, *ACS Energy Lett.* **2018**, 3, 1366.
- [166] J. Zhou, L. Shan, Z. Wu, X. Guo, G. Fang, S. Liang, *Chem. Commun.* **2018**, 54, 4457.
- [167] Y. Li, Z. Huang, P. K. Kalambate, Y. Zhong, Z. Huang, M. Xie, Y. Shen, Y. Huang, *Nano Energy* **2019**, 60, 752.
- [168] X. Chen, L. Wang, H. Li, F. Cheng, J. Chen, *J. Energy Chem.* **2019**, 38, 20.
- [169] M. S. Javed, H. Lei, Z. Wang, B. Liu, X. Cai, W. Mai, *Nano Energy* **2020**, 70, 104573.
- [170] F. Liu, Z. Chen, G. Fang, Z. Wang, Y. Cai, B. Tang, J. Zhou, S. Liang, *Nano-Micro Lett.* **2019**, 11, 25.
- [171] M. Song, H. Tan, D. Chao, H. J. Fan, *Adv. Funct. Mater.* **2018**, 28, 1802564.
- [172] L. Fan, Y. Ru, H. Xue, H. Pang, Q. Xu, *Adv. Sustainable Syst.* **2020**, 4, 2000178.
- [173] J. Zhang, S. Wei, H. Wang, H. Liu, Y. Zhang, S. Liu, Z. Wang, X. Lu, *ChemSusChem* **2021**, 14, 2076.
- [174] L. Xiong, Z. Qu, Z. Shen, G. Yuan, G. Wang, B. Wang, H. Wang, J. Bai, *J. Colloid Interface Sci.* **2022**, 615, 184.
- [175] N. Xu, C. Yan, W. He, L. Xu, Z. Jiang, A. Zheng, H. Wu, M. Chen, G. Diao, *J. Power Sources* **2022**, 533, 231358.
- [176] H. Li, P. He, Y. Wang, E. Hosono, H. Zhou, *J. Mater. Chem.* **2011**, 21, 10999.
- [177] W. Meng, R. Pigliapochi, P. M. Bayley, O. Pecher, M. W. Gaultois, I. D. Seymour, H.-P. Liang, W. Xu, K. M. Wiaderek, K. W. Chapman, C. P. Grey, *Chem. Mater.* **2017**, 29, 5513.
- [178] N. A. Chernova, M. Roppolo, A. C. Dillon, M. S. Whittingham, *J. Mater. Chem.* **2009**, 19, 2526.
- [179] J. Shin, D. S. Choi, H. J. Lee, Y. Jung, J. W. Choi, *Adv. Energy Mater.* **2019**, 9, 1900083.
- [180] L. Shan, J. Zhou, W. Zhang, C. Xia, S. Guo, X. Ma, G. Fang, X. Wu, S. Liang, *Energy Technol.* **2019**, 7, 1900022.
- [181] Y. Lin, F. Zhou, M. Xie, S. Zhang, C. Deng, *ChemSusChem* **2020**, 13, 3696.
- [182] X. Wang, L. Ye, Y. Zou, L. Zhao, Q. Jiang, *Mater. Today Energy* **2021**, 19, 100593.
- [183] Y. Liu, G. Yuan, X. Wang, J. Liu, Q. Zeng, X. Guo, H. Wang, C. Liu, H. Pang, *Chem. Eng. J.* **2022**, 428, 132538.
- [184] F. Lei, Y. Sun, K. Liu, S. Gao, L. Liang, B. Pan, Y. Xie, *J. Am. Chem. Soc.* **2014**, 136, 6826.
- [185] S. Gao, X. Jiao, Z. Sun, W. Zhang, Y. Sun, C. Wang, Q. Hu, X. Zu, F. Yang, S. Yang, L. Liang, J. Wu, Y. Xie, *Angew. Chem., Int. Ed.* **2016**, 55, 698.
- [186] B. Tian, W. Tang, C. Su, Y. Li, *ACS Appl. Mater. Interfaces* **2018**, 10, 642.
- [187] T. Wu, K. Zhu, C. Qin, K. Huang, *J. Mater. Chem. A* **2019**, 7, 5612.
- [188] H. Wang, X. Bi, Y. Bai, C. Wu, S. Gu, S. Chen, F. Wu, K. Amine, J. Lu, *Adv. Energy Mater.* **2017**, 7, 1602720.
- [189] A. Moretti, S. Passerini, *Adv. Energy Mater.* **2016**, 6, 1600868.
- [190] W. Zhang, C. Zuo, C. Tang, W. Tang, B. Lan, X. Fu, S. Dong, P. Luo, *Energy Technol.* **2021**, 9, 2000789.
- [191] J. Huang, X. Guo, X. Lin, Y. Zhu, B. Zhang, *Research* **2019**, 2019, 1021368.
- [192] M. Yang, Z. Wang, H. Ben, M. Zhao, J. Luo, D. Chen, Z. Lu, L. Wang, C. Liu, *J. Colloid Interface Sci.* **2022**, 607, 68.
- [193] Y. Zhang, L. Xu, H. Jiang, Y. Liu, C. Meng, *J. Colloid Interface Sci.* **2021**, 603, 641.
- [194] J. Zeng, Z. Zhang, X. Guo, G. Li, *J. Mater. Chem. A* **2019**, 7, 21079.
- [195] M. Wang, J. Zhang, L. Zhang, J. Li, W. Wang, Z. Yang, L. Zhang, Y. Wang, J. Chen, Y. Huang, D. Mitlin, X. Li, *ACS Appl. Mater. Interfaces* **2020**, 12, 31564.
- [196] Z. Feng, J. Sun, Y. Liu, H. Jiang, T. Hu, M. Cui, F. Tian, C. Meng, Y. Zhang, *J. Power Sources* **2022**, 536, 231489.
- [197] H. Tang, N. Xu, C. Pei, F. Xiong, S. Tan, W. Luo, Q. An, L. Mai, *ACS Appl. Mater. Interfaces* **2017**, 9, 28667.
- [198] M. Rastgoo-Deylami, M. S. Chae, S.-T. Hong, *Chem. Mater.* **2018**, 30, 7464.
- [199] Y. Zhang, X. Liu, G. Xie, L. Yu, S. Yi, M. Hu, C. Huang, *Mater. Sci. Eng. B* **2010**, 175, 164.
- [200] Q. Pang, C. Sun, Y. Yu, K. Zhao, Z. Zhang, P. M. Voyles, G. Chen, Y. Wei, X. Wang, *Adv. Energy Mater.* **2018**, 8, 1800144.
- [201] D. Chen, M. Lu, B. Wang, H. Cheng, H. Yang, D. Cai, W. Han, H. J. Fan, *Nano Energy* **2021**, 83, 105835.
- [202] H. Cao, Z. Zheng, P. Norby, X. Xiao, S. Mossin, *Small* **2021**, 17, 2100558.
- [203] N. Zhang, M. Jia, Y. Dong, Y. Wang, J. Xu, Y. Liu, L. Jiao, F. Cheng, *Adv. Funct. Mater.* **2019**, 29, 1807331.
- [204] J. Huang, H. Liang, Y. Tang, B. Lu, J. Zhou, S. Liang, *Adv. Energy Mater.* **2022**, 12, 2201434.
- [205] J. Lai, H. Zhu, X. Zhu, H. Koritala, Y. Wang, *ACS Appl. Energy Mater.* **2019**, 2, 1988.
- [206] T. Wei, Q. Li, G. Yang, C. Wang, *Electrochim. Acta* **2018**, 287, 60.
- [207] Y. Tang, X. Rui, Y. Zhang, T. M. Lim, Z. Dong, H. H. Hng, X. Chen, Q. Yan, Z. Chen, *J. Mater. Chem. A* **2013**, 1, 82.
- [208] T. Wei, G. Yang, C. Wang, *ACS Appl. Mater. Interfaces* **2019**, 11, 20888.

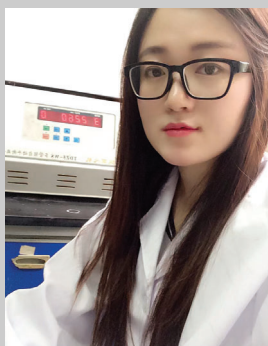
- [209] W. Wu, S. Wang, C. Zhang, S. Hou, L. Zhang, *ACS Appl. Mater. Interfaces* **2021**, 13, 18704.
- [210] Y. Xu, K. Sheng, C. Li, G. Shi, *ACS Nano* **2010**, 4, 4324.
- [211] Z. Chen, W. Ren, L. Gao, B. Liu, S. Pei, H.-M. Cheng, *Nat. Mater.* **2011**, 10, 424.
- [212] Y. Zhao, C. Hu, Y. Hu, H. Cheng, G. Shi, L. Qu, *Angew. Chem., Int. Ed.* **2012**, 51, 11371.
- [213] H. Hu, Z. Zhao, W. Wan, Y. Gogotsi, J. Qiu, *Adv. Mater.* **2013**, 25, 2219.
- [214] J. Zhu, L. Cao, Y. Wu, Y. Gong, Z. Liu, H. E. Hoster, Y. Zhang, S. Zhang, S. Yang, Q. Yan, P. M. Ajayan, R. Vajtai, *Nano Lett.* **2013**, 13, 5408.
- [215] H. Sun, Z. Xu, C. Gao, *Adv. Mater.* **2013**, 25, 2554.
- [216] Z. Li, S. Ganapathy, Y. Xu, Z. Zhou, M. Sarilar, M. Wagemaker, *Adv. Energy Mater.* **2019**, 9, 1900237.
- [217] Y. Liu, T. Lv, H. Wang, X. Guo, C. Liu, H. Pang, *Chem. Eng. J.* **2021**, 417, 128408.
- [218] Y. Liu, P. Hu, H. Liu, X. Wu, C. Zhi, *Mater. Today Energy* **2020**, 17, 100431.
- [219] F. Cui, J. Zhao, D. Zhang, Y. Fang, F. Hu, K. Zhu, *Chem. Eng. J.* **2020**, 390, 124118.
- [220] Z. Zhang, B. Xi, X. Wang, X. Ma, W. Chen, J. Feng, S. Xiong, *Adv. Funct. Mater.* **2021**, 31, 2103070.
- [221] H. Zhang, Z. Yao, D. Lan, Y. Liu, L. Ma, J. Cui, *J. Alloys Compd.* **2021**, 861, 158560.
- [222] P. Hu, M. Yan, T. Zhu, X. Wang, X. Wei, J. Li, L. Zhou, Z. Li, L. Chen, L. Mai, *ACS Appl. Mater. Interfaces* **2017**, 9, 42717.
- [223] Z. Qi, T. Xiong, T. Chen, W. Shi, M. Zhang, Z. W. J. Ang, H. Fan, H. Xiao, W. S. V. Lee, J. Xue, *J. Alloys Compd.* **2021**, 870, 159403.
- [224] J. Cao, D. Zhang, Y. Yue, T. Pakornchote, T. Bovornratanaraks, M. Sawangphruk, X. Zhang, J. Qin, *Mater. Today Energy* **2021**, 21, 100824.
- [225] C. Liu, R. Li, W. Liu, G. Shen, D. Chen, *ACS Appl. Mater. Interfaces* **2021**, 13, 37194.
- [226] S. Wu, S. Liu, L. Hu, S. Chen, *J. Alloys Compd.* **2021**, 878, 160324.
- [227] Y. Shao, J. Zeng, J. Li, H. Ren, Z. Zhang, J. Liu, C. Mao, X. Guo, G. Li, *ChemElectroChem* **2021**, 8, 1784.
- [228] Z. Cao, H. Chu, H. Zhang, Y. Ge, R. Clemente, P. Dong, L. Wang, J. Shen, M. Ye, P. M. Ajayan, *J. Mater. Chem. A* **2019**, 7, 25262.
- [229] X. Li, L. Ma, Y. Zhao, Q. Yang, D. Wang, Z. Huang, G. Liang, F. Mo, Z. Liu, C. Zhi, *Mater. Today Energy* **2019**, 14, 100361.
- [230] C. Liu, W. Xu, C. Mei, M.-C. Li, X. Xu, Q. Wu, *Chem. Eng. J.* **2021**, 405, 126737.
- [231] T. Wei, Q. Li, G. Yang, C. Wang, *Adv. Energy Mater.* **2019**, 9, 1901480.
- [232] H. Yan, Q. Ru, P. Gao, S. Cheng, F. Chen, F. C.-C. Ling, L. Wei, *Energy Technol.* **2020**, 8, 1901105.
- [233] P. He, J. Liu, X. Zhao, Z. Ding, P. Gao, L.-Z. Fan, *J. Mater. Chem. A* **2020**, 8, 10370.
- [234] M. Liao, J. Wang, L. Ye, H. Sun, Y. Wen, C. Wang, X. Sun, B. Wang, H. Peng, *Angew. Chem., Int. Ed.* **2020**, 59, 2273.
- [235] Y. Lin, F. Zhou, M. Chen, S. Zhang, C. Deng, *Chem. Eng. J.* **2020**, 396, 125259.
- [236] M. Liao, J. Wang, L. Ye, H. Sun, P. Li, C. Wang, C. Tang, X. Cheng, B. Wang, H. Peng, *J. Mater. Chem. A* **2021**, 9, 6811.
- [237] W. Shi, B. Yin, Y. Yang, M. B. Sullivan, J. Wang, Y.-W. Zhang, Z. G. Yu, W. S. V. Lee, J. Xue, *ACS Nano* **2021**, 15, 1273.
- [238] W. Liu, L. Dong, B. Jiang, Y. Huang, X. Wang, C. Xu, Z. Kang, J. Mou, F. Kang, *Electrochim. Acta* **2019**, 320, 134565.
- [239] M. Clites, J. L. Hart, M. L. Taheri, E. Pomerantseva, *ACS Energy Lett.* **2018**, 3, 562.
- [240] Y. Yang, Y. Tang, S. Liang, Z. Wu, G. Fang, X. Cao, C. Wang, T. Lin, A. Pan, J. Zhou, *Nano Energy* **2019**, 61, 617.
- [241] M. H. Alfaruqi, V. Mathew, J. Song, S. Kim, S. Islam, D. T. Pham, J. Jo, S. Kim, J. P. Baboo, Z. Xiu, K.-S. Lee, Y.-K. Sun, J. Kim, *Chem. Mater.* **2017**, 29, 1684.
- [242] Y. Ran, J. Ren, Y. Kong, B. Wang, X. Xiao, Y. Wang, *Electrochim. Acta* **2022**, 412, 140120.
- [243] S. Liang, J. Zhou, G. Fang, J. Liu, Y. Tang, X. Li, A. Pan, *ACS Appl. Mater. Interfaces* **2013**, 5, 8704.
- [244] Y. Dong, S. Li, K. Zhao, C. Han, W. Chen, B. Wang, L. Wang, B. Xu, Q. Wei, L. Zhang, X. Xu, L. Mai, *Energy Environ. Sci.* **2015**, 8, 1267.
- [245] S. Yuan, Y.-B. Liu, D. Xu, D.-L. Ma, S. Wang, X.-H. Yang, Z.-Y. Cao, X.-B. Zhang, *Adv. Sci.* **2015**, 2, 1400018.
- [246] Y. Cai, F. Liu, Z. Luo, G. Fang, J. Zhou, A. Pan, S. Liang, *Energy Storage Mater.* **2018**, 13, 168.
- [247] S. Islam, S. Lee, S. Lee, M. Hilmy Alfaruqi, B. Sambandam, V. Mathew, J.-Y. Hwang, J. Kim, *Chem. Eng. J.* **2022**, 446, 137069.
- [248] W. Bi, G. Gao, G. Wu, M. Atif, M. AlSalhi, G. Cao, *Energy Storage Mater.* **2021**, 40, 209.
- [249] D. Fang, X. Xu, R. Bao, R. Wan, F. Yang, J. Yi, T. Zeng, O. Ruzimuradov, *J. Environ. Chem. Eng.* **2021**, 9, 104765.
- [250] T. Zhou, L. Xie, Q. Han, X. Yang, L. Zhu, X. Cao, *Chem. Eng. J.* **2022**, 445, 136789.
- [251] D. Zhou, S. Liu, H. Wang, G. Yan, *J. Power Sources* **2013**, 227, 111.
- [252] H. Kang, Y. Liu, M. Shang, T. Lu, Y. Wang, L. Jiao, *Nanoscale* **2015**, 7, 9261.
- [253] A. Radwan, Y. Liu, Y. Qi, W. Jin, V. Nguyen, X. Yang, S. Yang, W. Chen, *Mater. Res. Bull.* **2018**, 97, 24.
- [254] X. Guo, G. Fang, W. Zhang, J. Zhou, L. Shan, L. Wang, C. Wang, T. Lin, Y. Tang, S. Liang, *Adv. Energy Mater.* **2018**, 8, 1801819.
- [255] M. Clites, B. W. Byles, E. Pomerantseva, *J. Mater. Chem. A* **2016**, 4, 7754.
- [256] W. Zhou, J. Chen, C. He, M. Chen, X. Xu, Q. Tian, J. Xu, C.-P. Wong, *Electrochim. Acta* **2019**, 321, 134689.
- [257] V. S. Reddy Channu, R. Holze, I.-H. Yeo, S. Mho, R. R. Kalluru, *Appl. Phys. A* **2011**, 104, 707.
- [258] P. Ye, X. Wang, M. Wang, Y. Fan, X. Xiang, *Hydrometallurgy* **2012**, 117–118, 108.
- [259] F. Wan, X. Wang, S. Bi, Z. Niu, J. Chen, *Sci. China: Chem.* **2019**, 62, 609.
- [260] M. Xu, J. Han, G. Li, Y. Niu, S. Liu, J. Hou, M. Wang, J. Song, C. M. Li, *Chem. Commun.* **2015**, 51, 15290.
- [261] R. Chen, Z. Wang, Z. Chen, P. Wang, G. Fang, J. Zhou, X. Tan, S. Liang, *J. Alloys Compd.* **2019**, 772, 852.
- [262] P. He, G. Zhang, X. Liao, M. Yan, X. Xu, Q. An, J. Liu, L. Mai, *Adv. Energy Mater.* **2018**, 8, 1702463.
- [263] Y. Zhao, C. Han, J. Yang, J. Su, X. Xu, S. Li, L. Xu, R. Fang, H. Jiang, X. Zou, B. Song, L. Mai, Q. Zhang, *Nano Lett.* **2015**, 15, 2180.
- [264] G. Fang, J. Zhou, Y. Hu, X. Cao, Y. Tang, S. Liang, *J. Power Sources* **2015**, 275, 694.
- [265] R. Baddour-Hadjean, A. Boudaoud, S. Bach, N. Emery, J.-P. Pereira-Ramos, *Inorg. Chem.* **2014**, 53, 1764.
- [266] W. Zhang, C. Tang, B. Lan, L. Chen, W. Tang, C. Zuo, S. Dong, Q. An, P. Luo, *J. Alloys Compd.* **2020**, 819, 152971.
- [267] L. Li, S. Liu, W. Liu, D. Ba, W. Liu, Q. Gui, Y. Chen, Z. Hu, Y. Li, J. Liu, *Nano-Micro Lett.* **2021**, 13, 34.
- [268] P. Wu, T. Xu, Y. Chen, Q. Yang, J. Wang, Y.-N. Liu, Y. Li, *ACS Appl. Energy Mater.* **2022**, 5, 1656.
- [269] B. Tang, G. Fang, J. Zhou, L. Wang, Y. Lei, C. Wang, T. Lin, Y. Tang, S. Liang, *Nano Energy* **2018**, 51, 579.
- [270] K. Yang, Y. Hu, L. Li, L. Cui, L. He, S. Wang, J. Zhao, Y.-F. Song, *Nano Energy* **2020**, 74, 104851.
- [271] F. Wan, S. Huang, H. Cao, Z. Niu, *ACS Nano* **2020**, 14, 6752.
- [272] N. Qiu, Z. Yang, R. Xue, Y. Wang, Y. Zhu, W. Liu, *Nano Lett.* **2021**, 21, 2738.

- [273] C. Liu, Z. Neale, J. Zheng, X. Jia, J. Huang, M. Yan, M. Tian, M. Wang, J. Yang, G. Cao, *Energy Environ. Sci.* **2019**, *12*, 2273.
- [274] M. Tian, C. Liu, J. Zheng, X. Jia, E. P. Jahrman, G. T. Seidler, D. Long, M. Atif, M. Alsalthi, G. Cao, *Energy Storage Mater.* **2020**, *29*, 9.
- [275] B. Sambandam, V. Soundharrajan, S. Kim, M. H. Alfaruqi, J. Jo, S. Kim, V. Mathew, Y. Sun, J. Kim, *J. Mater. Chem. A* **2018**, *6*, 15530.
- [276] F. Ming, H. Liang, Y. Lei, S. Kandambeth, M. Eddaoudi, H. N. Alshareef, *ACS Energy Lett.* **2018**, *3*, 2602.
- [277] H. D. Yoo, J. R. Jokisaari, Y.-S. Yu, B. J. Kwon, L. Hu, S. Kim, S.-D. Han, M. Lopez, S. H. Lapidus, G. M. Nolis, B. J. Ingram, I. Bolotin, S. Ahmed, R. F. Klie, J. T. Vaughey, T. T. Fister, J. Cabana, *ACS Energy Lett.* **2019**, *4*, 1528.
- [278] Y. Xu, X. Deng, Q. Li, G. Zhang, F. Xiong, S. Tan, Q. Wei, J. Lu, J. Li, Q. An, L. Mai, *Chem* **2019**, *5*, 1194.
- [279] Y. Yang, Y. Tang, G. Fang, L. Shan, J. Guo, W. Zhang, C. Wang, L. Wang, J. Zhou, S. Liang, *Energy Environ. Sci.* **2018**, *11*, 3157.
- [280] J. Feng, Z. Xiong, L. Zhao, C. Huang, H. Liu, S. Chen, Z. Wang, Q. Kuang, Y. Dong, Q. Fan, Y. Zhao, *J. Power Sources* **2018**, *396*, 230.
- [281] S. Huang, F. Wan, S. Bi, J. Zhu, Z. Niu, J. Chen, *Angew. Chem., Int. Ed.* **2019**, *58*, 4313.
- [282] Z. Liu, D. Wang, Z. Tang, G. Liang, Q. Yang, H. Li, L. Ma, F. Mo, C. Zhi, *Energy Storage Mater.* **2019**, *23*, 636.
- [283] H. Cao, F. Wan, L. Zhang, X. Dai, S. Huang, L. Liu, Z. Niu, *J. Mater. Chem. A* **2019**, *7*, 11734.
- [284] W. Zhou, J. Chen, M. Chen, A. Wang, A. Huang, X. Xu, J. Xu, C.-P. Wong, *J. Mater. Chem. A* **2020**, *8*, 8397.
- [285] L. Gao, W. Bao, A. V. Kuklin, S. Mei, H. Zhang, H. Ågren, *Adv. Mater.* **2021**, *33*, 2004129.
- [286] H. Chen, H. Ma, C. Li, *ACS Nano* **2021**, *15*, 15502.
- [287] Y. Bai, C. Liu, T. Chen, W. Li, S. Zheng, Y. Pi, Y. Luo, H. Pang, *Angew. Chem., Int. Ed.* **2021**, *60*, 25318.
- [288] C. Liu, Y. Bai, W. Li, F. Yang, G. Zhang, H. Pang, *Angew. Chem., Int. Ed.* **2022**, *61*, e202116282.
- [289] J. Guan, L. Shao, L. Yu, S. Wang, X. Shi, J. Cai, Z. Sun, *Chem. Eng. J.* **2022**, *443*, 136502.
- [290] Z. Feng, Y. Zhang, Y. Zhao, J. Sun, Y. Liu, H. Jiang, M. Cui, T. Hu, C. Meng, *Nanoscale* **2022**, *14*, 8776.
- [291] J. Sun, Y. Zhao, Y. Liu, H. Jiang, C. Huang, M. Cui, T. Hu, C. Meng, Y. Zhang, *Small Struct.* **2022**, *3*, 2100212.
- [292] J. Yao, Y. Li, R. C. Massé, E. Uchaker, G. Cao, *Energy Storage Mater.* **2018**, *11*, 205.
- [293] Y. Du, X. Wang, Y. Zhang, H. Zhang, J. Man, K. Liu, J. Sun, *Chem. Eng. J.* **2022**, *434*, 134642.
- [294] M. Du, F. Zhang, X. Zhang, W. Dong, Y. Sang, J. Wang, H. Liu, S. Wang, *Sci. China: Chem.* **2020**, *63*, 1767.
- [295] Y. Luo, *Comprehensive Handbook of Chemical Bond Energies*, CRC Press, Boca Raton, **2007**, 1688.
- [296] X. Liu, H. Zhang, D. Geiger, J. Han, A. Varzi, U. Kaiser, A. Moretti, S. Passerini, *Chem. Commun.* **2019**, *55*, 2265.
- [297] S. Bao, Q. Bao, C. Li, T. Chen, C. Sun, Z. Dong, Y. Gan, J. Zhang, *Small* **2007**, *3*, 1174.
- [298] Q. Bao, S. Bao, C. M. Li, X. Qi, C. Pan, J. Zang, W. Wang, D. Y. Tang, *Chem. Mater.* **2007**, *19*, 5965.
- [299] H. Liu, J. Wang, H. Sun, Y. Li, J. Yang, C. Wei, F. Kang, *J. Colloid Interface Sci.* **2020**, *560*, 659.
- [300] S. Zhang, W. Li, C. Li, J. Chen, *J. Phys. Chem. B* **2006**, *110*, 24855.
- [301] Y. Liang, L. F. Zhu, P. Liu, H. B. Li, J. Xiao, X. W. Ji, G. W. Yang, *CrytEngComm* **2013**, *15*, 6131.
- [302] B. Lan, Z. Peng, L. Chen, C. Tang, S. Dong, C. Chen, M. Zhou, C. Chen, Q. An, P. Luo, *J. Alloys Compd.* **2019**, *787*, 9.
- [303] Q. Li, Y. Liu, K. Ma, G. Yang, C. Wang, *Small Methods* **2019**, *3*, 1900637.
- [304] F. K. Butt, M. Tahir, C. Cao, F. Idrees, R. Ahmed, W. S. Khan, Z. Ali, N. Mahmood, M. Tanveer, A. Mahmood, I. Aslam, *ACS Appl. Mater. Interfaces* **2014**, *6*, 13635.
- [305] L. M. Z. De Juan-Corpuz, M. T. Nguyen, R. D. Corpuz, T. Yonezawa, N. C. Rosero-Navarro, K. Tadanaga, T. Tokunaga, S. Kheawhom, *ACS Appl. Nano Mater.* **2019**, *2*, 4247.
- [306] Y. Liu, C. Li, J. Xu, M. Ou, C. Fang, S. Sun, Y. Qiu, J. Peng, G. Lu, Q. Li, J. Han, Y. Huang, *Nano Energy* **2020**, *67*, 104211.
- [307] L. Z. Pei, N. Lin, T. Wei, H. D. Liu, H. Y. Yu, *J. Alloys Compd.* **2015**, *631*, 90.
- [308] V. Shrivastava, R. Nagarajan, *Mater. Lett.* **2020**, *280*, 128559.
- [309] Z. Chen, W. Huang, D. Lu, R. Zhao, H. Chen, *Mater. Lett.* **2013**, *107*, 35.
- [310] B. Sambandam, V. Soundharrajan, S. Kim, M. H. Alfaruqi, J. Jo, S. Kim, V. Mathew, Y. Sun, J. Kim, *J. Mater. Chem. A* **2018**, *6*, 3850.
- [311] L. D. Reed, E. Menke, *J. Electrochem. Soc.* **2013**, *160*, A915.
- [312] A. Sarkar, S. Sarkar, T. Sarkar, P. Kumar, M. D. Bharadwaj, S. Mitra, *ACS Appl. Mater. Interfaces* **2015**, *7*, 17044.
- [313] X. Miao, Z. Chen, N. Wang, Y. Nuli, J. Wang, J. Yang, S. Hirano, *Nano Energy* **2017**, *34*, 26.
- [314] J. Wu, Q. Kuang, K. Zhang, J. Feng, C. Huang, J. Li, Q. Fan, Y. Dong, Y. Zhao, *Energy Storage Mater.* **2021**, *41*, 297.
- [315] B. He, Z. Zhou, P. Man, Q. Zhang, C. Li, L. Xie, X. Wang, Q. Li, Y. Yao, *J. Mater. Chem. A* **2019**, *7*, 12979.
- [316] D. Xu, H. Wang, F. Li, Z. Guan, R. Wang, B. He, Y. Gong, X. Hu, *Adv. Mater. Interfaces* **2019**, *6*, 1801506.
- [317] X. Zhu, W. Wang, Z. Cao, S. Gao, M. O. L. Chee, X. Zhang, P. Dong, P. M. Ajayan, M. Ye, J. Shen, *J. Mater. Chem. A* **2021**, *9*, 17994.
- [318] Y. Bai, H. Zhang, B. Xiang, Y. Zhou, L. Dou, G. Dong, *J. Colloid Interface Sci.* **2021**, *597*, 422.
- [319] J. Song, W. Wang, Y. Fang, S. Wang, D. He, R. Zhao, W. Xue, *Appl. Surf. Sci.* **2022**, *578*, 152053.
- [320] W. Yang, W. Yang, Y. Huang, C. Xu, L. Dong, X. Peng, *Chin. Chem. Lett.* **2022**, *33*, 4628.
- [321] Y. Qi, J. Huang, L. Yan, Y. Cao, J. Xu, D. Bin, M. Liao, Y. Xia, *Chem. Eng. J.* **2022**, *442*, 136349.
- [322] D. Ji, H. Zheng, H. Zhang, W. Liu, J. Ding, *Chem. Eng. J.* **2022**, *433*, 133815.
- [323] J. Ding, H. Zheng, X. Ji, *Chem. Commun.* **2022**, *58*, 5241.
- [324] X. Tian, J. Jin, S. Yuan, C. K. Chua, S. B. Tor, K. Zhou, *Adv. Energy Mater.* **2017**, *7*, 1700127.
- [325] P. Chang, H. Mei, S. Zhou, K. G. Dassios, L. Cheng, *J. Mater. Chem. A* **2019**, *7*, 4230.
- [326] H. Ma, X. Tian, T. Wang, K. Tang, Z. Liu, S. Hou, H. Jin, G. Cao, *Small* **2021**, *17*, 2100746.
- [327] H. Wang, K. Huang, C. Huang, S. Liu, Y. Ren, X. Huang, *J. Power Sources* **2011**, *196*, 5645.
- [328] Q. Li, X. Rui, D. Chen, Y. Feng, N. Xiao, L. Gan, Q. Zhang, Y. Yu, S. Huang, *Nano-Micro Lett.* **2020**, *12*, 67.
- [329] H. Jiang, Y. Zhang, Y. Liu, J. Yang, L. Xu, P. Wang, Z. Gao, J. Zheng, C. Meng, Z. Pan, *J. Mater. Chem. A* **2020**, *8*, 15130.
- [330] Y. Jiang, Z. Wu, F. Ye, R. Pang, L. Zhang, Q. Liu, X. Chang, S. Sun, Z. Sun, L. Hu, *Energy Storage Mater.* **2021**, *42*, 286.
- [331] C. Xia, J. Guo, Y. Lei, H. Liang, C. Zhao, H. N. Alshareef, *Adv. Mater.* **2018**, *30*, 1705580.
- [332] B. Tang, J. Zhou, G. Fang, F. Liu, C. Zhu, C. Wang, A. Pan, S. Liang, *J. Mater. Chem. A* **2019**, *7*, 940.
- [333] V. Soundharrajan, B. Sambandam, S. Kim, M. H. Alfaruqi, D. Y. Puro, J. Jo, S. Kim, V. Mathew, Y.-K. Sun, J. Kim, *Nano Lett.* **2018**, *18*, 2402.
- [334] T. Wei, Q. Li, G. Yang, C. Wang, *J. Mater. Chem. A* **2018**, *6*, 20402.
- [335] R. Trócoli, F. La Mantia, *ChemSusChem* **2015**, *8*, 481.
- [336] F. R. Theobald, J.-G. Theobald, J. C. Vedrine, R. Clad, J. Renard, *J. Phys. Chem. Solids* **1984**, *45*, 581.



- [337] X. Liu, Z. Li, H. Fei, M. Wei, *Dalton Trans.* **2015**, 44, 18864.
- [338] G. Xu, H. He, H. Wan, R. Liu, X. Zeng, D. Sun, X. Huang, H. Wang, *J. Appl. Electrochem.* **2016**, 46, 879.
- [339] H. Jiang, Y. Zhang, L. Xu, Z. Gao, J. Zheng, Q. Wang, C. Meng, J. Wang, *Chem. Eng. J.* **2020**, 382, 122844.
- [340] Q. Zong, W. Du, C. Liu, H. Yang, Q. Zhang, Z. Zhou, M. Atif, M. Alsalihi, G. Cao, *Nano-Micro Lett.* **2021**, 13, 116.
- [341] C. Huang, S. Liu, J. Feng, Y. Wang, Q. Fan, Q. Kuang, Y. Dong, Y. Zhao, *J. Power Sources* **2021**, 490, 229528.
- [342] R. Sun, Z. Qin, X. Liu, C. Wang, S. Lu, Y. Zhang, H. Fan, *ACS Sustainable Chem. Eng.* **2021**, 9, 11769.
- [343] Y. Lu, L. Liu, D. Mandler, P. S. Lee, *J. Mater. Chem. C* **2013**, 1, 7380.
- [344] Y. Wei, J. Zhou, J. Zheng, C. Xu, *Electrochim. Acta* **2015**, 166, 277.
- [345] G. Salek, B. Bellanger, I. Mjejri, M. Gaudon, A. Rougier, *Inorg. Chem.* **2016**, 55, 9838.
- [346] C. F. Armer, M. Lübke, M. V. Reddy, J. A. Darr, X. Li, A. Lowe, *J. Power Sources* **2017**, 353, 40.
- [347] D. He, Y. Peng, Y. Ding, X. Xu, Y. Huang, Z. Li, X. Zhang, L. Hu, *J. Power Sources* **2021**, 484, 229284.
- [348] H. Jiang, Y. Zhang, Z. Pan, L. Xu, J. Zheng, Z. Gao, T. Hu, C. Meng, J. Wang, *Mater. Chem. Front.* **2020**, 4, 1434.
- [349] A. G. Macdiarmid, J. C. Chiang, A. F. Richter, A. J. Epstein, *Synth. Met.* **1987**, 18, 285.
- [350] S. Chen, K. Li, K. S. Hui, J. Zhang, *Adv. Funct. Mater.* **2020**, 30, 2003890.
- [351] M. Huang, Y. Mai, L. Zhao, X. Liang, Z. Fang, X. Jie, *Electrochim. Acta* **2021**, 388, 138624.
- [352] W. Bi, J. Huang, M. Wang, E. P. Jahrman, G. T. Seidler, J. Wang, Y. Wu, G. Gao, G. Wu, G. Cao, *J. Mater. Chem. A* **2019**, 7, 17966.
- [353] Y. Chen, C. Li, X. Ma, Q. Qiang, B. Liu, S. Cao, L. Peng, L. Li, T. Lang, *Appl. Surf. Sci.* **2020**, 506, 144816.
- [354] Z. Zhao, Y. Zhou, F. Wang, K. Zhang, S. Yu, K. Cao, *ACS Appl. Mater. Interfaces* **2015**, 7, 730.
- [355] Y. Li, Y. Liu, J. Chen, Q. Zheng, Y. Huo, F. Xie, D. Lin, *Chem. Eng. J.* **2022**, 448, 137681.
- [356] X. Wang, B. Xi, Z. Feng, W. Chen, H. Li, Y. Jia, J. Feng, Y. Qian, S. Xiong, *J. Mater. Chem. A* **2019**, 7, 19130.
- [357] S. Chen, Y. Zhang, H. Geng, Y. Yang, X. Rui, C. C. Li, *J. Power Sources* **2019**, 441, 227192.
- [358] L. V. Kayser, D. J. Lipomi, *Adv. Mater.* **2019**, 31, 1806133.
- [359] M. N. Gueye, A. Carella, J. Faure-Vincent, R. Demadrille, J.-P. Simonato, *Prog. Mater. Sci.* **2020**, 108, 100616.
- [360] J. Kim, S. H. Lee, C. Park, H. Kim, J. Park, K. Y. Chung, H. Ahn, *Adv. Funct. Mater.* **2021**, 31, 2100005.
- [361] M. Wörle, F. Krumeich, F. Bieri, H.-J. Muhr, R. Nesper, *Z. Anorg. Allg. Chem.* **2002**, 628, 2778.
- [362] G. Yang, T. Wei, C. Wang, *ACS Appl. Mater. Interfaces* **2018**, 10, 35079.
- [363] J. Lai, H. Tang, X. Zhu, Y. Wang, *J. Mater. Chem. A* **2019**, 7, 23140.
- [364] H. Jiang, Y. Zhang, Z. Pan, L. Xu, J. Zheng, Z. Gao, T. Hu, C. Meng, *Electrochim. Acta* **2020**, 332, 135506.
- [365] Z. Wang, J. Zhang, H. Wang, X. Wei, J. Zhang, H. Chen, S. Liu, S. Wei, X. Lu, *Electrochim. Acta* **2022**, 404, 139785.
- [366] Y. Song, T.-Y. Liu, B. Yao, T.-Y. Kou, D.-Y. Feng, X.-X. Liu, Y. Li, *Small* **2017**, 13, 1700067.
- [367] J. Cao, D. Zhang, Y. Yue, X. Wang, T. Pakornchote, T. Bovornratnaraks, X. Zhang, Z.-S. Wu, J. Qin, *Nano Energy* **2021**, 84, 105876.
- [368] Y. Bai, H. Zhang, Q. Hu, Y. Zhou, B. Xiang, *Nano Energy* **2021**, 90, 106596.
- [369] Z. Fan, W. He, M. Ni, P. Zhang, W. Tian, W. Zhang, L. Pan, Z. Sun, *Energy Technol.* **2021**, 9, 2000829.
- [370] Q. Zong, Q. Wang, C. Liu, D. Tao, J. Wang, J. Zhang, H. Du, J. Chen, Q. Zhang, G. Cao, *ACS Nano* **2022**, 16, 4588.
- [371] C. Liu, M. Tian, M. Wang, J. Zheng, S. Wang, M. Yan, Z. Wang, Z. Yin, J. Yang, G. Cao, *J. Mater. Chem. A* **2020**, 8, 7713.
- [372] Z. Feng, Y. Zhang, J. Sun, Y. Liu, H. Jiang, M. Cui, T. Hu, C. Meng, *Chem. Eng. J.* **2022**, 433, 133795.
- [373] X. Wang, A. Naveed, T. Zeng, T. Wan, H. Zhang, Y. Zhou, A. Dou, M. Su, Y. Liu, D. Chu, *Chem. Eng. J.* **2022**, 446, 137090.
- [374] K. Zheng, Y. Zeng, S. Liu, C. Zeng, Y. Tong, Z. Zheng, T. Zhu, X. Lu, *Energy Storage Mater.* **2019**, 22, 410.
- [375] M. Du, Z. Miao, H. Li, F. Zhang, Y. Sang, L. Wei, H. Liu, S. Wang, *Nano Energy* **2021**, 89, 106477.
- [376] P. Gao, Q. Ru, H. Yan, S. Cheng, Y. Liu, X. Hou, L. Wei, F. Chi-Chung Ling, *ChemElectroChem* **2020**, 7, 283.
- [377] D. Xie, F. Hu, X. Yu, F. Cui, G. Song, K. Zhu, *Chin. Chem. Lett.* **2020**, 31, 2268.
- [378] F. Hu, D. Xie, D. Zhao, G. Song, K. Zhu, *J. Energy Chem.* **2019**, 38, 185.
- [379] S. Li, M. Chen, G. Fang, L. Shan, X. Cao, J. Huang, S. Liang, J. Zhou, *J. Alloys Compd.* **2019**, 801, 82.
- [380] S. Islam, M. H. Alfaruqi, D. Y. Putro, V. Soundharrajan, B. Sambandam, J. Jo, S. Park, S. Lee, V. Mathew, J. Kim, *J. Mater. Chem. A* **2019**, 7, 20335.
- [381] L. Shan, Y. Wang, S. Liang, B. Tang, Y. Yang, Z. Wang, B. Lu, J. Zhou, *InfoMat* **2021**, 3, 1028.
- [382] W. Tang, B. Lan, C. Tang, Q. An, L. Chen, W. Zhang, C. Zuo, S. Dong, P. Luo, *ACS Sustainable Chem. Eng.* **2020**, 8, 3681.
- [383] K. Zhu, T. Wu, K. Huang, *ACS Nano* **2019**, 13, 14447.
- [384] L. Shan, Y. Yang, W. Zhang, H. Chen, G. Fang, J. Zhou, S. Liang, *Energy Storage Mater.* **2019**, 18, 10.
- [385] L. Ma, N. Li, C. Long, B. Dong, D. Fang, Z. Liu, Y. Zhao, X. Li, J. Fan, S. Chen, S. Zhang, C. Zhi, *Adv. Funct. Mater.* **2019**, 29, 1906142.
- [386] J. Li, K. McColl, X. Lu, S. Sathasivam, H. Dong, L. Kang, Z. Li, S. Zhao, A. G. Kafizas, R. Wang, D. J. L. Brett, P. R. Shearing, F. Corà, G. He, C. J. Carmalt, I. P. Parkin, *Adv. Energy Mater.* **2020**, 10, 2000058.
- [387] Y. Liu, Q. Li, K. Ma, G. Yang, C. Wang, *ACS Nano* **2019**, 13, 12081.
- [388] X. Yu, F. Hu, F. Cui, J. Zhao, C. Guan, K. Zhu, *Dalton Trans.* **2020**, 49, 1048.
- [389] L. Shan, J. Zhou, M. Han, G. Fang, X. Cao, X. Wu, S. Liang, *J. Mater. Chem. A* **2019**, 7, 7355.
- [390] L. Chen, Z. Yang, J. Wu, H. Chen, J. Meng, *Electrochim. Acta* **2020**, 330, 135347.
- [391] D. Bin, W. Huo, Y. Yuan, J. Huang, Y. Liu, Y. Zhang, F. Dong, Y. Wang, Y. Xia, *Chem* **2020**, 6, 968.
- [392] Y. Zhang, H. Jiang, L. Xu, Z. Gao, C. Meng, *ACS Appl. Energy Mater.* **2019**, 2, 7861.
- [393] L. Xu, Y. Zhang, H. Jiang, J. Zheng, X. Dong, T. Hu, C. Meng, *Colloids Surf., A* **2020**, 593, 124621.
- [394] K. Zhu, T. Wu, K. Huang, *Adv. Energy Mater.* **2019**, 9, 1901968.
- [395] Y. Liu, L. Xu, X.-T. Guo, T. Lv, H. Pang, *J. Mater. Chem. A* **2020**, 8, 20781.
- [396] Y. Jing, Z. Zhou, C. R. Cabrera, Z. Chen, *J. Phys. Chem. C* **2013**, 117, 25409.
- [397] M. S. Weimer, R. F. McCarthy, J. D. Emery, M. J. Bedzyk, F. G. Sen, A. Kinaci, M. K. Y. Chan, A. S. Hock, A. B. F. Martinson, *Chem. Mater.* **2017**, 29, 2864.
- [398] C. S. Rout, B.-H. Kim, X. Xu, J. Yang, H. Y. Jeong, D. Odkhuu, N. Park, J. Cho, H. S. Shin, *J. Am. Chem. Soc.* **2013**, 135, 8720.
- [399] J. Feng, X. Sun, C. Wu, L. Peng, C. Lin, S. Hu, J. Yang, Y. Xie, *J. Am. Chem. Soc.* **2011**, 133, 17832.
- [400] J. Feng, L. Peng, C. Wu, X. Sun, S. Hu, C. Lin, J. Dai, J. Yang, Y. Xie, *Adv. Mater.* **2012**, 24, 1969.
- [401] T. Jiao, Q. Yang, S. Wu, Z. Wang, D. Chen, D. Shen, B. Liu, J. Cheng, H. Li, L. Ma, C. Zhi, W. Zhang, *J. Mater. Chem. A* **2019**, 7, 16330.
- [402] S. Britto, M. Leskes, X. Hua, C.-A. Hébert, H. S. Shin, S. Clarke, O. Borkiewicz, K. W. Chapman, R. Seshadri, J. Cho, C. P. Grey, *J. Am. Chem. Soc.* **2015**, 137, 8499.

- [403] Y. Zhou, Y. Li, J. Yang, J. Tian, H. Xu, J. Yang, W. Fan, *ACS Appl. Mater. Interfaces* **2016**, *8*, 18797.
- [404] L. Zhang, Q. Wei, D. Sun, N. Li, H. Ju, J. Feng, J. Zhu, L. Mai, E. J. Cairns, J. Guo, *Nano Energy* **2018**, *51*, 391.
- [405] X. Zhang, S. Wang, J. Tu, G. Zhang, S. Li, D. Tian, S. Jiao, *ChemSusChem* **2018**, *11*, 709.
- [406] Q. Pang, Y. Zhao, Y. Yu, X. Bian, X. Wang, Y. Wei, Y. Gao, G. Chen, *ChemSusChem* **2018**, *11*, 735.
- [407] H. Qin, Z. Yang, L. Chen, X. Chen, L. Wang, *J. Mater. Chem. A* **2018**, *6*, 23757.
- [408] K. Chen, X. Li, J. Zang, Z. Zhang, Y. Wang, Q. Lou, Y. Bai, J. Fu, C. Zhuang, Y. Zhang, L. Zhang, S. Dai, C. Shan, *Nanoscale* **2021**, *13*, 12370.
- [409] T. Zhai, X. Lu, H. Wang, G. Wang, T. Mathis, T. Liu, C. Li, Y. Tong, Y. Li, *Nano Lett.* **2015**, *15*, 3189.
- [410] C. Yang, X. Ou, X. Xiong, F. Zheng, R. Hu, Y. Chen, M. Liu, K. Huang, *Energy Environ. Sci.* **2017**, *10*, 107.
- [411] S. Liu, X. Chen, Q. Zhang, J. Zhou, Z. Cai, A. Pan, *ACS Appl. Mater. Interfaces* **2019**, *11*, 36676.
- [412] L. Chen, Z. Yang, F. Cui, J. Meng, H. Chen, X. Zeng, *Appl. Surf. Sci.* **2020**, *507*, 145137.
- [413] Y. Bai, H. Zhang, B. Xiang, Q. Yao, L. Dou, G. Dong, *Nano Energy* **2021**, *89*, 106386.
- [414] J.-S. Park, S. E. Wang, D. S. Jung, J.-K. Lee, Y. C. Kang, *Chem. Eng. J.* **2022**, *446*, 137266.
- [415] J. Ding, Z. Du, B. Li, L. Wang, S. Wang, Y. Gong, S. Yang, *Adv. Mater.* **2019**, *31*, 1904369.
- [416] X. Xie, G. Fang, W. Xu, J. Li, M. Long, S. Liang, G. Cao, A. Pan, *Small* **2021**, *17*, 2101944.
- [417] Y. Rong, H. Chen, J. Wu, Z. Yang, L. Deng, Z. Fu, *Ind. Eng. Chem. Res.* **2021**, *60*, 8649.
- [418] Q. Su, Y. Rong, H. Chen, J. Wu, Z. Yang, L. Deng, Z. Fu, *Ind. Eng. Chem. Res.* **2021**, *60*, 12155.
- [419] H. Chen, Z. Yang, J. Wu, *Ind. Eng. Chem. Res.* **2022**, *61*, 2955.
- [420] H. Chen, Z. Yang, J. Wu, Y. Rong, L. Deng, *J. Power Sources* **2021**, *507*, 230286.
- [421] Y. Niu, W. Xu, Y. Ma, Y. Gao, X. Li, L. Li, L. Zhi, *Nanoscale* **2022**, *14*, 7607.



**Tingting Lv** is a graduate student under Prof. Pang, at Yangzhou University of chemistry and chemical engineering, China. Her research mainly focuses on the field of electrochemical energy storage materials and their applications.



**Huan Pang** received his Ph.D. degree from Nanjing University in 2011. He is now a distinguished professor at Yangzhou University and a Young Changjiang Scholar of the Ministry of Education in China. He is a senior member of the Chinese Chemical Society. He is the managing editor of *EnergyChem*, the editorial board member of *National Science Review*, *FlatChem*, and *Rare Metals*, and the youth editorial board member of *Nano Research*, *Nano Research Energy*, and *eScience* among other distinguished academic journals. He was recognized as a highly cited researcher in Cross-Field by Clarivate Analytics in 2020 and 2021.